MicroLED-Pumped Colloidal Nanomaterials for Biosensing and Quantum Photonics

Natalie Bruce

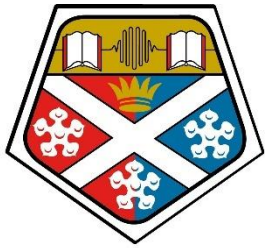

University of Strathclyde Glasgow

Department of Physics, Institute of Photonics

University of Strathclyde

Submitted in fulfilment of the requirements of the

Degree of Doctor of Engineering

2023

Declaration of Authorship

‘This thesis is the result of the author’s original research. It has been composed by the author and has not been previously submitted for examination which has led to the award of a degree.’ 'The copyright of this thesis belongs to the author under the terms of the United Kingdom Copyright Acts as qualified by University of Strathclyde Regulation 3.50. Due acknowledgement must always be made of the use of any material contained in, or derived from, this thesis.’

Signed:

Date:

Abstract

This thesis explores the combination of micro size LEDs (µLEDs) with colloidal quantum dot materials in order (i) to create hybrid bioinstrumentation, with the overarching goal of advancing point-of-care diagnostics; (ii) to progress the development and understanding of elastomeric colour converters; and (iii) to pump-prime and assess the potential for a new single photon source in the visible.

(i) Many existing diagnostic devices rely on specialized expertise and entail prolonged result wait times. µLEDs, traditionally associated with lighting and display applications, are harnessed in this study to miniaturize excitation sources in a fluorescence platform without the need for additional optics. This innovation is showcased through the development of an optical biosensor, illustrating the potential for creating smaller, portable devices while preserving robust detection capabilities. The thesis delves into the detection of proteins conjugated to colloidal quantum dots, demonstrating their detectability using a smartphone. Further exploration of the optical biosensor's capabilities includes multiplexing and the utilization of a novel colloidal quantum dot based fluorescent tag — a supraparticle.

(ii) In addition, colloidal quantum dots incorporated into an elastomeric polymer undergo temperature treatment to investigate their photoluminescent properties. This analysis aims to establish a functional operating temperature for colloidal quantum dot colour converters integrated into devices.

(iii) Lastly, the study investigates colloidal quantum dots (as well as nano-diamonds) combined into a polymer film, exploring their potential as a single photon source. The ultimate objective is to assess whether a µLED can be employed to excite single quantum dots and showcase single photon emission, although this specific outcome was not realized in the present work.

Covid Impact Statement

The original scope of the thesis was a portfolio of projects related to integration of microLED and colloidal quantum dot materials for hybrid instrumentation for several applications including bioinstrumentation and on demand single photon sources. Unfortunately, the progress of these endeavours was significantly hindered by the disruptions caused by the COVID-19 pandemic.

These activities suffered disruption through laboratory and building restrictions which impacted my ability to access the lab due to capacity limits for experimental work and equipment for data collection. Supply chain issues also impacted this work due to availability of raw materials and long delivery times, causing delays in progress even after other restrictions had been lifted.

In an effort to address the challenges encountered, a six-month extension was granted specifically for experimental activities. This extension aimed to provide additional time for advancing the work on single photon sources, which had been particularly adversely affected by the aforementioned factors. It is likely that the outcomes of the single photon work would have been more extensive had it not been for the disruptions caused by the pandemic.

Acknowledgements

Firstly, I would like to thank my supervisors, Dr. Nicolas Laurand, Dr. Mark Scullion and Dr. Loyd McKnight for the advice and guidance given throughout the course of my EngD. A special thanks to Dr. Laurand for the support and patience he has provided throughout the past 5 years and always being forthcoming with encouragement.

Being fortunate enough to work across two institutions, namely the IoP and the FhCAP, has cultivated an outstanding work environment where discussing research is encouraged. Working with these two centres has enabled me to forge numerous friendships throughout my EngD journey, which has helped to keep the process fun even when it has been challenging.

I am grateful to the CDT for Applied Photonics for the opportunity to undertake this EngD and to continue learning and undertake this project. Thank you to Gary and Eilidh who gave so much support and friendship when we were in St. Andrew's together, I wouldn't have been able to do it without you both.

Thank you to the admin staff from the IoP, Lorraine Annand, and Sharon Kelly who helped with many requests I wouldn't have been able to navigate without their expert help. Thank you to Lisa Flannagan from FhCAP for provided much needed support out with her job role.

I would like to thank my family – Mum, Dad, Stephen, Joanne and Peter for all their support when I decided that I needed to change my career, and not thinking I had lost my mind. Kirsty and Anna for always encouraging me and being there with advice, a shoulder to cry on and lots of wine.

Finally, I would like to thank my husband, Fraser. Over the last five years, we've navigated significant milestones together, including a career transition, moving, and renovating our home, planning a wedding, and anticipating the arrival of our first

child—all while I pursued my EngD. Your unwavering support has meant the world to me, and I'm truly grateful.

Table of Contents

List of Figures

List of Tables

List of Publications

- MicroLED biosensor with colloidal quantum dots and smartphone detection Bruce, N., Farrell, F., Xie, E., Scullion, M. G., Haughey, A-M., Gu, E., Dawson, M. D. & Laurand, N., 10 Feb 2023, In: Biomedical Optics Express. 14, 3, p. 1107-1118 12 p.
- Biotinylated Photocleavable Semiconductor Colloidal Quantum Dot Supraparticle Microlaser Eling, C, Bruce, N, Gunasekar, N-K, Edwards, P R, Martin, R W, Laurand, N (Manuscript in Preparation)
- Temperature stability of elastomeric colloidal quantum dot colour converter Bruce, N., Farrell, F. & Laurand, N., 9 Apr 2020, 2019 IEEE 2nd British and Irish Conference on Optics and Photonics, BICOP 2019. Piscataway, NJ.: IEEE, 4 p. 9059578
- Hybrid GaN microLED platform for fluorescence sensing Farrell, F., Bruce, N., He, X., Xie, E., Haughey, A-M., Gu, E., Dawson, M. D. & Laurand, N., 8 Jan 2020. 2 p.

List of Abbreviations

1D	1 - Dimension
2D	2 - Dimension
3D	3 - Dimension
APTES	3-aminopropyltriehoxysilane
BB84	protocol for QKD establish in 1984 by Bennett and Brassard
BSA	bovine serum albumin
CCD	charge coupled device
Cd	cadmium
CLIA	chemiluminescence immunoassay
CMOS	complementary metal-oxide semiconductor
COVID	coronavirus disease
CQD	colloidal quantum dot
CVD	chemical vapour deposition
CW	continuous wave
DI	de-ionised
DPSS	diode pumped solid state
DV	divacancy
ELISA	enzyme linked immunosorbent assay
FEL	long edge pass filter
FFT	fast fourier transform
FhCAP	Fraunhofer Centre for Applied Photonics
FIA	fluorescent immunoassay
FWHM	full width half maximum
HBT	Hanbury-Brown Twiss
HCl	hydrogen chloride
ICT	information communication technology
IMM	Fraunhofer Institute for Microengineering and Microsystems
IR	infrared
ISO	International Standard for Organisation
JPEG	Joint Photographic Experts Group
LD	laser diode
µLED	micro light emitting diode
LED	light emitting diode
MBE	molecular beam epitaxy
MOCVD	Metal-Organic Chemical Vapour Deposition
MQW	multiple quantum wells
NA	numerical aperture
ND	neutral density

NHS	N-hydroxysuccinimidyl
NIR	near infra-red
NIST	National Institute of Standard and Technology
NSB	non-specific binding
NV	nitrogen vacany
ONB	ortho-nitrobenzyl
PBS	phosphate buffer solution
PCB	printed circuit board
PDMS	polydimethylsiloxane
PEG	poly-ethylene glycol
PL	photoluminescence
PLQY	photoluminescence quantum yield
PMMA	poly - methyl methacrylate
POC	point-of-care
PQD	perovskite quantum dot
PVA	poly-vinyl alcohol
PVP	polyvinyl pyrrolidone
QD	quantum dot
QKD	quantum key distribution
RGB	red- green-blue
RI	refractive index
SA-QD	streptavidin conjugated quantum dot
SEM	scanning electron microscopy
Se	Selenide
SMA	Subminiature version A
SP	supraparticle
SPAD	single photon avalanche diode
SPS	single photon source
S	sulphide
TDPA	tetradecylphosphine acid
TE	transverse electric
TEOS	tetraethyl orthosilicate
TIR	total internal reflection
TIRF	total internal reflection fluorescence
TIRFM	Total internal reflection microscopy
TM	transverse magnetic
TOP	triocytlphosphine
TOPO	triocytlphosphine oxide
TP	transfer printing

UV	ultraviolet
UVC	ultraviolet C
VLC	visible light communication
WGM	whispering gallery mode
Zn	Zinc

Chapter 1

1 General Introduction

Compact and portable devices are an important and necessary advancement in the technology industry. As advancements occur this leads to wider adoption of newer technologies by more people. This is critical for improving workflow processes but also businesses. As technology continues to improve there is a trend towards more miniaturised and compact devices. For example, this allows for adoption of this technology into homes, in environmental applications, and primary care settings where space and weight could be a concern.

Photonics technologies are key for the future development of information and communication technologies (ICT) and healthcare and provide a means for novel and innovative advancements; including further development of light sources like light emitting diodes (LEDs) and microLEDs (µLEDs) which can be readily combined with light emitting materials such as quantum dots (QDs).

Gallium-nitride based LEDs in particular have revolutionized solid-state lighting in the last 15 years and the early research in that field led to the Nobel prize in Physics in 2014 [1]. Nowadays, industry is investing heavily in µLEDs (a smaller size version of LEDs, that have a 10^2 to 10^5 times reduction in area, conferring them additional,

advantageous attributes as a new type of display technology. However, the potential range of applications of µLEDs is much wider, including digital lighting, imaging and healthcare among others.

Colloidal quantum dots are colourful light emitting nanoparticles that are being researched for many applications. The 2023 Nobel Prize in Chemistry was awarded for early work on the development and synthesis of these nanomaterials [2]. They can now be found in certain consumer electronics like TV screens or as colour converters in LED lamps, but their potential for novel applications is still mostly untapped.

The overarching aim of this thesis was to explore the development of hybrid devices based on optical pumping of colloidal quantum dots by µLEDs, where that could evolve into compact portable devices suitable for a diverse range of field applications.

Diagnostics devices are an important piece of the technological puzzle for many environments and industries. Healthcare requires ever improving diagnostic tests for early disease detection and progression monitoring. Environmental concerns such as water or soil quality would benefit from rapid on-site testing to enable timely judgements about quality and safety. In this context, the first focus of the research covered work on a proof-of-concept biosensor and making improvements towards a useful diagnostic tool.

Colloidal quantum dots can be incorporated into host (or matrix) polymeric materials for ease of handling and integration with LEDs to act as colour converters for applications such as lighting. Elastomers are interesting matrix materials because they can conform to non-planar surfaces and could also enable mechanically flexible colour converters. The second part of the research shown in this thesis looked at elements that would contribute towards tolerancing limits for better quantum dot elastomeric devices such as operating temperature.

Quantum technology is a rapidly growing research sector within photonics. Efforts to develop scalable techniques to secure, handle and process information have seen

considerable efforts. Exploring the use of µLEDs as a compact pump source for this kind of technology is growing in space applications. The final part of this research explored an idea for an on-demand single photon source in a miniaturised compact package.

1.1 Thesis Synopsis

This EngD doctoral thesis introduces a research portfolio comprising of work towards compact and novel photonic devices and materials for potential applications in health/diagnostic technologies, novel lighting technologies, and in quantum technologies. The portfolio consists of three main projects, forming the results chapters. The thesis is organised as explained below.

Chapter 2 will outline the relevant theoretical concepts, which are common throughout the different topics of this research portfolio. Chapter 3 will focus on experimental work on a compact biosensor utilising a microLED as an excitation source for a colloidal quantum dot fluorescent assay and a smartphone as the detector. In chapter 4 enhancements to expand the biosensor capabilities detailed in chapter 3 are explored. Two methods are investigated: incorporating multiple wavelengths fluorescent tags to demonstrate the possibility of multiplexing and the other is employing a different type of novel tag that could lead to enhanced fluorescence - functionalised quantum dot supraparticles. Chapter 5 will provide a brief overview of research involving the encapsulation of quantum dots within a polymer. This encapsulation aims to extend the operational lifetime of these materials, contributing to prolonging device longevity, and understand their limits. Chapter 6 will delve into work on another project based on an idea for a single photon source. This chapter will investigate the use of encapsulated nanodiamonds and colloidal quantum dots in the context of an on demand single photon source, under a project name QuDos – this was a collaboration between the Institute of Photonics at Strathclyde, the Fraunhofer Centre of Applied Photonics and the Fraunhofer IMM in Germany. Finally, chapter 7 will summarise the research, present the conclusions drawn from it and discuss avenues for potential future works

Chapter 2

2 Background

This chapter succinctly introduces the background of the research presented in this thesis, including basic physical principles, devices and materials that form a common thread across the multiple chapters in this thesis. It includes sections on LEDs and microLEDs (relevant to all results chapters), colloidal quantum dots (relevant to all), also mentioning nano-diamonds (relevant to chapter 6), and basics of planar waveguide (relating to the chapters 3 and 4 on fluorescent sensing). More details and specifics can be found in the relevant results chapters.

2.1 Basic Principles of microLEDs

The design and physics of LEDs is covered in many textbooks for example [3]. Similarly, many reviews on GaN LEDs [4]–[6] and on microLEDs [7]–[11] can be found in the literature. The goal of this section is not to repeat such reviews but simply to give, for completeness, a flavour of the main points related to the LED devices used in this thesis.

2.1.1 LED physics

Light Emitting Diodes (LEDs) are fabricated using direct-bandgap semiconductor materials, that emit light if enough current is applied to cause recombination of charge carriers. Specifically, electrons from the conduction band and holes in the valence band will combine, emitting photons in the process. This process is known as electroluminescence as the charge carriers are electrically injected. LEDs can be made from various semiconductor materials such as silicon carbide (SiC), II-VI semiconductors, zinc oxide (ZnO) [12] and III-V semiconductors such as gallium nitride (GaN) [4], [13] and gallium arsenide (GaAs) [13], among others. Below, we succinctly describe the concepts associated with the design and operation of LEDs.

2.1.1.1 Gallium Nitride LEDs

The LEDs utilised in this thesis are made from GaN materials. GaN LEDs and its alloys with aluminium nitride (AlN) and indium nitride (InN) have the ability to emit a wide range of wavelengths from the UV to blue/green end of the visible spectrum, with progress towards emission in the UVC wavelengths [14]. Although the near UV and blue emitters remain the most efficient in the family [15]. The emitting wavelength of the devices is dependent on the semiconductor composition by alloying with aluminium nitride (AlN) or indium nitride (InN) [16], in turn tuning the band gap energy. GaN is a direct bandgap semiconductor material with a bandgap energy of 3.45 eV which corresponds to 364 nm emission wavelength, (more on bandgap energies in the following section). GaN also has the advantage of being very stable and resistant to degradation under high currents and light illumination [17], making this material an ideal candidate for LEDs. Often GaN LEDs are used in conjunction with phosphors or colour converters for lighting and displays applications to give white light solutions [6], [15], [18]–[20]. Although GaN is a robust material chemically, there have been issues with growth of this structure as there are limited materials that are suitable as substrates that will not cause significant lattice dislocations in the crystalline structure. The most common substrates are sapphire [5], [17] and silicon carbide (SiC) [17]. In this work, the GaN materials were grown on sapphire and for

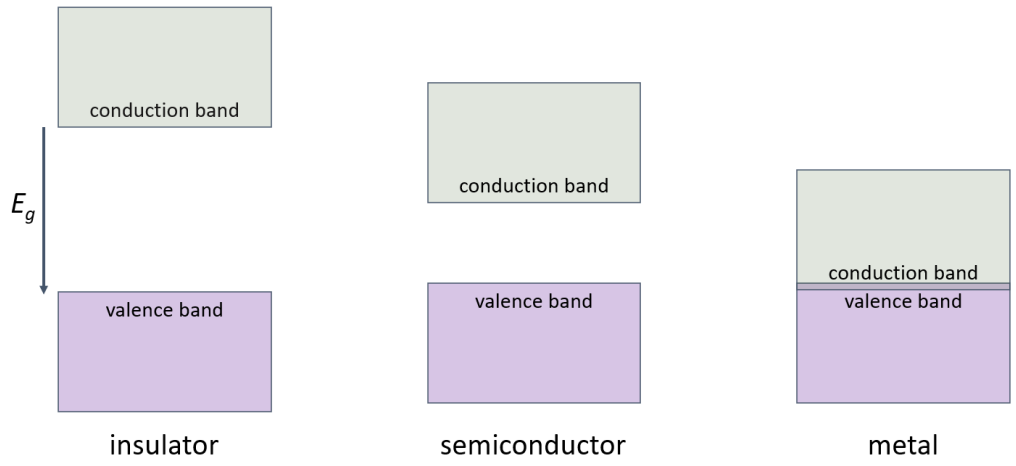

Fig. 2-1 depicts different materials and their bandgap energies. Insulators with the largest band gap, have the lowest conductivity, semiconductors fall in between an insulator and a conductor where they have low conductivity but not zero, and finally metals are good conductors owing to the overlap between the conduction and valence band energies allowing the transfer of electrons and holes between the two bands easily.

the µLED devices mounted in a flip-chip configuration, meaning that the GaN-based µLED emits through the sapphire window. This flip-chip configuration has several advantages over epi-up configuration as it allows for improved current spreading, higher light extraction from the device due to the reduction in refractive index contrast, better thermal management and the ability for further components to be mounted onto the sapphire window [21]. For the work in this thesis, epitaxial LED structures were purchased commercially and the fabrication of the µLEDs done in-house by colleagues of the Institute of Photonics.

2.1.1.2 Bandgaps Energies

The emission wavelength of semiconductors is determined by the material used and the bandgap energy associated with this material. The photons emitted from the electron-hole recombination will have an energy that is equivalent to the bandgap energy of the semiconductor material. The relationship between the bandgap energy and the photon emission wavelength is given by Eq. (1).

$$E_g = E_c - E_v \approx \frac{hc}{\lambda} \tag{1}$$

E_g is the bandgap energy, E_c is the energy of an electron the conduction band, E_v is the energy of the hole in the valence band, h is planck's constant, c is the speed of light, λ is the emission wavelength of the generated photon.

Fig. 2-1 illustrates the variation in band gap energies among different materials and their correlation with the conduction and valence bands. Metals are known for being efficient conductors due to their overlap between the conduction and valence band. This overlap facilitates the recombination of electrons and holes resulting in low or negligible bandgap energies. The opposite is true for an insulator, a substantial band gap energy between the conduction and valence bands, requires a significant amount of energy to excite carriers from one band to the other for recombination. Semiconductors lie between metals and insulators in terms of conduction capabilities. They can conduct reasonably well once sufficient energy is supplied. These conduction properties of semiconductors give these materials the ability to emit light when a current is applied to them. When a sufficient current is applied for an electron to be injected in the conduction band and a hole in the valence band the two have a chance to recombine, the energy being released in the form of a photon when this happens. Again, the photon will have a wavelength that is equivalent to the bandgap energy of the semiconductor material (see Eq. (1)). Using different semiconductor materials with different bandgap energies enables the coverage of different emission wavelengths ranging from the UV to IR.

For efficient electrical injection of carriers in the semiconductor for light emission, a diode is typically formed. This necessitates the use of doped semiconductors, combined in certain cases with a region of intrinsic semiconductor.

2.1.1.3 Types of semiconductors

Intrinsic semiconductors are materials which have not been subject to doping. Doping is a process where atoms or impurities are added to a material to enhance its properties such as increasing conduction properties by donating or capturing electrons. There are two different ways to dope a semiconductor. Creating more electrons in the conduction band by incorporating electron-donating dopants is

known as an n-type semiconductor, whereas increasing the number of holes in the valence band (with the dopants capturing valence electrons, which is the same as donating holes) is known as a p-type semiconductor. A doped semiconductor will have higher conduction compared to an intrinsic semiconductor as there are more free carriers available.

2.1.1.4 p-n Junctions

LEDs are fabricated using doped semiconductor material, where a p-type and n-type semiconductor come into contact to form a p-n junction. Without any external voltage or bias applied between the n and p regions, some excess carriers diffuse to the other doped regions - electrons from n to p and holes from p to n. Doing so they recombine with the opposite type of free carriers. This creates a space charge (or depleted) region between the p and n regions which has an electric field that opposes further diffusion of holes and electrons. When a forward bias is applied across the junction, excess carriers between the materials can overcome the electrical barrier of the charge region and current flows. These electron and holes can then recombine, leading to the generation of light. This recombination process occurs as carriers diffuse between the p and n type semiconductor regions. The rate at which these excess carriers recombine is dependent on the density of electrons in the active region of the p-n junction. The carriers will diffuse over a certain length (diffusion length) before recombining. A p-n junction is known as a homojunction if the p and n-doped material are of the same composition. p-n homojunctions have relatively low recombination rates due to a larger diffusion length, making them less efficient. On the contrary if a reverse bias is applied, no current can flow – hence such a structure is a diode; the current can only flow in one direction.

Most efficient LED technologies will be based on double heterojunctions structures. A comparison of homojunction and double heterojunction structures are shown in Fig. 2-2. The efficiency is improved by surrounding smaller band gap material with larger bandgap material to create potential barriers, this is often done by using an undoped (intrinsic) semiconductor material of a slightly different composition

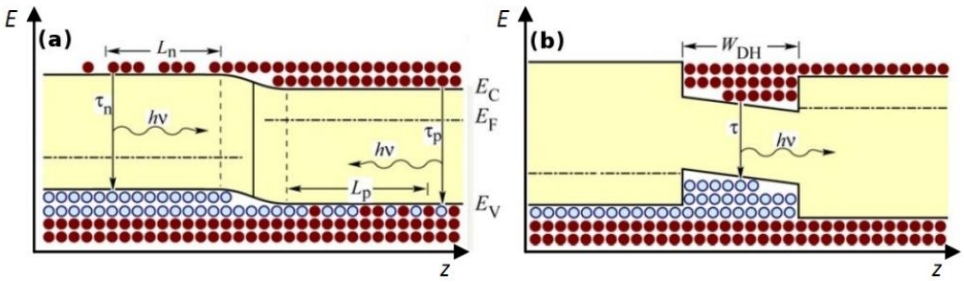

Fig. 2-2 Diagram of a p-n junction b) p-i-n junction under forward bias.[3] **Where, L_n – diffusion length of n-type material, L_p – diffusion length of p-type material, τ_p – carrier lifetime, τ_n – n-type carrier lifetime, $h\nu$ – photons emitted with bandgap energy, E_c – conduction band energy, E_v, - valence band energy, E_F – Fermi energy, W_{DH} – width double heterostructure. This figure is reproduced with permission of the licensor through PLSclear.**

between the doped p and n-type materials, also known as a p-i-n diode. The barriers confine the electrons in the smaller band gap material known as the active region, increasing the density of electrons and holes in this smaller region, and reducing the diffusion length for carriers to recombine, resulting in increased efficiency. Further improvements can be made when the intrinsic material is sufficiently thin enough, i.e. less than the de Broglie wavelength so that a quantum well is created, increasing the carrier recombination further. Quantum well or multi-quantum wells are typically the active region in LEDs; they are present within the intrinsic region of the p-i-n junction.

The main advantages of LEDs are long device longevity, reduced dimensions, better thermal management than conventional lighting, high response time (switching on/off) [22], are mechanically robust and have low energy consumption.

2.1.1.5 LED fabrication

Commercial III-nitride LED wafers are often grown by metal organic chemical vapour deposition (MOCVD). The crystalline structure is grown on a substrate by depositing the desired material from a mixture of vapours. The crystal growth is led by a chemical reaction rather than physical deposition of the elements. The most common substrate for GaN materials is sapphire, and this is what the microLEDs in this thesis are grown on. The atoms are added to form the crystal structure layer by layer and the composition of the vapour in the MOCVD chamber will determine the properties

of the structure. Following the growth of the crystal structure for the LEDs, the wafers require etching to form the individual LEDs chips. Due to the robustness of the III-nitride crystal structure, dry etching such as ion etching is used since the material is more resistant to wet etching techniques [23]. The development of multiple quantum wells (MQW) in GaN materials is what allowed the creation of bright and efficient blue LEDs [7].

2.1.2 microLED

Typically, LEDs employed in lighting applications have an emitting area around 1 mm by 1 mm in dimensions [24]. If the size of the emitting region of LED chips is reduced, it results in mini-LEDs and micro-LEDs. Specifically, LED structures measuring less than 100 µm feature size are referred to as micro-LEDs (µLEDs). Historically, LEDs ranging from 100 µm to 300 µm were designated as µLEDs. As the technology for LEDs evolved the terminology for the devices in this size range are now recognized as mini-LEDs (mLEDs) [11].

The µLED used in this thesis is fabricated using commercially grown GaN on sapphire wafers that have a thickness of 300 µm. A layer of undoped (intrinsic) GaN is deposited between the sapphire and the p-type and n-type GaN, this helps to reduce the lattice mismatch between the doped GaN active material and the sapphire substrate. Reducing the lattice mismatch is important during the fabrication of these materials as it reduces the number of dislocations in the crystal lattice. The active GaN material consists of multiple quantum wells (MQWs) which are then topped with p-GaN to complete the wafer. Once the wafers are completed, they are subjected to

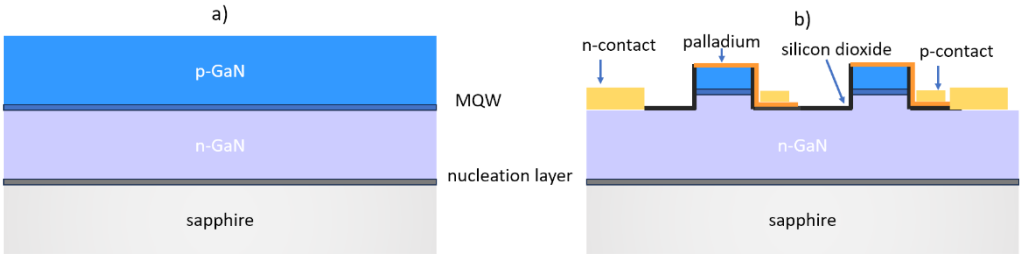

Fig. 2-3 a) schematic of the layers of a GaN wafer used for LED fabrication b) GaN wafer following photolithography to create MQWs and the individual LED chips.

photolithography and etching to make the individual LED chips. The LED emitters are defined by photolithography and then plasma etched down to the n-GaN layer. Next, silicon dioxide is deposited to provide electrical insulation between each pixel, followed by palladium being spread over the top of the p – GaN to act as electrical contacts and a mirror to help improve the light extraction efficiency. Finally, a mixture of titanium/gold is deposited as a metal bonding pad for each of the contact pads so the LED can be electrically driven A schematic of the layers of a GaN wafer and how the photolithography process changes the structure of the layers is shown in Fig. 2-3 a) and b).

By reducing the size of the light emitting material in LEDs this has helped to improve the performance characteristics of these devices, such as higher optical power density, fast response, high contrast, lower power consumption and longer device lifetime [10].Some examples of µLEDs that have been produced by the Institute of Photonics (IoP) are shown in Fig. 2-4. This has helped to broaden the applications that µLEDs can be used for such as visible light communications (VLC) [10], [27], [28] ,

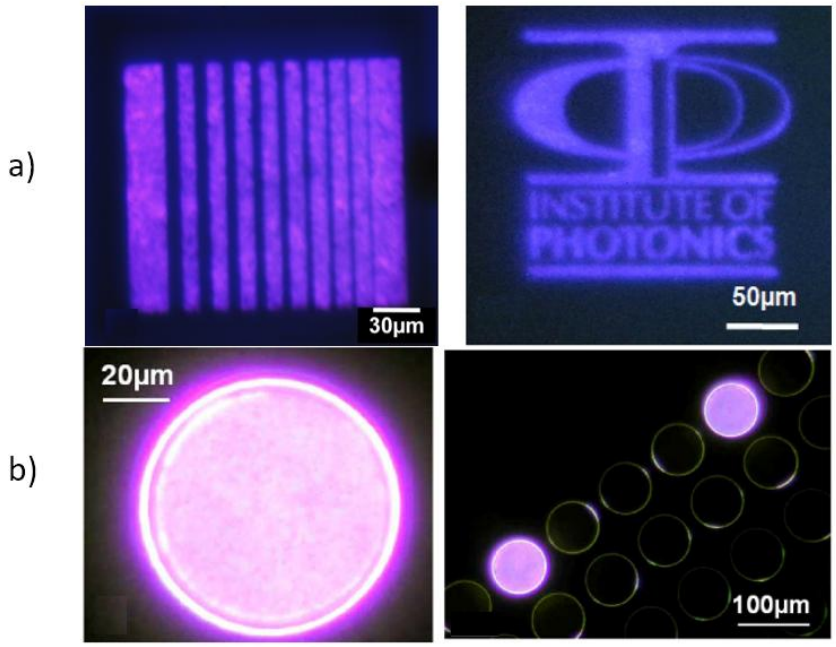

Fig. 2-4 Microscope images of µLEDs fabricated in the IoP a) a 1D array of violet bars (left), the IoP logo displayed using µLEDs(right)[25] b)Microscope images of UV pixels taken through a sapphire substrate, right image is an individual UV pixel and the left image is a pair of pixels operating. [26].

wearable displays [9], phototherapy [28], biomedical imaging and sensing systems [6] and optogenetics [8].

Due to the small pixel size and high optical power density, this made µLEDs an ideal excitation source for a compact biosensor which is presented in chapter 3.

2.2 Semiconductor Quantum Dots

Electronic and optical properties of bulk semiconductors materials are governed by their elemental composition and crystal structure. Improvements in crystal growth via molecular beam epitaxy (MBE) and metal organic chemical vapour deposition (MOCVD) enabled highly crystalline materials to be fabricated. Advancements in crystal growth have allowed the customisation of semiconductor materials allowing fabrication of different materials with more desirable optical properties. With these customisable crystalline materials, spatial dimensions can be tuned to a degree that quantum confinement is observed, inherently changing the electronic and optical properties of the material.

Bottom-up synthesis via wet chemistry is also allowing the creation of semiconductor nanocrystals, which can be processed from solution (see section 2.2.2).

2.2.1 Quantum Confinement

Quantum confinement in a material occurs when electrons and/or holes are constrained in one or more dimensions to an extent that becomes comparable to the materials' de Broglie wavelength. This happens when a particle of semiconductor material is so small its size approaches the Bohr radius, causing the electron and hole wavefunctions to "sense" the material edge and overlap. There are several types of quantum confined structures, and these can be classified related to their degree of confinement. In Fig. 2-5 a schematic is presented illustrating the different degrees of confinement on semiconductor materials and the resulting effect of confinement on the semiconductor electronic structure. A bulk material that lacks electron confinement is referred to as a 3D material. When there is one degree of confinement in any direction it is classed a 2D quantum well structure. With two degrees of

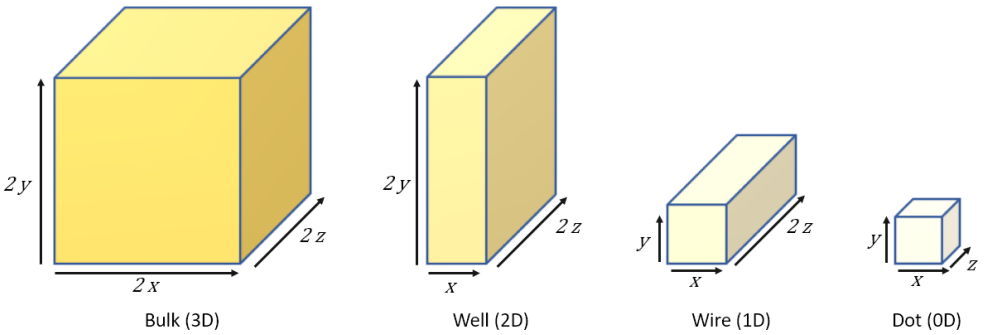

Fig. 2-5 illustrates the various degrees of quantum confinement observed in semiconductor materials. The diagram depicts different structures: bulk material, quantum well, quantum wire, and quantum dot, each representing different degrees of confinement. The bulk material demonstrates dimensions with no confinement in any direction. The quantum well exhibits confinement in one direction, while the quantum wire showcases confinement in two directions. The quantum dot confinement in all three dimensions

constraint, the material is considered 1D and referred to as a quantum wire. Materials with zero degrees of freedom are known as quantum dots, where the electrons are constrained in all 3 directions. As the electrons are subject to confinement in all 3 directions in a QD, they exhibit discrete atom like density of states [29], giving rise to higher energies in this type of material compared to the bulk, and different optical properties.

The overall bandgap energy of the quantum dots depends on the effective mass of the electrons and holes within the material, as well as the bandgap of its bulk counterpart [30]. The bandgap energy of a spherical quantum dot ($E_{g(QD)}$), ignoring the hole-electron interaction, is given by the equation:

$$E_{g(QD)} = E_{g(bulk)} + \frac{\pi^2 \hbar^2}{2m_{e-h}R^2} \quad (2)$$

Where $E_{g(bulk)}$, is the band gap energy of the bulk crystal, m_{e-h} is the effective mass of the electron and holes and R is the quantum dot radius.

Therefore, as the size of the QD is changed the resulting effect is the effective bandgap of the material changes. Due to the change in the bandgap energy of the material, the wavelength of emitted photons from the QDs upon excitation will be different depending on the size of the material bandgap. As the size of the QD

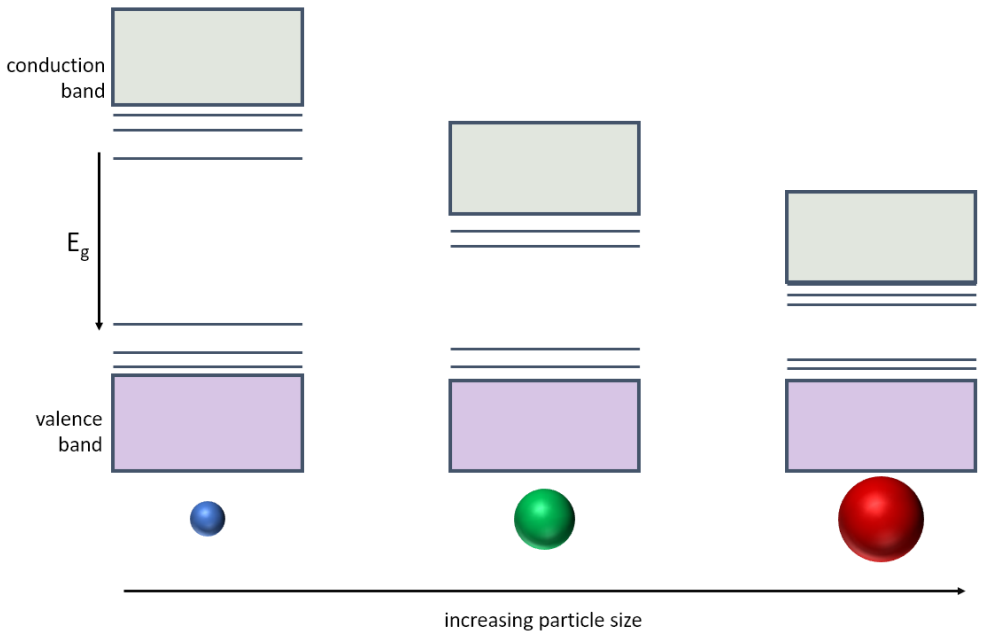

Fig. 2-6 representation of the bandgap structures and their relation to size dependence of the quantum dots. As the size of the quantum dot increases, the corresponding bandgap energy decreases. As the size of the quantum dot decreases the degree of confinement is larger and the energy required for an electron to move from the valence band to the conduction band increases.[29]

reduces, the band gap energy will increase, causing a shift in optical properties towards blue emission as shown in Fig. 2-6.

An electron which is excited from the valence band to the conduction band continues to interact strongly with the hole left in the valence band due to Coulomb attraction; this strongly confined electron-hole pair that is generated is called an exciton. Together with the size tuning and quantum confinement, QDs can be tailored for many different applications where emission wavelength and absorption are important characteristics.

2.2.2 Colloidal Quantum Dots (CQDs)

CQDs are nanoparticles that are suspended in a solvent to form a colloidal solution. Their emission wavelength is related to the nanocrystal diameter and are typically below 20 nm [31]. CQDs like other quantum confined semiconductor materials emit light with their emission wavelengths being dependent on their size and bandgap energy of the material, details of which have been outlined in section 2.1.1.2. As CQDs

are in solution this lends them to being readily incorporated into different formats and structures such as encapsulation in polymers or enables their self-assembly into supraparticles. This processability allows for integration into devices such as laser, LEDs, solar cells and photo detectors [31]. While encapsulated the CQDs can act as colour converters for use with µLEDs when used in higher concentrations. At lower concentrations, incorporation into polymer matrices could allow for CQDs to act as a single photon source, as isolated, they will behave as artificial atoms.

2.2.2.1 Optical Properties of CQDs

CQDs have special luminescence and absorption properties related to their size and quantum confinement. They exhibit high photoluminescent quantum yield (PLQY), narrow emission, broad absorption and their peak emission wavelength is size dependent.

The optical properties of CQDs can be understood in the context of a simplified model known as a two-level system, which is commonly used to describe the behaviour of quantum systems.

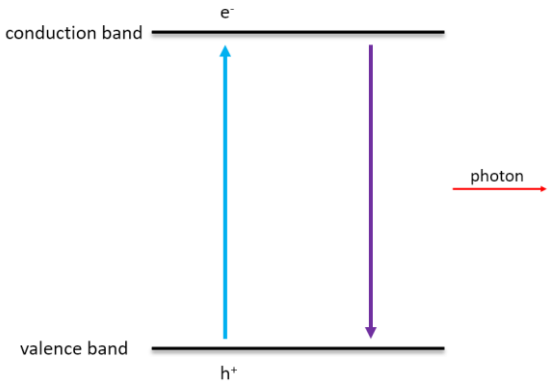

Fig. 2-7 representation of a two-level energy system in a CQD. E- represents the electron in the conduction band, h+ represents the hole in the valence band

A schematic of a two-level system is shown in Fig. 2-7. There are two energy levels: the conduction band which is the excited state for carriers and the valence band which is the ground state for carriers. Since CQDs operate as a two-level system, when they absorb light, an electron is excited from the valence band to the conduction band leaving a hole behind. This electron-hole pair create an exciton. As

the excitons recombine – return to ground state, the exciton energy is released in the form of photon. The absorption and emission of CQDs will correspond to the energy transitions between the discrete quantum mechanically allowed levels. This basic concept helps to explain some of the optical properties of colloidal quantum dots.

The emission wavelengths of the CQDs can be tailored with the size of the particles as well as the material composition of the QD. Larger CQDs will have longer emission wavelengths, as well as a longer fluorescence lifetime due to the more closely space discrete energy levels.

CQDs are an attractive material for a single photon source (as described in Chapter 6), due to their ability to operate at room temperature with excellent optical properties broad absorption, narrow emission wavelengths and photostability at room temperature [32]. The sizes of the CQDs can be controlled during the synthesis process and their emission wavelength can be tailored towards the emission required for the desired application. Although PL blinking of a single CQD can occur, this has been greatly reduced for the more well developed materials such as CdSe/CdS core shell materials [32]. Another factor that could make CQDs a desirable single photon source is due to the solution processability, the ability to manipulate the location of CQDs and isolate them with ease and accuracy. Young-Shin et al, have shown that it is possible to achieve a single photon emission purity of 0.061 [33], with lead halide perovskite quantum dots compared with a nanodiamond single photon source giving a purity of 0.10 [34] which is often used as standard photon source. This level of purity at room temperate gives promising results for further development of different and miniaturised experimental systems for single photon emission.

2.2.2.2 Core/shell structure of QDs

CQDs often consist of a central core of semiconductor material that is encapsulated by a thin shell of a different semiconductor material. The shell helps passivate the dangling bonds at the surface of the CQD materials that can otherwise result in trap states which in turn can reduce the quantum efficiency such materials. A schematic

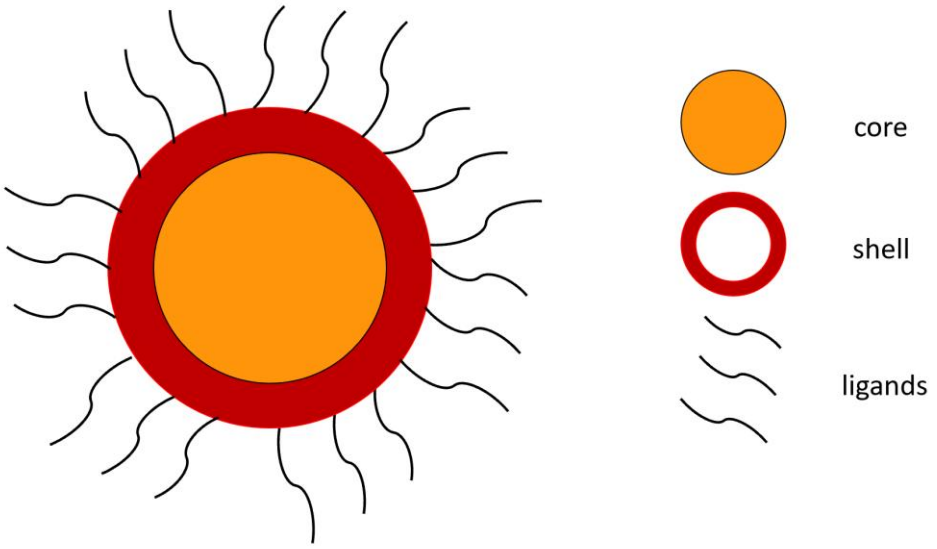

Fig. 2-8 illustration of a quantum dot showing core/shell structure. The orange core is encased in a red outer shell material. It is the outer shell material where ligands can be attached to the core/shell surface. This would also be the site where surface functionalisation could be carried out.

of this core/shell structure is shown in Fig. 2-8. The choice of the shell is important both for limiting the defects and for the confinement of the carrier.

Ideally, the lattice of the shell material needs to be close to the lattice of the core material. ZnS is often used as a shell material for II-VI and III-V core material. The lattice mismatch with CdSe is around 12% [35]; because of the strain caused by this mismatch this limits the thickness of the shell that can be grown defect free to a few monolayers.

In this work, CQDs based on CdSe or CdSSe core and ZnS as a shell are used. These types of CQDs are called type-I because the bandgap of the shell material is higher than that of the core material. Therefore, the electrons and holes are (mostly) confined in the core, which increases their overlap and enhances their recombination.

Another way that the optoelectronic properties of the CQDs are enhanced is through the use of different ligands which are used help to disperse the CQDs in solvents.

2.2.2.3 Important Role of Ligands

Ligands play a crucial role in the synthesis and application of CQDs, serving various functions and offering advantages. They act as a protective capping layer for the CQD particles, effectively saturating any dangling bonds on the particle surface and forming a protective barrier against the environment. Furthermore, ligands exert control over the nucleation and growth kinetics during the synthesis process [36]. Post-synthesis, the choice of ligands assists in dispersing the CQDs in a solvent, while maintaining control over the stability and aggregation of the nanoparticles. Ligands also significantly impact the photo physics of quantum dots by passivating surface traps, ultimately enhancing the quantum efficiency of CQDs. Typically synthesized in non-polar organic solvents, CQDs are equipped with hydrophobic ligands like triocytlphosphine oxide (TOPO), trioctylphosphine (TOP), tetradecylphosphine acid (TDPA), oleic acid, or amines [37]. However, this hydrophobic nature makes CQDs unsuitable for numerous applications, such as in biological research, necessitating ligand exchange or further encapsulation with polymers to impart water solubility. Although ligand exchange may be required for some biological applications, for many applications, they will play the role of stabilising the nanoparticles in different materials and allow applications such as spin-coating and ink jet printing [38].

2.2.2.4 Different QD materials

Over the years many different types of semiconductor material have been explored for use as CQD nanoparticles. Various compounds ranging from II–VI and I–III–VI compounds, as well as transition-metal dichalcogenides, perovskites, and carbon [39] have been explored. Due to this wide variety of materials CQDs can be synthetised from, they have extensive emission wavelengths covering the UV to NIR range. As II-VI semiconductor CQDs are some of the most well researched nanocrystal structures and the material used in this thesis the next section will outline more details about them.

2.2.2.5 II-VI Semiconductor Quantum Dots

II-VI materials consist of elements from group 2 – alkaline earth metals and group 16 – reactive nonmetals. II-VI QDs can have a broad range of band gaps and lattice

constants depending on their crystal structure arrangement. Common II-VI compounds used include cadmium selenide (CdSe), cadmium sulphide (CdS) and zinc sulphide (ZnS) as well as their alloys. All the QD materials used in this thesis are cadmium based. In some instances, there are different types of surface functionalization using different types of ligands or polymers so that the QDs are suitable for different applications.

2.2.3 Bottom-up Quantum Dot synthesis

There are several methods used to synthesize QDs. Bottom-up techniques such as MBE and MOCVD are commonly used and are driven by assembling atomic building blocks from nucleation and by Stranski-Krastanov growth [29] to create nanoscale structures. Epitaxial growth relies on compressive strain force through deposition on a specific surface or substrate [40] . These types of fabrication are expensive and require a substrate for the materials to be grown on, adding an additional element of challenge as issues such as lattice mismatch between substrate and material being grown which can cause unwanted strain and lattice dislocations resulting in poorer quality materials and reproducibility. As the QDs used throughout this thesis are colloidal quantum dots (CQDs) we will outline their fabrication in more detail. CQDs are fabricated by chemical solution processing using bottom-up approaches.

2.2.3.1 Hot-Injection Organometallic

Hot-injection QD synthesis involves heating specific organic solvents followed by injecting semiconductor precursors into the solution [41]. To make cadmium selenide (CdSe) quantum dots via this method, cadmium (Cd) and selenide (Se) precursors are mixed with dimethylcadmium ($Cd(CH_3)_2$) and elemental Se in liquid tri-n-octylphosphine (TOP). This precursor mixture is then rapidly injected into a heated tri-octylphosphine oxide (TOPO) solution. Typically, TOPO is in a batch reactor, where the atmosphere is inert to aid the reaction. An image illustrating the typical experimental set-up for hot-injection can be seen in Fig. 2-9. The TOPO, which serves as a stabilizing agent, allows the mixture to reach a high reaction temperature of

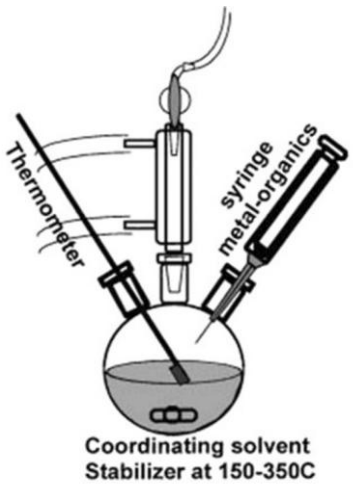

Fig. 2-9 schematic of hot injection method from [38]**. There is a syringe demonstrating how the precursor mixture can be injected into the heated solvent and TOPO mixture. Reproduced under CC BY 4.0 licence.**

approximately 320 ˚C [42]. The QD crystals will develop over several hours, and as the reaction continues different size distributions of QDs will form. Hot-injection allows for the rapid growth and nucleation of monodispersed QDs through the instantaneous saturation of the reactants. Cadmium oxide (CdO) is often used as an alternative to $Cd(CH_3)_2$ as this material is highly toxic, explosive and expensive, which means that while using this compound this form of synthesis is not ideal for large scale production and better used for smaller batch synthesis.

2.2.3.2 Non-injection Organometallic

One key disadvantage of hot-injection synthesis is the poorer reproducibility of the results at larger scales due to challenges in controlling the reaction temperatures upon injection. This has led to alternative methods for synthesis encompassing a single pot, low temperature process referred to as non-injection. Non-injection is an alternative synthesis of CQDs while allows for a larger scale production[42] whilst still producing CQDs of similar size. A metal salt is mixed into a strong solvent, where particles can form at temperatures of around 70 ˚C. Adjusting this temperature will vary the size distribution of the QDs.

2.2.4 Aqueous Quantum Dots

When considering QDs for different applications it is sometimes necessary to modify the solvent CQDs are carried in. For example, biological applications often require CQDs to be in an aqueous solution to increase their biocompatibility. To produce CQDs in an aqueous medium, organometallic solvent synthesis methods are often employed first, followed by a subsequent phase transfer to make the CQDs compatible with water dispersion. While this method is still commonly used, it is often more advantageous to directly synthesize the CQDs in an aqueous solvent from the beginning. This is because the organic solvent remaining after the phase transfer process is highly toxic and cannot be reused, causing environmental concerns. There are other advantages to direct synthesis in water such as surface functionalisation, lower toxicity and lower reaction temperatures [42].

2.2.4.1 Synthetic in Continuous Reactors

In this synthesis method reactants are continuously introduced into a reactor and subsequently emerge as a continuous stream of CQD solution. This is beneficial over batch synthesis as the reaction parameters are more readily controlled such as residence time, temperature, and pressure with the ability to give more consistent quality of production. An image from our collaborator Fraunhofer IMM is shown in Fig. 2-10 a). Microfluidics are often used within these kinds of reactors to control the solution flow. An image of quantum dots made using this synthesis method are shown in Fig. 2-10 b), more details of this synthesis are given in chapter 6.

Fig. 2-10 a) Image of continuous synthesis reactor as seen in [43] **from project collaborator, Fraunhofer IMM., reproduced under CC BY 4.0. b) quantum dots made using continuous synthesis from Fraunhofer IMM collaborator excited under ultraviolet light**

2.3 NV centre Nanodiamonds

In this thesis, nanodiamonds are utilised as an alternative material for investigating single photon emission (Chapter 6). Nanodiamonds, which are nanoparticles derived from diamond, share similar properties to those found in bulk diamond. Depending on the method of synthesis the size of diamond nanoparticles can range from a few nanometres to 200 nm [44]. These properties include high hardness, excellent thermal conductivity, electrical resistivity, chemical stability, biocompatibility, and resilience to harsh environments[45], [46]. This variety of properties means that nanodiamonds are used across various fields. Fluorescent nanodiamonds have been used in biological sensing as an alternative to QDs as they are more biocompatible and less toxic [47] for bioimaging and microscopy [48] as well as drug delivery in cancer treatments [48]. Other applications of nanodiamonds include for use as a

single photon source [34] for quantum key distribution and quantum computing. Nanodiamond is used in this thesis for the purpose of demonstrating single photon emission with the micro – PL system which was established in chapter 6.

2.3.1 Optical Properties of Nanodiamonds

The fluorescence in nanodiamonds arises from point defects that are created in the diamond lattice structure. These defects are known as colour centres. One of the most used colour centres in diamond is the nitrogen vacancy (NV). NV centres occur when a nitrogen atom is substituted for a carbon atom, known as a substitutional defect, and is adjacent to a vacancy defect in the carbon structure of diamond [45], [49], [50]. A representation of the crystal structure of nanodiamond containing NV centres is shown in Fig. 2-11. There are two charge states that can occur in NV centres, neutral vacancy (NV^0) and a negatively charged state (NV^-). NV^- are more commonly used in quantum technologies as they show bright and stable photoluminescence under visible wavelength excitation. The NV^- emission occurs at 637 nm due to a zero phonon line, whereas NV^0 zero phonon line will emit at 575 nm [50]. This is the distinguishing feature between the two vacancy centres. It is important to note that the optical transitions from NV centres do not occur from the

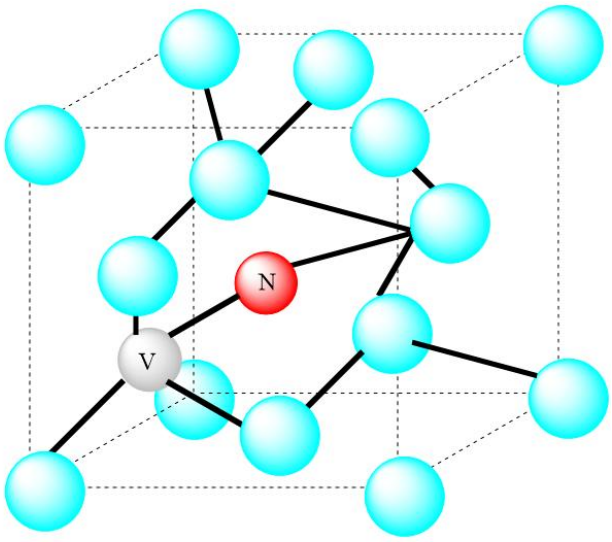

Fig. 2-11 Representation of chemical structure of nitrogen-vacancy centre nanodiamond. The blue spheres represent carbon atoms, the red sphere represents the nitrogen atom, and the grey sphere represents the vacancy in the crystal lattice

conduction/valence band relationship but from the discrete defect levels from within the diamond band gap, as indicated from the sharp zero phonon line and well-defined vibronic bands of the NV^0 and NV^-.

2.3.2 Synthesis of NV centre nanodiamonds

Nanodiamonds can be fabricated through detonation or milling of synthetic bulk diamond which has been made through chemical vapour deposition (CVD) or high pressure, high temperature [45]. Although these techniques to create nanodiamonds are used routinely, they have many disadvantages such as poor control of the size of the nanodiamonds, and contaminants are often present after this process leading to further post-processing requirements. The NV centres are introduced to the carbon lattice through means of ion implantation or deposition during the CVD process [49].

2.3.3 NV – Nanodiamond as a single photon source

When considering a material as a single photon source we should define how this differs from a classic source where photons are emitted randomly following Poissonian distributions. An ideal single photon source would be expected to produce one photon at a time; however, in practice there is a probability that real photon sources may emit zero or multiple photons simultaneously. To assess whether a photon source truly emits a single photon, photon statistics must be relied upon. There are a few parameters that are used to define a single photon source, one of the most important ways to characterise a photon source being, the second order auto-correlation function ($g^2(0)$). This intensity correlation can be measured using a Hanbury-Brown and Twiss (HBT) experimental set up (described in Chapter 6) to determine the probability of detecting two photons separated by a certain time difference.

Single photon sources are normally atom-like systems where electronic transitions occur at discrete energy levels. These energy transitions can be induced by electrical or optical excitation. Although single atoms can be used as single photon sources, since they operate as a two-level system they require trapping in high-finesse optical cavities, so that the atoms can be placed in the lowest quantum state and can be

exploited for testing quantum mechanics and quantum information purposes [51]. Other sources of single photon sources can include single molecules and single QDs, however these also require optical cavities for ideal operation, which is not suitable for all applications. QDs are one of the most well researched materials for use as a single photon source although most of this research concentrates on epitaxially grown QDs. To obtain single photon emission from QDs substantial equipment required. An alternative to epitaxially grown QDs that is being investigated is diamond containing colour centres. NV centre nanodiamond has many desirable properties namely it is resistant to decoherence, which would lower the quantum efficiency of materials. Sources of decoherence include nuclear spins, low electron concentration and phonon scattering.

2.4 Optical Waveguide Principles

The work on an evanescent wave fluorescent biosensor presented in chapter 3 and 4 involves the use of a glass plate as a planar waveguide. Therefore, the principle of planar optical waveguides based on total internal reflection is outlined in this section.

Optical waveguides are structures which are used to confine and guide light waves. Ideally, these waves can propagate within the waveguide medium without significant loss or dispersion. They are an essential component of photonics since they can be used for multiple functions such as guiding, coupling, switching, splitting, and multiplexing of light. They are often used in integrated optics for semiconductor lasers and optical integrated circuits Waveguides can be passive or active in their operation, and their shape and material dictate the properties and types of waves that can be guided within the medium.

According to this definition, the glass microscope slide used in chapters 3 and 4 of this thesis is referred to as a planar waveguide; because it is highly multimode, it may be also appropriately described as a light guide. It functions by confining light emitted from a µED, guiding it to a region where immunoassays or fluorescent tags are present on the glass surface. The evanescent waves of the guided light, which extends from the glass are used to excite the fluorescent tags. The theory presented here

predominantly applies to planar (or slab) waveguides. However, it is worth noting that various other types of waveguides exist, such as channel, rib, and cylindrical (nonplanar waveguides), each of which is more suitable for specific applications.

Slab waveguides are simple structures where the core material (n_c) is surrounded by two materials of lower refractive index, known as cladding (n_f) and substrate (n_s), a schematic of the basic structure of a slab waveguide is shown in Fig. 2-12. If the cladding and substrate are the same material, this is known as a symmetric waveguide.

2.4.1 Total Internal Reflection Principle

Optical waveguides are based on the principle of total internal reflection (TIR). The relationship is given by Snell's Law in Eq. 3 and describes the relationship between the angle of incidence and angle of refraction when light or waves passes through a boundary between two different isotropic media. n_1 and n_2 are the refractive indices of the two different materials, θ_1 is the angle of the incident wave and θ_2 is the angle of the refracted wave once it has interacted with the second material. A representation of how light rays interact with media is shown in Fig. 2-13.

$$n_1 \sin\theta_1 = n_2 \sin\theta_2 \tag{3}$$

Fig. 2-12 schematic of planar dielectric waveguide, with the core surrounded by two other refractive index materials known as the core and cladding.

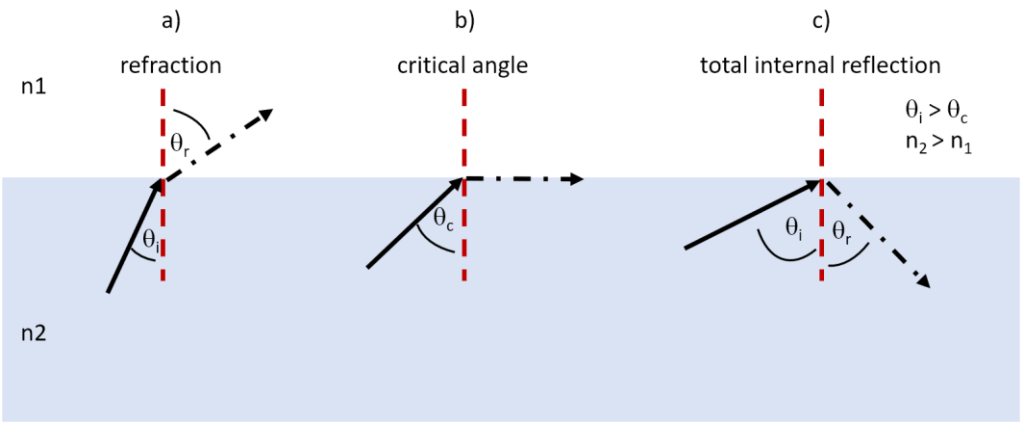

Fig. 2-13 depicts the interaction of light with a medium when under different angle conditions. a) illustrates refraction and the change in angle of the incident light after it interacts with the boundary of a medium with a different refraction index. b) shows how the light behaves when the critical angle conditions are met, the refracted light is perpendicular to the normal (i.e. 90˚), c) when the angles of incidence is exceeds the critical angle, the refracted wave is now fully reflected and remains within the initial material, demonstrating total internal reflection.

Where the refracted angle (θ_r) is 90 ˚, the incident angle (θ_i) is known as the critical angle (θ_c). Any angle which is incident that is larger than the critical angle will be fully reflected within the higher refractive index material. This is known as TIR. Certain conditions must be met for TIR to occur, the refractive index of the core material has a higher refractive index than its surrounding materials (cladding and substrate). Not all the light incident on the material will be guided or meet the TIR criteria, this can result in coupling losses from the waveguide. Waveguides guide light through their structures by TIR, the principles on which the light is guided are outlined in the following section.

2.4.2 Waveguiding principles

Light matter interactions are governed by the propagation of electromagnetic waves in materials and can be described by Maxwell's equations. Parameters for a waveguide can be found through solving Maxwell's equations, a more thorough description of these equations can be found in [52].

Waveguides operate by imposing constraints on the light propagating through a material, allowing only a finite number of wave patterns knows as guided mode solutions to propagate within the materials. These guided modes have a transverse

field pattern where the amplitude and polarization of the wave remain constant along the direction of propagation. The light guided by the waveguides can be categorised into transverse electric (TE) and transverse magnetic (TM) modes. The electric and magnetic fields of these waves can be described in Eq. 5 and 6 respectively. ν represents the mode number, $E_\nu(x,y)$ is the electric field mode profile in the x and y directions, $H_\nu(x,y)$ is the magnetic field mode profile in the x and y directions, and B_ν is the propagation constant of the mode.

$$E_v(r,t) = E_v(x,y)\exp i(\beta_v z - \omega t) \tag{5}$$

$$H_v(r,t) = H_v(x,y)\exp i(\beta_v z - \omega t) \tag{6}$$

These discrete modes are due to certain boundary conditions which allow only certain waves to propagate through the materials. Only selected angles of incidence can propagate within the waveguide and the number of guided modes depends on the thickness of the planar waveguide. B_ν determines how the amplitude and phase of the wave will propagate in the direction of travel. The propagation constant B_ν, is given by Eq. 7 where k_0 is the wavevector and n_{eff} is the effective refractive index.

$$\beta = k_0 n_{eff} \tag{7}$$

The travelling waves must interfere constructively for light to continue to propagate within the material and must be a multiple of 2π. The wavevector k_0, can be given by the Eq. 8.

$$k_o = \frac{2\pi}{\lambda} \tag{8}$$

From Eq 7. and Eq. 8, it can be seen that the propagation constant is a product of the effective refractive index of the waveguide and this incident wavelength.

Guided modes can only exist if the transverse resonance condition is satisfied where the repeated wave which is reflected due to TIR and interferes constructively with itself. In the optically active region of the waveguide the phase shift of the roundtrip of a transverse wave can be given in Eq. 9:

$$2k_1 d\cos\theta \tag{9}$$

Where d is the thickness of core material. Because the phase shifts (φ) that occur are functions of the angles of the propagating waves, the transverse resonance condition for a symmetric waveguide is as follows in Eq. 10

$$2k_1 d\cos\theta + 2\varphi_\theta = 2m\pi \quad (10)$$

The integer *m*, must be a whole number to multiply by 2π to meet the constructive interference criteria. Using the transverse resonance condition a waveguide can be tailored in its design (for example adjusting the thickness of the core region) so that only certain modes can propagate in the guide, and this can be used to design single or multimode waveguides for particular applications. When *m=0*, this is known as the fundamental mode, the other guided modes are known as the higher-order modes.

Chapters 3 and 4 employ a chip-based total internal reflection fluorescence microscopy (TIRFM) platform as the primary imaging technique. TIRFM is an optical method that emerged in the 1990s valued for its inherently low background fluorescence, which significantly improves the signal-to-noise ratio. Due to the lower background fluorescence, the surface sensitivity increases. Fluorophores are selectively excited near the waveguide surface leading to superior axial resolution in fluorescence imaging compared to confocal fluorescence microscopy. TIRFM delivers approximately a tenfold improvement in depth discrimination [53].

Owing to this high signal-to-noise ratio and reduced background interference, TIRFM has been widely used to study processes occurring at or near the cell membrane, including cell morphology, motility, and focal adhesions[54]. This is particularly advantageous in live-cell imaging, where minimizing phototoxicity and photobleaching is essential to preserve sample viability and integrity. High excitation intensities can accelerate photobleaching, particularly when high numerical aperture (NA) objectives are used [55]. Consequently, compromises must be navigated between spatial resolution and sample preservation when imaging live cells.

Evanescent wave based TIRFM techniques have been shown to provide an excellent alternative to more traditional microscopy techniques for live cell imaging. The evanescent wave excitation helps to reduce photobleaching and phototoxicity

though minimising the number of fluorophones which are excited within a cell at any given moment. The separation of the excitation light path from the detection path in evanescent wave techniques, allows for more simplified optical set ups and the opportunity for miniaturisation of imaging systems [56].Following the introduction of waveguides, theirphysics and TIRFM , the principles of the chemistry behind the functionalisation of the glass are briefly outlined in the next section.

2.5 Surface and amine functionalisation

Often a substrate requires modification to allow for probe molecules to be immobilised to the surface to be suitable for biosensing. The quality of the surface and this immobilisation will influence the sensitivity and selectivity of the bioassay. Immobilisation can be achieved through physical adsorption, covalent immobilisation, [57], [58] .

Physical adsorption onto a surface occurs due to forces between the probe molecule and substrate surface, however this process is reversible and means that repeated washing steps or long reaction times can have a detrimental effect on the overall functionalisation as these forces tend to be weak. Covalent attachment of biomolecules can be achieved through chemically active surfaces, and often chemical linker molecules used to facilitate this following several wet chemistry processes [58]. There are several approaches to aid this attachment of proteins to a surface, and in the case of the work presented in this thesis, silanisation was the method used to facilitate the covalent attachment.

Silanisation is the process of modifying silicon or glass substrates with a silane solution. The use of 3-aminopropyltriehoxysilane (APTES) solution is used to treat surfaces and act as a coupling agent [59]. This coupling results in the introduction of amine or thiol groups [60]. The introduction of amines provides the chemical linkers to be used to covalent attachment for the biomolecules. Covalent binding creates a strong bond between the substrate surface and the bound molecules so is more suited to a process where aggressive washing is required in the functionalisation

protocol. In this thesis ester-amine (N-hydroxysuccinimidyl (NHS) – amine) coupling is used to provide the attachment for the biomolecules.

2.6 Summary

This chapter has endeavoured to explain the main background concepts behind devices and materials used in this thesis. The design of the devices in chapters 3 and 4 primarily centred around utilizing a µLED device as the excitation source, which had a significant impact on the selection of materials. While the ultimate device proposed in the QuDos project discussed in chapter 6 did not achieve the integration of µLED devices, the initial intention was to incorporate µLEDs to facilitate choices in miniaturization. Throughout all the undertaken projects, the goal was to integrate µLEDs with hybridized elastomers containing quantum dots. Whenever necessary, each chapter in the portfolio provided a more comprehensive overview of the materials and methods used.

Chapter 3

3 MicroLED excitation of a waveguide biosensor with CQD fluorescent tags

In this chapter, we investigate a microLED-based biosensor that has the potential to be developed into a novel point-of-care diagnostic device. A μLED array is used as the excitation source, a glass slide as a waveguide and as the substrate for CQD-immunoassays, and a common smartphone as the fluorescence detector. Additionally, we aim to establish a limit of detection for the device to serve as a reference point for its practical application. The main results from this chapter were published in Biomedical Optical Express, "MicroLED biosensor with colloidal quantum dots and smartphone detection"[61].

3.1 Introduction

Point-of-care diagnostics (POC) is a growing technological area particularly within healthcare that aims to deliver rapid and accurate methods for detecting analytes without the delay that has come to be expected when using centralised laboratory

testing. When placed within healthcare settings, POC helps to aid faster clinical decisions and ultimately better treatment and care. As well as wanting to produce rapid and accurate results, another main feature that is sought after in POC diagnostics is cost effectiveness. Many diagnostic tests are required to be processed in a centralised laboratory that can take several days, whilst also requiring the expertise of a skilled technician to perform, leading to higher costs.

A big aim of developing POC diagnostics is to improve patient care and satisfaction [62]. Using POC can help to do this through earlier disease diagnosis and monitoring progressive conditions that can lead to better patient care and management and ultimately better health outcomes. Although the motivation behind this device is targeted more towards healthcare, other industries that could benefit from portable, rapid and accurate detection systems include water quality assessment [63], food safety [64], bioterrorism agent detection [65] and drug detection [66].

3.2 Why use point-of-care diagnostics

Ultimately POC diagnostics offer a means of testing that provides rapid results in environmental field settings. The primary advantage of these diagnostic tools is their ability to deliver faster results compared to those processed in a centralised laboratory. Several factors contribute to longer processing times for centralised laboratory tests, such as the duration required for the test to develop and provide results, the time taken to transport samples to a lab, and the wait for a specialised technician to conduct the test. In contrast, POC diagnostics can be performed in the field and processed with much shorter times, significantly reducing the turnaround time for obtaining test results.

Better access to portable and reliable devices can help to improve patient compliance by allowing patients to take ownership over aspects of their own health. Being able to perform a test in a person's own home versus the time and cost it can take to transport a patient into a primary health care settings benefit everyone. Another advantage of POC is the reduction in cost benefit for time savings and for diseases or

progression of diseases that can be detected at an earlier stage because of these devices. Faster diagnosis leads to greater patient satisfaction and potential lowering of treatments costs as more extreme methods of treatment that are more costly may not be required yet.

Development of POC diagnostic devices is ever evolving and targets for these types of devices are increasing all the time. Current functionality has been shown in these devices for detecting proteins; metabolites; nucleic acids; human cells; microbes and pathogens; and molecules used in the investigation for drug and food safety [66].

3.3 Optical Immunoassays

There are several different mechanisms through which analytes and pathogens are detected. Discussion here focuses on optical immunoassays, the most common types being enzyme linked immunosorbent assay (ELISA), chemiluminescence immunoassay (CLIA) and fluorescence immunoassay (FIA). In the following sections we will outline some of these different types of immunoassays.

3.3.1 Enzyme Linked Immunosorbent Assay (ELISA)

Simply put, ELISA's use enzymes to detect antigen-antibody reactions. An antibody will bind to an antigen that incorporates an enzyme tag. Following the antigen-antibody reaction, a colorimetric substrate is added and reacts with the enzymes, yielding a change in colour. The change in colour is related to the amount of bound antibody, and hence the presence and number of analytes.

There are several mechanisms that antigen-antibody reactions can be done through such as direct, sandwich, indirect or competitive techniques. In direct immunoassays the target antigen is detected using a single labelled antibody that has bound directly to the antigen. For sandwich immunoassays, the target analyte is" sandwiched" between two antibody counterparts. The first antibody will immobilise the antigen on a surface, and the other antibody in the sandwich will be a labelled antibody that can attach to another site of the target analyte. Indirect immunoassays are not labelled directly. An antibody for the target antigen is introduced to the sample to

bind. Once bound another labelled antibody which can bind to the first antibody is added to the sample. It is this second labelled antibody which will indirectly indicate the presence of the target of interest. This method is typically used when no labelled antibody for the target is available. For a competitive assay a known amount of the same analyte which is labelled is added to the sample. As there is an equal number of labelled and unlabelled analytes competing to bind to a limited number of antibodies, the amount of labelled analyte which can be detected is inversely proportional to the target analyte concentration. These can be used to determine the presence of an analyte when low concentrations are involved. In short the purpose of immunoassays is to identify and quantify the presence of molecules in biological fluids [67]. ELISA's exploit antigen-antibody reactions as it is almost impossible for antibodies to be bound to another molecule apart from its own antigen counterpart. The presence of an analyte is typically detected through a colorimetric change to a colourless substrate when the enzyme labelled antibody when it is presented. The degree of colour change is quantified and is directly proportional to the quantity of antigen present. The colour changes can be measured using a spectrophotometer to determine the absorbance or optical density of the substrate or through comparison to a standard curve of known amounts of the antigen [68].

3.3.2 Chemiluminescent Immunoassay (CLIA)

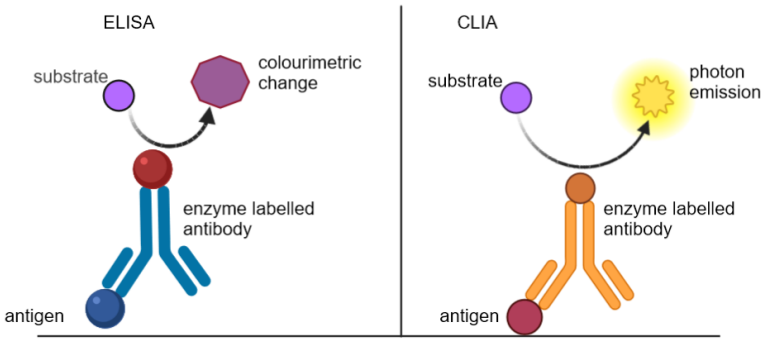

Fig. 3-1 Schematic of the detection mechanism of an ELISA vs CLIA. The ELISA uses enzymes to produce a colour change on a substrate to determine analyte presence, whilst CLIA produces a chemical reaction to emit photons when the presence of an analyte is detected.

CLIA works through a similar mechanism to an ELISA with the main difference being, the label that binds to the antigen relies on a chemical reaction that produces light to indicate presence of the analyte, rather than a colorimetric change. Like an ELISA, CLIA has high sensitivity and specificity [69], [70]. The intensity that the label emits light at allows a determination of the concentration of the analyte being detected [70]. A schematic showing a comparison between an ELISA and CLIA is shown in Fig. 3-1

3.3.3 Fluorescence Immunoassay (FIA)

FIA is another similar technique to ELISA and CLIA that relies upon the principle of fluorescence for detection rather than a chemical or enzyme reaction like in CLIA or ELISA. Fluorescent molecules (fluorophores) are used as the tags that attached to the antibody to indicate the presence of the antigen through the emission of light when excited by an external source. The intensity of the fluorescence emitted is directly proportional to the amount of target molecule which is present. Normally FIA provides sensors which are high in sensitivity, have a wide dynamic range of wavelength of emitters and have great potential for multiplexing. There is a wide variety of different fluorophores which can be used for this type of immunoassay which include organic dyes, quantum dots, silica nanoparticles, and gold or silver nanoparticles [71].

FIA's could allow for miniaturisation of biosensors by taking advantage of progression in excitation sources such as LEDs. The footprint of the excitation source can be made considerably smaller by using µLEDs instead of laser diodes or LEDs. Using µLEDs would also reduce the need for additional optics to couple the excitation light into the sample. As the presence of analytes can be determined through the intensity of fluorescent emission alternatives to traditional detection methods can be considered, for instance, the camera capabilities of modern smartphones can allow for these devices to be used as compact detectors. In the next section we will outline the concept and design of a compact fluorescent biosensor which utilises µLED

excitation with smartphone detection. A table summarising the different types of assays and their variants are shown below in ***Table 1***.

Table 1 Comparison table of Immunoassay techniques and their variants

Technique	Variant	Principle	Detection Method
ELISA	Direct	Antigen is immobilised, labelled enzyme binds directly to antibody	Colour change via enzyme substrate
	Indirect	Primary antibody binds to antigen; enzyme-linked secondary antibody detects	Colourimetric
	Sandwich	Capture antibody binds antigen; detection antibody binds antigen	Colourimetric
CLIA	Direct	Chemiluminescent-labelled antibody binds directly to target	Light emission via chemical reaction
FIA	Direct	Fluorophore-labelled antibody binds directly to antigen	Fluorescence emission

3.1 Concept and design

In this section, the concept and design of a compact µLED-based sensor is presented. The proof-of-concept uses total internal reflection fluorescence (TIRF) within a µLED platform similar to one previously designed for phototherapy applications [72]–[74]. The concept of TIRF is outlined more in section 3.2.3. A schematic of the sensor concept is shown in Fig. 3-2. The platform is a simple slab waveguide using a functionalized glass microscope slide that is butt-coupled to an optical excitation source. A blue emitting, GaN µLED array is used as the excitation source. Guided light from the excitation source interacts with the assay on the glass surface by evanescence. Any resulting luminescence from the assay can be detected from the top or bottom of the glass plate, for example with a camera.

Using a µLED will allow future iterations of the device to be battery operated which would be a crucial element needed for miniaturisation and portability. This is due to µLEDs being able to deliver similar optical power density at lower current, meaning fewer batteries would be required for operation compared to traditional LEDs or a laser diode. With a bid to work towards a device that could be employed easily in primary care or field-based applications, a smartphone was used to investigate viability for a detection device. Another element of the design that would make miniaturisation more possible by using µLEDs, is the small emitting size of the µLED pixels enables efficient light coupling without the need for any intermediate optics. In this platform, fluorescence emission from the conjugated QDs used for the assay is detected from the top with a smartphone camera.

Modern smartphones have powerful built in capabilities such as internal operating systems, internal memory, high quality camera lenses, their own built in illumination, and communications connectivity [65], [76]. In comparison to laboratory devices they are cheaper and more readily available [77] whilst being portable and low cost and without the requirement for specialist operation in comparison to microscopes or spectrophotometers. Due to these properties, smartphones bring an inherent adaptability to any device they are integrated in to, making them a reasonable choice

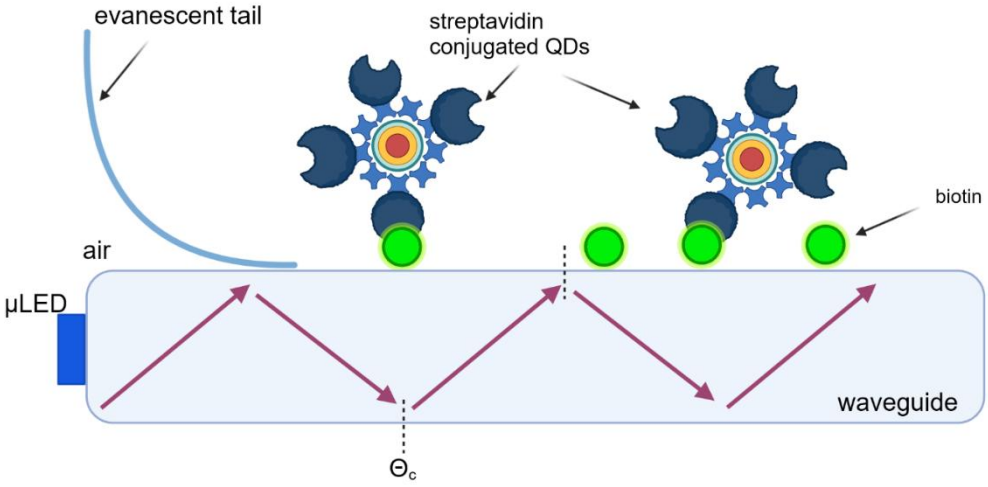

Fig. 3-2 illustrates a functionalised glass waveguide with biotin on the surface bound to the streptavidin QDs, while butt coupled to the LED. A representation of how the excitation light will undergo TIR is represented by the arrows within the waveguide and how the evanescent tail will extend from the surface to excite the SA-QD tags.

for an optical sensor for a potential POC diagnostic. When considering a smartphone as an optical sensor, the trade-off between the accuracy versus the cost is a critical component when assessing the plausibility of a smartphone as a detector and viability will be dependent on the application the smartphone is being used for.

The CMOS sensors of smartphones respond to red (R), green (G), and blue (B) wavelengths of light, that allows for detection of changes in fluorescent intensities at different wavelengths. We take advantage of this capability to spectrally discriminate between the blue (444 nm) excitation light from the µLED array device and the red fluorescence from bio-conjugated colloidal quantum dots [78], [79]. The spectral response of camera sensor used in the Samsung Galaxy S9 is shown in Fig. 3-3. The data used for this figure is provided by [75]. It must be noted that due to the vast differences in smartphone camera sensors, calibration of the spectral sensitivity of differing models of smartphone would be required so that images from different

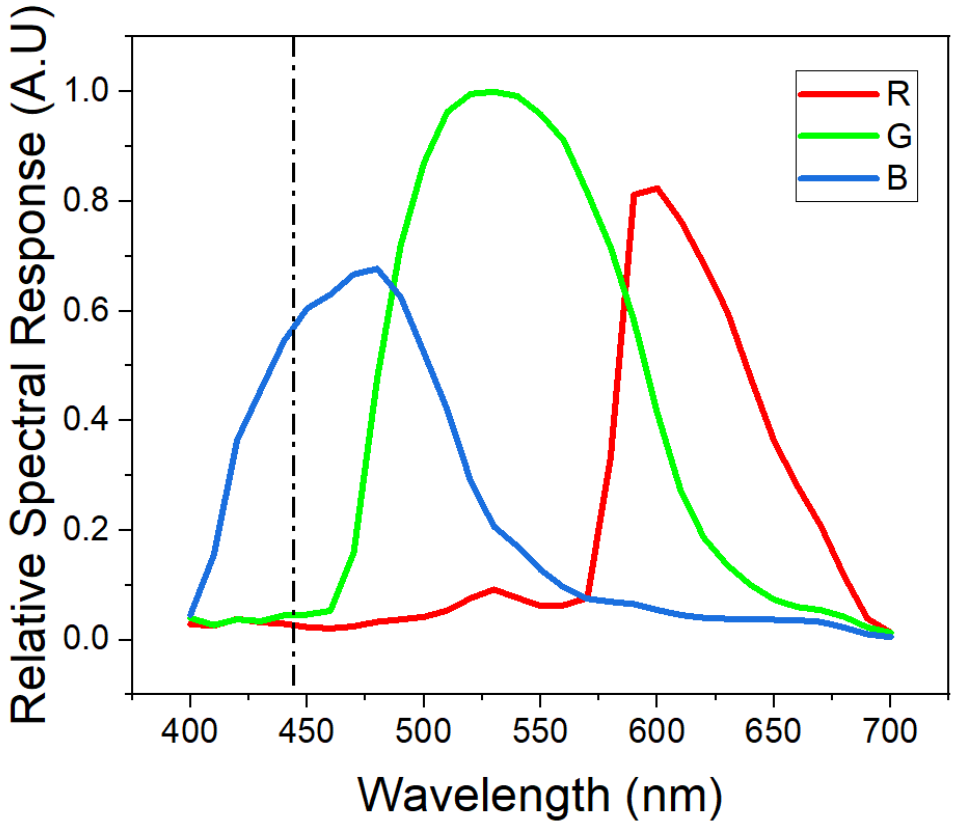

Fig. 3-3 Data from [75] **of the relative spectral sensitivity of the Samsung Galaxy S9 smartphone. The dashed line represents the spectral emission peak of the µLED used in this thesis at 444 nm**

would give conclusive results when considering these devices for POC [75] or wider availability.

3.2 Experimental Methods

3.2.1 µLED Design Choices

The µLED used in this work is a flip-chip GaN array, with a custom 1 x 10-pixel array design. This configuration of pixels was chosen for the platform to ensure maximum coupling into the dimensions of the slab waveguide. An image of the µLED is shown in Fig. 3-4. The µLED array is wire bonded to a printed circuit board (PCB). The PCB is 25 x 50 mm^2 and has SubMiniature version A (SMA) connectors to link to an external current source for ease of demonstration. Although this experimental set-up is currently still bench top, the system has been designed such that future implementations of the platform would allow for miniaturisation of the PCB and could be further reduced to incorporate a battery for portable operation.

The pixel size of the emitter is 100 x 100 μm^2, a 1 x 10 pixel design as seen in Fig. 3-4, ensures that coupling into the glass slide is maximised as much as possible, through a horizontal configuration of pixels, mimicking the shape dimensions of the glass slide. Although the physical size of the emitters is 100 x 100 μm^2, the emissive area is equivalent to 300 x 300 μm^2 due to diffraction of the light through the sapphire substrate [80]. This emissive area is related to the sapphire substrate thickness, which is approximately 300 µm in this case. Fig. 3-5 highlights how the individual emitter emission enters the glass slide following diffraction through the sapphire substrate.

Fig. 3-4 Image of GaN µLED showing 1 x 10 pixel array design. Scale bar show is 2 mm.

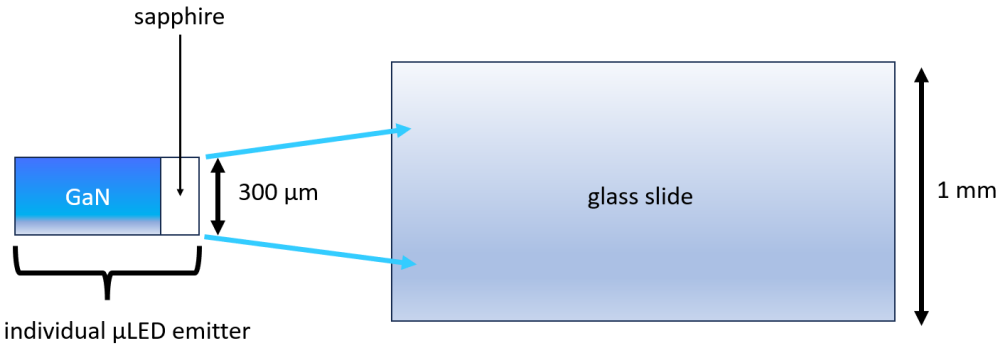

Fig. 3-5 schematic representation (not to scale) of the pixel emission into the glass substrate from the GaN pixel which is 100 µm by 100 µm, and the subsequent scattering of the light through the sapphire substrate to give an emissive area of 300 µm by 300 µm at the sapphire output.

With the dimensions of the glass slide being 76 x 26 x 1 mm^3, the vertical height of the µLED emission needs to be smaller than 1 mm (the thickness of the glass slide) to ensure the coupling can be maximised. With the set-up there is less restriction in the horizontal plane for the µLED shape, and more pixels could be added to make a longer design and ensure better "filling" of the waveguide with the excitation light in the horizontal direction. Although adding more pixels would be desirable for coupling, consideration needs to be given to the overall power consumption of the device, and adding too many pixels will impact the power consumption on the µLED, and would increase requirements for battery operation.

Therefore, the final design of the µLED was a 1x10 array format of µLED emitters (or pixels), the dimensions of the active region of each pixel being 100 x 100 μm^2. The spacing between each pixel is 720 µm (centre to centre) and the pixels are contacted in parallel. The µLED array is of a flip chip design with emission through the sapphire substrate. A schematic is of a flip-chip µLED is shown in Fig. 3-6.

The µLED in this thesis share a common p and n contact which means that all the pixels will either be on or off, and as stated previously they are contacted in parallel. As the pixels are contacted in parallel this means the supplied current is shared between each pixel. Although parallel contacting will mean a higher operating current which increases the risk of damage to the device from overheating, it allows for lower voltages, meaning fewer batteries would be required to power the device. This would lead to a smaller and more compact final device.

3.2.2 Characterising the µLED

Before implementation in the system, the µLED was characterized using a pair of aspheric condenser lenses (AC4532-A, Thorlabs) with a diameter of 45 mm, a focal length of 32 mm and numerical aperture of 0.612, to collect and image the emission onto a detector. To measure the power of the µLED, the detector was a silicon photodetector (Thorlabs, S121C), this could then be swapped to a fibre coupled spectrometer (OceanOptics, USB 4000) to measure the emission spectrum. An image of a µLED, with the lens pair and the detector are shown in Fig. 3-7 a) and a schematic shown in Fig. 3-7 b). The optical output power was measured by increasing the current in incremental steps of 10 mA, while the supplied voltage and optical power were recorded from the photodetector.

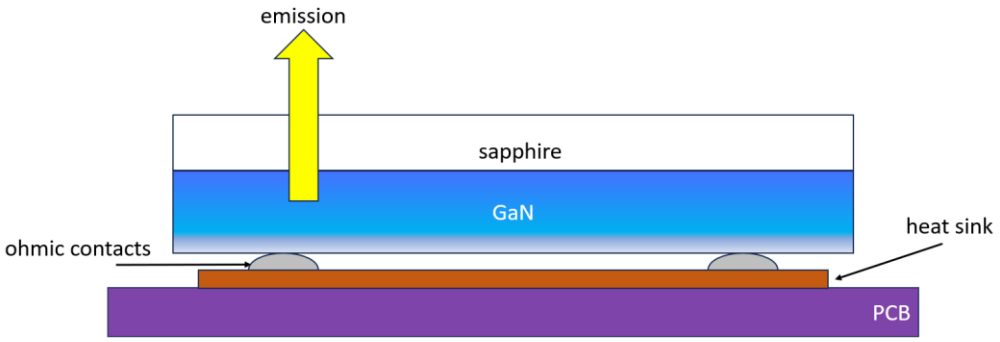

Fig. 3-6 Flip chip LED schematic. The GaN substrate is mounted directly onto the ohmic contacts, with the heat sink and PCB contacted so that when electrically driven the emission from the GaN is through the sapphire substrate.

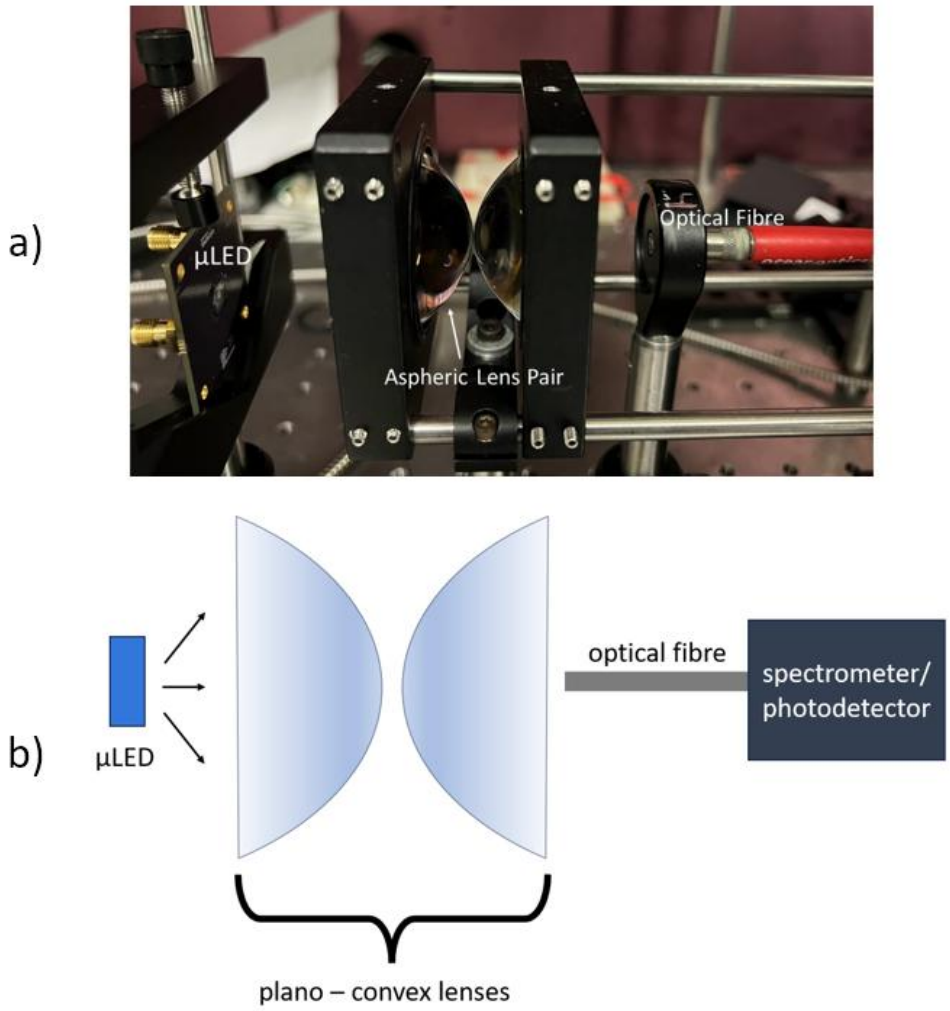

Fig. 3-7 a) Image of lens collection system used for µLED characterisation. The µLED light is collected and collimated using a pair of condenser lenses and either focussed into an optical fibre or onto a silicon photodetector b) schematic of the µLED characterisation set up.

The maximum output power, limited by thermal roll-over, is 23 mW reached at a drive current of 450 mA. For the sensing experiments, the µLED was driven either at 80 mA (7.5 mW) or at 120 mA (10 mW). Fig. 3-8 a) plots the output power vs. current, and the current vs. voltage of the µLED device. The emission from the µLED is centred at 444 nm with a full width half maximum (FWHM) of 25 nm, as shown in Fig. 3-8b.

3.2.3 Total Internal Reflection Fluorescence

The basis for the design of the biosensor is related to TIRF. This kind of excitation exploits the evanescent field that is produced when light is incident on a dielectric medium where a material of high refractive index (RI) is surrounded by a material of lower RI and total internal reflection (TIR) conditions are met. TIR is outlined in more detail in section 2.4.1. Fluorophores can be placed on the surface of the higher RI material and are excited by the wave that is extending from this material. The

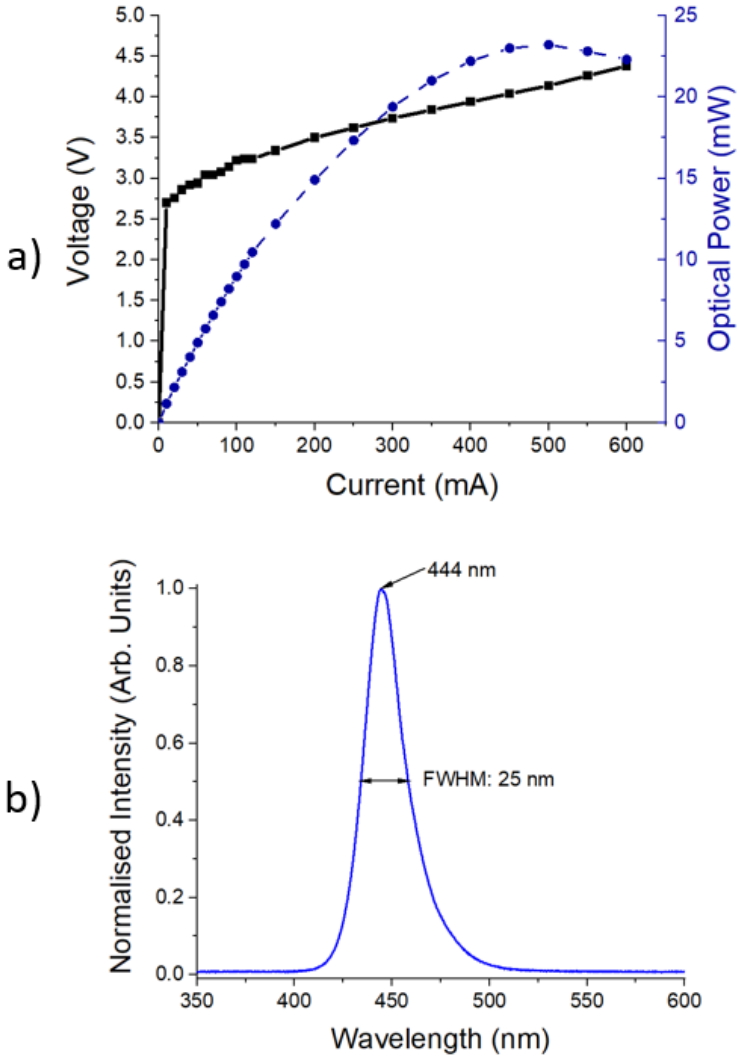

Fig. 3-8 a) graph of measured data for µLED, square points represent the current vs voltage relationship and the circular data points indicate the optical power output and its correlation with current changes. b) µLED photoluminescent emission spectra, with a peak emission wavelength of 444 nm and FWHM of 25 nm.

evanescent wave that extends from the material is what excites the fluorophores on the surface and due to the small penetration depth of this wave the background noise is reduced and sensitivity improved [81]–[83], without excess excitation light due to a thin excitation volume. In contrast to direct fluorophore excitation, TIRF geometry minimizes autofluorescence and background noise caused by direct excitation light [81]–[83].

3.2.4 Waveguide material

A standard silica glass microscope slide with dimensions 76 mm by 26 mm and a thickness of 1 mm was chosen as the waveguide platform. As standard microscope slides were used, the edges must be polished otherwise coupling efficiency is lost to scattering if rough edges were used.

3.2.5 Streptavidin – Biotin Bonding

The binding pair that was used in this demonstration was biotin/streptavidin as it has a well-understood coupling mechanism with strong affinity binding and is commonly used for demonstrating the capabilities of novel biosensors [84]. These two proteins bind together readily and have a strong binding affinity of 10^{-15} M, which makes this pair stable and able to withstand difficult reaction conditions such as aggressive washing. Another advantage of using biotin as the analyte capture molecule is the possibility of using it to attach other antibodies through a process known as biotinylation to allow for further functionality and multiplexing [85].

3.2.6 Sensor Waveguide Fabrication

3.2.6.1 Glass Functionalisation

Due to the availability of commercially available conjugated CQDs, biotin was attached to the glass slide to allow binding with streptavidin conjugated QDs. For the functionalisation process to be possible, surface bonds need to be created on the silica glass allowing other molecules to bind to the glass surface, known as hydroxylation. To achieve this the glass was plasma treated using an air mixture. A schematic of the functionalised waveguide is shown in Fig. 3-2. The slides were placed

in a plasma reactor (Diener Atto Plasma Surface Treatment Machine) for approx. 30 s @ 20 W, 1 mbar pressure. Once the surface bonds of the glass have been released to create hydroxyl groups, the glass is silanised by dipping into a solution of 3-aminopropyltriethoxysilane (APTES) (2% v/v in de-ionized water) and incubated for 2 hours. The glass slides were then rinsed in de-ionized water (DI), dried with a nitrogen aspirator gun, and placed in an oven at 80 °C for 5 minutes to cure the APTES layer. As APTES adds functional amine groups through the process of silanisation the analyte can now be bound to the glass through this amine group. The N-Hydroxysulfosuccinimidobiotin (NHS-Biotin) powder (Sigma Aldrich Biotin-NHS, Water-Soluble) was mixed with phosphate buffer saline (PBS), (Fischer BioReagents, Phosphate Buffered Saline, 1X Solution, pH 7.4), to a concentration of 1 mg/ml. 1 ml of the solution was pipetted onto the surface of the glass and left to react with the surface. Following this, excess NHS-Biotin solution was rinsed using PBS and DI water respectively and then dried with the aspirator. To reduce the non-specific binding and improve the sensor's sensitivity, a solution of 4% bovine serum albumin (BSA), (Thermo Fisher, Blocker BSA (10X) in PBS), was used to fill the gaps where no biotin is present on the glass surface. Non-specific binding can cause issues with sensitivity and background noise by causing binding of undesired analytes to a sensor surface. Ultimately this could result in false positive/negative results and lead to misdiagnosis, so steps should be taken to minimise this effect. The glass was left to soak in solution for 2 hours. Once removed from the BSA solution, the glass slides were rinsed again with PBS and DI water and dried.

3.2.6.2 Quantum Dot Tags

Semiconductor colloidal quantum dots (CQDs) offer several advantages as fluorescent tags, such as high quantum yield, broad absorption, high resistance to photobleaching. The ability to tailor their size means their fluorescent emission can cover wavelengths ranging from the ultraviolet to infrared spectrum [86] and emission properties can be customised according to the application. More details about quantum dots have been presented in section 2.2.

As the binding pair that we have chosen for the demonstration is biotin/streptavidin, the fluorescent tags used in this concept are streptavidin conjugated colloidal quantum dots (SA-QDs) and were purchased from Invitrogen. The QD material consists of a cadmium selenide (CdSe) core, surrounded by a zinc sulphide (ZnS) shell. As the QDs need to be suitable for biological applications, the nanocrystal is coated with a polymer-shell that renders the QD material hydrophilic and biologically safer. The polymer shell also provides the site for streptavidin surface conjugation [87]. The emission wavelength peak of the quantum dots (QDs) is 655 nm, allowing enough spectral separation for the camera to discriminate between the blue excitation light and red fluorescent emission of the SA-QDs.

3.2.6.3 Binding SA-QDs

Following functionalisation with biotin, the next step in the sensor fabrication was immobilization of SA-QDs (Invitrogen, Qdot 655 streptavidin conjugate). First the SA-QDs were diluted from their stock concentration of 1 µM, to solutions that range from 100 nM to 1 nM, using 4% BSA. A 3x5 array of one concentration of SA-QD solution was pipetted onto the glass, the format is shown in Fig. 3-9. The volume of solution used was 0.5 µL for each region dropcast. One glass slide per concentration was used to determine an average of the mean pixel intensities for each concentration. The SA-QDs were left in contact with the surface for 30 seconds after deposition and then rinsed. The glass slides were rinsed by repeated dipping in 4% polysorbate 20 (Tween 20, Fisher BioReagents), followed by PBS then DI water; this

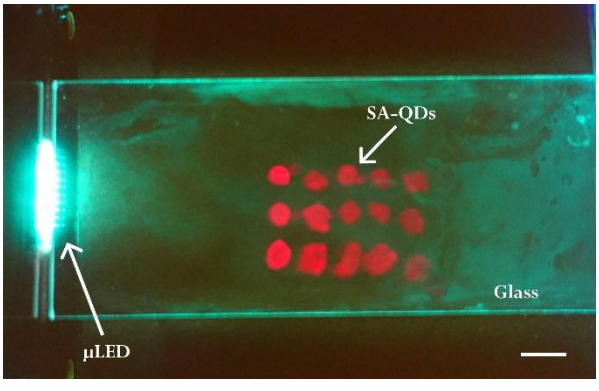

Fig. 3-9 Top-down view of glass sensor showing 3x5 array of SA-QDs taken with Samsung Galaxy S9. (5 mm scale bar)

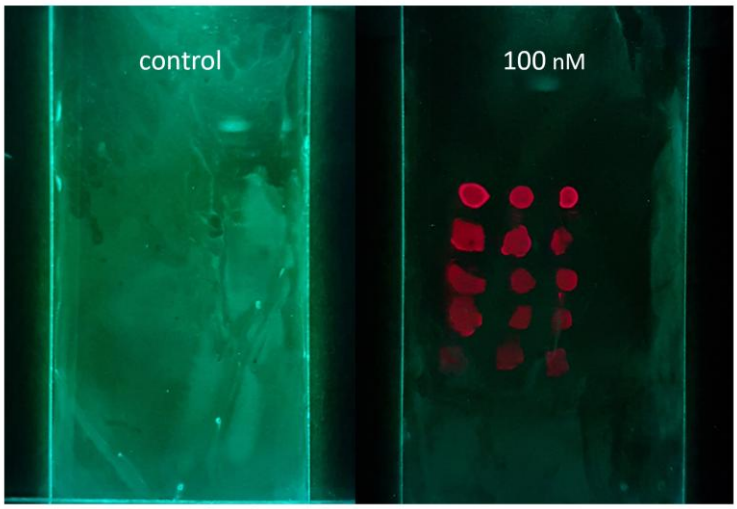

Fig. 3-10 comparison of a control slide with no biotin present during the functionalisation process to a glass slide containing biotin where the SA-QDs (concentration of 100 nM) have bound to the surface functionalised with biotin.

was repeated 3 times to ensure all excess was removed. The glass slides were left to dry fully before images were captured.

A control slide was also fabricated along with the functionalised glass slides to confirm that the SA-QDs present after rinsing were due to binding to biotin rather than non-specific binding to the glass surface, shown in Fig. 3-10. The same protocol was followed for fabricating the control slide, but biotin was omitted. When imaging the control slides, no fluorescence from the SA-QDs was observed, therefore it was determined through the absence of SA-QDs emission that non-specific binding was negligible in our experiments.

3.2.7 Smartphone Selection

Table 2 Camera Specifications of Samsung Galaxy S9

Camera Feature	**Specification**
Sensor	12 Megapixels, dual pixel autofocus and optical image stabilisation
Aperture size	f 1.5 / f 2.4
Sensor size	1/2.55”

Pixel size	1.4 µm

The model of smartphone used as the detector was a Samsung Galaxy S9. When released in 2018 the main camera had some of the best camera features available in a smartphone. The camera specifications are listed in **Table 2**. With these features the ability to select, exposure time and aperture settings, in the camera pro mode meant that there was greater control of the camera parameters, allowing for finding a good limit of detection (LoD) were possible. Since 2018 smartphone camera features have improved, however many of these improvements have been made using software enhancements.

3.2.8 Top-Down Spectral Irradiance Measurements

To determine the best area of the glass to drop cast the SA-QDs to realise the assay, a "guiding profile" of the glass microscope slides was assessed to ensure minimal background interference. The glass slides were subject to scattering of the excitation light close to the edges of the glass microscope slides meaning that the coupled light would not be maximised to excite the QDs on the surface in these areas.

To determine this area of the glass slide, we measure the spectral irradiance of the excitation light from the top surface of the device before the assay is performed. It is noteworthy that the spectral information of the light is often overlooked, and sensitivity may vary based on wavelength. This variance can lead to the underestimation or overestimation of power, particularly for broadband light sources. To address this issue, spectrometers can be calibrated to known light sources. This calibration allows the measurement of spectral irradiance in µW/cm²/nm. The process involves carefully characterizing calibration light sources to provide a known quantity of light at each wavelength with minimal uncertainty error. In our case, the spectrometer is calibrated to a tungsten-halogen light source (OceanOptics, HL2000), which is radiometrically calibrated to a NIST standard, ensuring the absolute irradiance spectrum is known. The spectrometer records the spectral response from 350 nm to 1150 nm. The spectral response of the light source can then be integrated over the desired wavelength range, and the spectrometer's

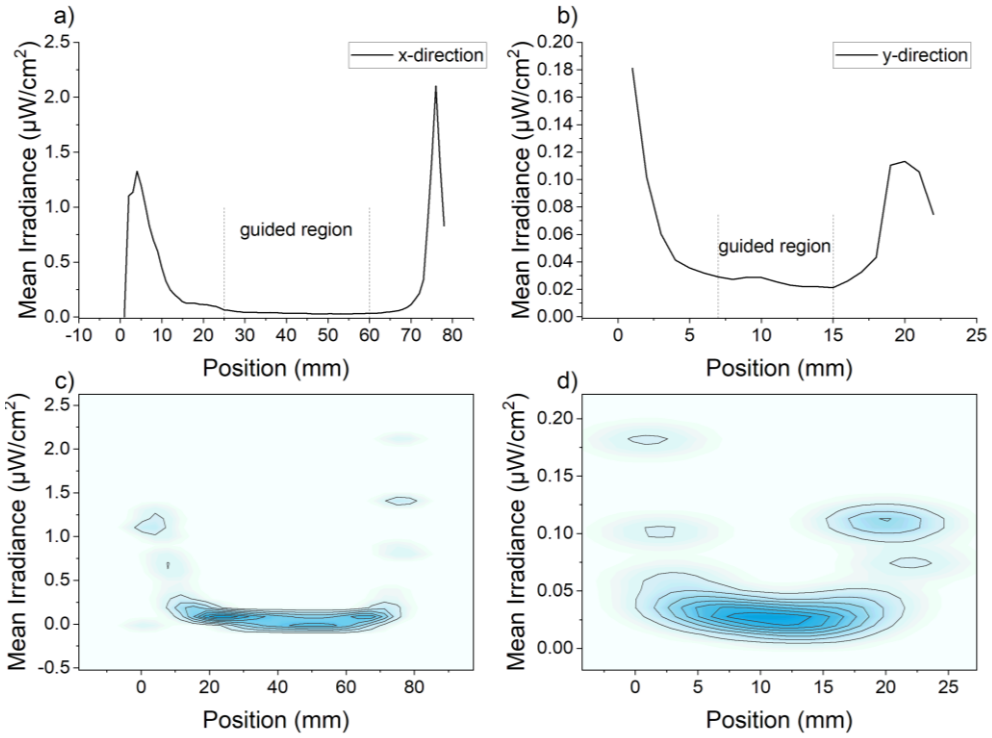

Fig. 3-11 Graphs of spectral irradiance measurements taken on a plain glass microscope slide in the a) x – direction and b) y- direction. Both directions have higher spectral irradiance values at the edges of the glass slide with the lowest values seen in the middle, indicated on each graph by the guided regions. The higher values of irradiance seen between 0 mm and 20 mm is caused by the unguided light from the µLED being scattered out of the slide, the irradiance that can be measured outside the glass is due to the evanescent wave extending from the surface which is exploited to excite the QDs c) and d) show the corresponding 2D intensity plots for a) and b) respectively to give a graphical representation of the area of highest intensity within the waveguide.

response is adjusted to give irradiance output of the lamp. This calibration process generates a calibration file, which is subsequently applied to every measurement.

The spectral irradiance of LED light emitted from the top of a glass microscope slide was measured using an optical fibre placed 4 mm about the glass surface. An xyz stage was used to move the optical fibre along the centre of the glass slide in 1 mm intervals – in the x direction, for the full length of the slide (76 mm). The µLED was driven at 120 mA current while a microscope slide was butt-coupled to the sapphire surface. An Avantes spectrometer (Avantes, Starline AvaSpec – 2048L) was calibrated and used to measure the spectral irradiance of the guided modes scattered from the top surface of the glass slide. Once all the measurements had been collected, the

data was integrated over the desired wavelengths (400 – 500 nm) and the irradiance measured from the top of the glass was plotted against the position. This process was repeated for the width of the glass slide – y direction, (26 mm), at 45 mm from the butt-coupled edge (in the x direction). These plots give an indication how the light entering the glass slide is guided and coupled into the material. The measurements were carried out on a plain glass slide and then repeated with a functionalised glass slide without the SA-QDs present to determine if any difference in scattering or transmission was noticed.

A plot of the irradiance for the x – direction and y – direction of a plain glass slide is shown in Fig. 3-11 a) and b) respectively. The position is given by the parameter x (y), in mm, where x (y) = 0 mm is the facet where the µLED array is butt-coupled. In Fig. 3-11 a) at the zero position the irradiance is higher, this is due to scattering from the edge of the waveguide surface and the proximity of the collecting fibre to the µLED. The decrease in irradiance between 0 mm and 20 mm is mainly caused by the unguided light leaking out of the slide, with a smaller contribution coming from the diffraction in the plane of the waveguide, as the coupled light spreads and fills the slide's cross-section as was demonstrated by Zemax simulation in [73] . Although it can be seen from 25 mm to 60 mm in the x – direction, the measured top irradiance is low and appears mostly constant; as there are small propagation losses, there is a small decreasing trend (see next sub-section). At 75 mm there is an increase in the irradiance, this is due to light exiting the waveguide and increased scattering due to surface roughness at the edge of the glass microscope slide. The measurement of the top irradiance in the y – direction has a similar trend with edge effect and a low, almost constant value between 7 mm to 15 mm. There is an area of the glass slide in the x and y direction that is mostly constant, i.e. between 25 mm < x < 60 mm and 7 mm < y < 15 mm, suggesting that this is the area where the light is guided within the glass the best. It is within this central area of the glass that it was determined that the SA-QDs are best placed for excitation without excessive background light being present.

This measurement was then repeated after biofunctionalization of the glass slide, a comparison of the mean irradiance between a functionalised glass slide and plain glass slide are shown in Fig. 3-12. While the scattering of light results in higher irradiance values being emitted from the surface the irradiance is still homogeneous within 30%.

3.2.9 Propagation Loss

The propagation losses of the µLED light guided in the x direction were measured using the cut-back method [88] on a plain glass microscope slide. The glass waveguide was butt-coupled to the µLED array while being driven at 120 mA. The spectral irradiance emitted from the end facet of the waveguide was measured using an optical fibre connected to a spectrometer (Avantes, Starline AvaSpec – 2048L). The initial measurement was taken at the original length of the glass waveguide at 76 mm. The length of the glass was then cutback by 6 mm, and the spectral irradiance was measured at 70 mm. This cutback process repeated at 10 mm intervals until the glass waveguide was 20mm long. Spectral irradiance data was then integrated over the desired wavelengths (400 – 500nm) and irradiance values were plotted against position. Fig. 3-13 plots the results; it was fitted using an exponential decay giving a

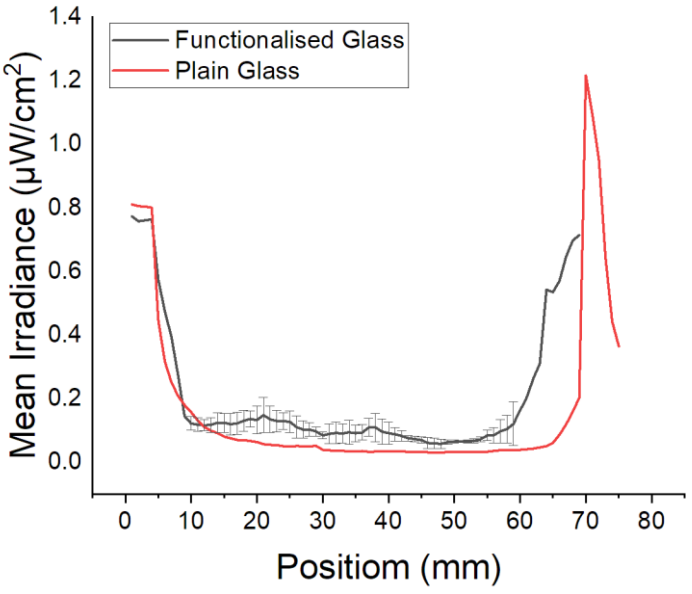

Fig. 3-12 comparison of the mean irradiance for a functionalised glass slide and plain glass slide in the x-direction

loss for propagation through the glass of 0.2 cm^{-1}. The irradiance value at x = 0 was extrapolated from 10 mm, as the optical fibre could not be moved any closer to the µLED due to the dimensions of the holder which restricted measurements being carried out at 0 mm from the µLED. Although still relatively homogenous, the propagation loss is higher, estimated at 0.36 cm^{-1} (This value could not be measured on a functionalised glass slide with the cutback method due to time constraints).

3.2.10 Estimating Power Loss and Coupling efficiency

An estimate of the propagation loss through the waveguide was obtained using data from the cutback method [88], as described in section 3.2.9. To estimate the coupling loss, the data of Fig. 3-13. was extrapolated to x = 0 to give a value for the irradiance that is coupled into the glass slide. The irradiance coupled into the glass was given to be 3.8 mW/cm^2. When taking the cross section of the slide into account, this corresponds to an optical power of approximately 1 mW ($P_{(guiding\ irradiance)}$) for the

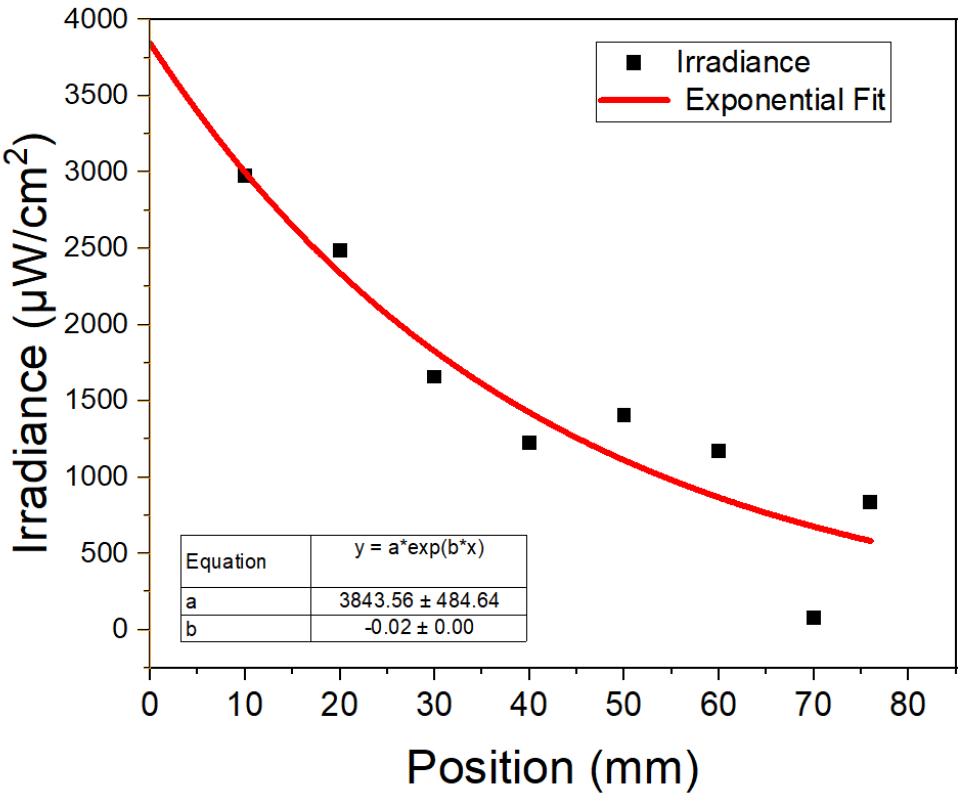

Fig. 3-13 Graph of irradiance values through a plain glass microscope slide. Propagation loss is calculated using an exponential fit to give a value of 0.2 /cm when extrapolated to x=0.

glass. Given this estimated power coupled into the waveguide and knowing the LED optical power ($P_{(\mu LED)}$) is 10 mW, using Eq.11, the coupling efficiency is given to be 10%.

$$n = \frac{P_{\ (guiding\ irradiance)}}{P_{\ (\mu LED)}} \tag{11}$$

3.2.11 Biosensor Platform

An image of the biosensor platform and a schematic of the same setup is shown in Fig. 3-14 a) and b) respectively. Again, the blue GaN µLED that has been described in 3.2.1 is used as the excitation source for a simple slab waveguide, that consists of a functionalised glass microscope slide, and a Samsung Galaxy S9 as the detector. This fluorescence is then detected by the smartphone camera which is placed 90 mm above the platform to image the glass surface. The fluorescent intensity is directly linked to the number of fluorescent tags immobilized on the surface.

3.2.12 Imaging the waveguides

To measure the intensity output of the SA-QD regions the µLED was operated with a driving current of 120 mA to establish limit of detection measurements, and to

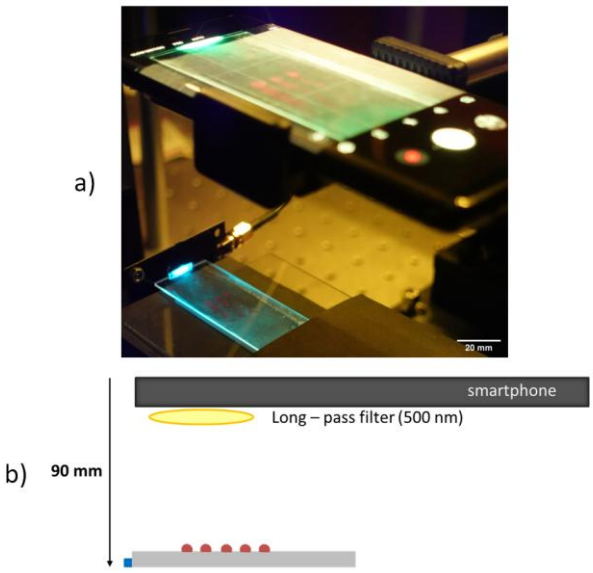

Fig. 3-14 a) Image of biosensor set up, µLED butt-coupled to glass slide, with smartphone set at 90 mm above glass. b) Schematic of the biosensor experimental set up. The smartphone images the sensor at 90 mm above the glass microscope slide with a 500 nm long pass cut off filter covering the camera lens to filter excess blue pump light.

compare the effect of different exposure times on the measured intensity. To determine the effect of a lower driving current on intensity output, the glass slides were also imaged with the driving current set to 80 mA. Each microscope slide contained 15 regions of one SA-QD concentration (5 rows of 3 drop-casted regions), as described in 3.2.6. To obtain an intensity value for each concentration, the fluorescence intensity of these 15 regions was averaged. Fig. 3-14 b) shows a schematic detailing the experimental set-up for imagining the glass slides. The smartphone is placed at a fixed height of 90 mm above the sensor membrane, with a long pass filter (Thorlabs, FEL 500) covering the camera window with a cut off wavelength of 500 nm. Each glass slide was imaged 3 times, after de-coupling and re-coupling to the µLED, so repeatability could be assessed. The image seen on the screen of the smartphone via the camera app, appears green rather than blue due to the 500 nm cut off filter placed in front of the camera lens which is removing the excess pump light from the µLED, leaving the green tail of the µLED to be imaged.

The camera settings for the smartphone that were used experimentally are outlined in **Table 3** and were set using the in-built pro mode in the camera software. Images were saved as JPEG files.

Table 3 Samsung Galaxy S9 Smartphone Pro Mode Camera Settings

Sensor Settings	**Value**
ISO	800
Exposure Time	50 ms, 250 ms ,1000 ms
Zoom	2x
Aperture	f/1.5

3.2.12.1 Image Processing

JPEG images were converted from their native RGB format, into an RGB stack using ImageJ software. An RGB stack separates the combined colour image into individual greyscale images for each of the R, G and B channels. When the images were converted into a stack, the individual R, G, B channel information could be processed

independently. The areas of red fluorescence were selected manually, and the pixel intensity information was averaged over this selected area. This was done for each of the 15 SA-QD regions on the sensor and the intensity values for each of these regions was then averaged to give a mean pixel intensity per concentration. The results are presented in section 3.3.1. Each of these measurements was conducted in triplicate, involving the decoupling of the glass slide from the µLED and the subsequent recoupling of the slide between each measurement. The results were then averaged to assess the repeatability of intensities for a specific concentration and determine the standard deviations associated with each concentration.

3.3 Biosensor Results

3.3.1 Determining the Limit of Detection for the Biosensor

Fig. 3-15 shows the pixel intensity data from an RGB image before conversion to a

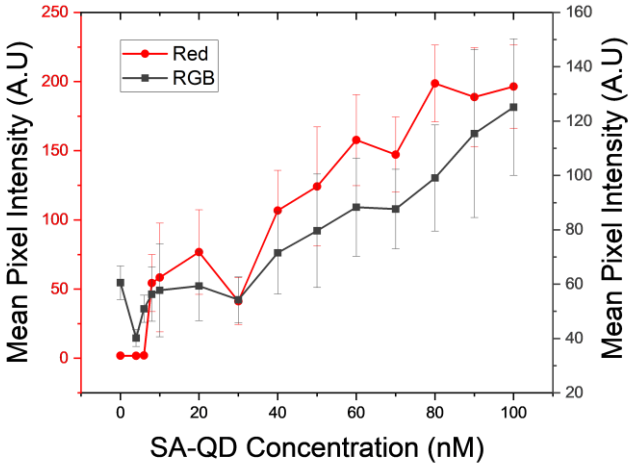

Fig. 3-15 Graph detailing the RGB mean pixel intensity data compared to red channel data only. The graph shows a linear trend of increasing mean pixel intensity as concentration increases for both sets of data

stack, and the pixel intensity for the red channel, plotted against the known concentration of the SA-QD solution when it was drop-cast. The data from the RGB image is a sum of the individual red (R), green (G) and blue (B) channels to give a total intensity value for those areas. The exposure time the images evaluated in Fig. 3-15 were captured at was 250 ms, with the µLED drive current set at 120 mA.

The trend in Fig. 3-15 shows that the mean pixel intensity increases with increasing concentration of the SA-QDs. This trend is seen both for the combined RGB data and the individual R channel data. The sensor response is approximately linear between 8 nM and 80 nM but begins to saturate at higher concentrations. This indicates that, at this exposure time, the detector of the smartphone has reached its limit. The lowest SA-QD concentration that yields a signal above the noise floor detection limit is 8 nM. We have used the mean pixel data from the red channel to determine a LoD for this current set up and smartphone. The LoD is defined here as the concentration giving an intensity reading, 3 times the standard deviations [89] above the intensity of a functionalised glass slide with no SA-QDs present. Below this concentration (8 nM), the sample regions were not bright enough to be detected by the smartphone sensor and were below the noise floor. A possible explanation is that the expected response of the sensor is sigmoidal due to Langmuir adsorption - that is often seen in antigen/antibody binding sensing [25], hence the intensity values drop more rapidly at low concentrations and the experimental conditions do not permit a high enough resolution in the concentrations below such levels. Another possible explanation for a steep reduction in detection is there may not be enough biotin present on the glass surface for SA-QDs to bind in sufficient numbers to be detected by the camera sensor. The binding efficiency of the SA-QDs to the biotin could also be affected due to the SA-QDs having 4 binding locations. This could result in one SA-QD particle binding to several neighbouring biotin molecules artificially reducing the possible LoD. As can be seen in Fig. 3-15 the data point (30 nM) for the red signal intensity is lower than expected, out with the linear trend. This is an outlier attributed to challenges fabricating the glass waveguides such as creating evenly distributed biological layers or keeping the glass surface free of excess residue. Unlike the R channel, the RGB intensity response is non-zero at a zero concentration of SA-QDs. This is because intensity is detected from the scattered light from the µLED in the G and B channel; whilst the blue light has been filtered out, the luminescence of the µLED has a non-negligible tail at green wavelengths. However, the value at 0 and overall trend of the R channel indicate that the red intensities captured by the smartphone are occurring

solely from the emission of the quantum dots and are not influenced by the G or B channel; the sensor therefore fully discriminates the fluorescence from the µLED light. Detection of concentrations as low as 80 pM have been reported in previous research where alkyl ligand quantum dots were used [73]. However, this was for a different kind of QDs that have a higher quantum yield, in comparison to the water soluble SA-QDs that were used in this research and that are necessary for biological applications [90]. As the previous research did not encompass bio-detection requiring rinsing procedures, all the quantum dots drop cast onto the membrane will have stayed in situ, leading to a lower LoD.

3.3.2 Effect on different driving current on detection

A comparison of the mean pixel intensities detected for different levels of excitation light power (i.e. with different driving currents for the LED device) is shown in Fig. 3-16. All smartphone images were taken at an exposure time of 250 ms, with the driving current being set 80 mA to give 7.5 mW of optical power (Fig. 3-16 a) and 120 mA to give 10 mW of optical power (Fig. 3-16 b). Both graphs indicate that above 8 nM the SA-QD intensity for the R channel increases with concentration regardless of the driving current. For each channel (R, G and B) a higher mean pixel intensity count is seen, along with a reduction in standard deviations when using a higher driving current of 120 mA. Although the intensity values detected by the smartphone sensor have increased for each channel, the LoD remains unchanged at 8 nM whether the current is driven at 80 mA or 120 mA. Increasing further the optical power could potentially lead to a lower the LoD (i.e., < 8 nM), however, as thermal effects and long-term stability of the µLED may raise challenges, this was not investigated in this work.

As stated previously, the R channel detects the SA-QDs independently with no influence from the pump light being detected, even with an increase in the amount of overall light the smartphone sensor detects. The behaviours are similar at the two drive currents for both G and B channels. The G channel intensities decrease slightly with increasing SA-QD concentration as there is higher absorption from the SA-QDs

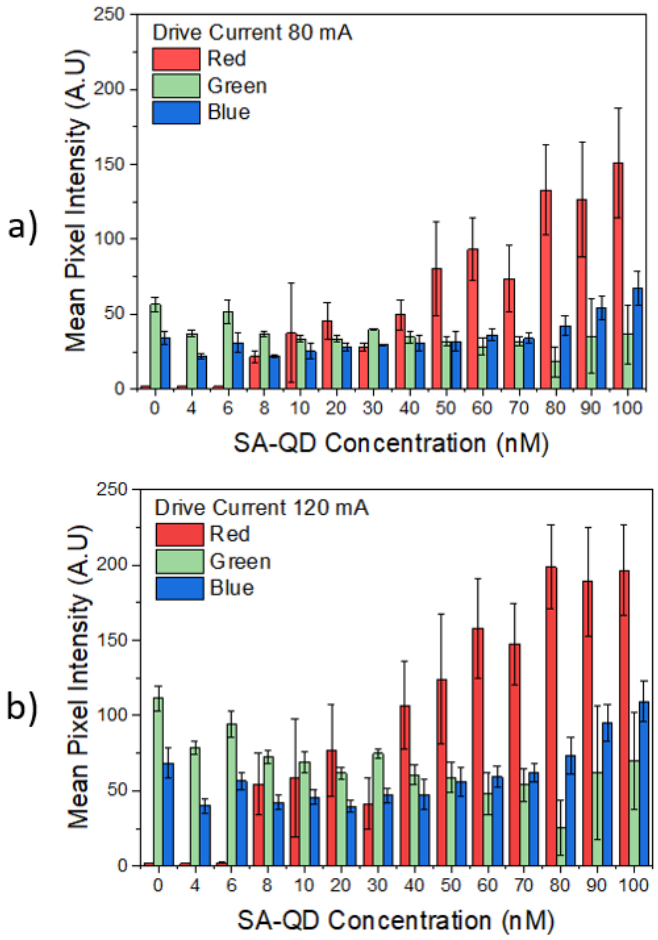

Fig. 3-16 Graph demonstrating the effect of increasing the current on the mean pixel intensities detected with the smartphone and the resultant effect on LoD a) shows the mean pixel intensities at a drive current of 80 mA b) mean pixel intensities at drive current of 120 mA

and the G channel is only showing a response to light emitted from the µLED. The B channel response shows a slight increase in intensity at higher SA-QD concentration, possibly because the B channel has a non-negligible response to red photon and/or because of an increase in scattered LED light. However, the magnitude of these trends is significantly lower than the changes seen in the R channel response.

3.3.3 Effect of exposure time on limit of detection

Three different exposure times (50 ms, 250 ms and 1000 ms) were compared to determine the change in mean pixel intensities on the R, G and B channels. By increasing the amount of light gathered by the camera sensor through increasing the

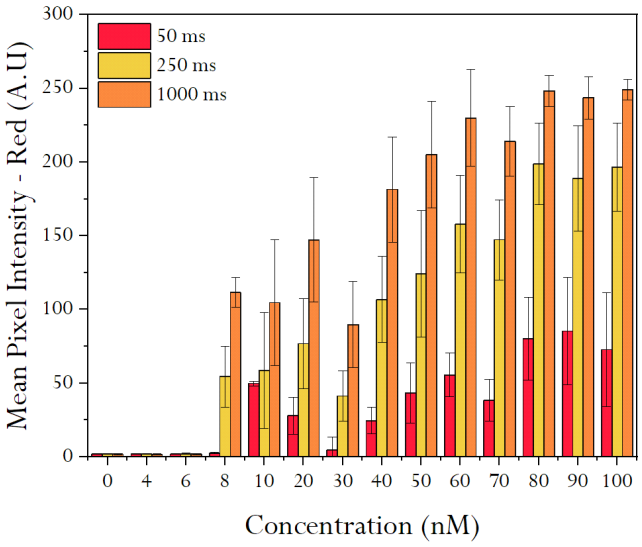

Fig. 3-17 Graph demonstrating the effect of increasing the exposure time on the mean pixel intensity of SA-QD regions. Three exposure times are shown, 50 ms, 250 ms and 1000 ms

exposure time, the expected effect of increasing this parameter would be to increase the pixel intensity counts and improve the LoD for lower concentrations of SA-QDs. The results of changing the exposure time are shown in Fig. 3-17. At 50 ms the LoD is 10 nM, upon increasing the exposure time to 1000 ms the LoD is improved to 8 nM. When isolating the R channel response, there is an increase in mean pixel intensity from 50 ms to 1000 ms for SA-QD regions at 8 nM. This increase is 46 times higher at a longer exposure time. Although there is an improvement in the LoD an increase to the noise floor also occurs and the detector is saturated more readily for higher concentrations of SA-QDs at the longer exposure time. The noise floor at 50 ms is 2 counts in comparison to 80.9 counts at 1000 ms. Below 8 nM, the smartphone sensor is unable to detect a significant intensity count of red photons, highlighting that for this application the limitations of detection for this smartphone and experimental set-up have been reached.

While increasing the exposure time can increase detection of lower SA-QD concentrations, conversely, decreasing the exposure time to 50 ms will allow for a larger range of concentrations to be detected. At a 100 nM concentration, 50 ms exposure time, the mean pixel intensity was found to be 72 counts; this is less than half the maximum intensity value that can be detected with the smartphone sensor.

3.4 Discussion

The research in this chapter has helped to establish that it is possible to discriminate and detect fluorescent tags using a novel µLED based platform and a smartphone as the detection system. Whilst it is a positive result that fluorescent tags could be detected using this platform, we have demonstrated that it has also been possible to establish a LoD, although there are still areas that could be improved upon. The platform has the advantage of not requiring intermediate optics to enable efficient light coupling, this should make working towards miniaturisation more feasible. As it currently stands the experimental set-up is a bench top system due to the power supply, however as the excitation source is a µLED without additional optics, transitioning from a bench top power supply to a battery powered device should be relatively straightforward due to the concept and design. Whilst considering miniaturisation and device design, some steps should be taken to consider a 3D printed holder for ease of alignment for waveguide to µLED and a holder for the smartphone. This will help to minimize repeatability errors due to alignment. It was noted previously that this research has been conducted with one type of smartphone, further work is required to determine the variances in LoD for other smartphones when using this set-up and whether the best option would be to use the operators own smartphone slotted into the holder or if the device unit would come with an integrated smartphone or other standalone image sensor reducing the requirement for calibration. When considering an all-encompassing device, it would be beneficial to have a software application designed specifically for imaging and then processing the images taken with the device, making it a one and done diagnostic solution, further minimising the need for additional expertise or time to wait for results.

While this research used JPEG images files, steps should be taken to use raw data image files instead as JPEG files have already undergone automatic post processing including white balance, colour interpolation, colour correction and compression to improve detection accuracy.

To improve the capability of the device, exchanging the excitation source from a blue emitting µLED to UV µLED would allow for a wider range of CQD wavelengths to be used. The UV excitation would allow for lower emission wavelengths of CQDs to be used and this would provide a means to multiplex the waveguide sensors with more than one wavelength of fluorescent tag on a chip at one time. Multiplexing allows for differential diagnosis between antigens of interest and would be better suited to use with a UV LED.

Streptavidin-functionalized QDs were utilized as the fluorescent emitters in this demonstration where the core shell material contains toxic and non-environmentally friendly chemicals such as cadmium. An alternative material that could be employed to avoid these toxic elements could be carbon quantum dots or indium phosphide. This would help to increase biocompatibility and would be better suited if the device was used in environmental settings such as water quality testing. However, as these alternative materials still lag behind the Cd-based materials in terms of photoluminescent properties, it may be a while before the emission properties of Cd-based quantum dots are matched.

3.5 Summary

In this chapter we have demonstrated a proof-of-concept µLED-based evanescent waveguide platform that can be used as a relatively simple fluorescent biosensor with smartphone detection. µLEDs enable efficient light coupling without any additional optics and scaling down the thickness of the waveguide platform, while maintaining efficiency, is possible. These factors contribute positively towards development of a compact POC device that has the potential to be battery operated. Importantly, the RGB response of the detector sensor can discriminate between fluorescence and excitation light by appropriate choice of the µLED and QD emission wavelengths, meaning that simple JPEG images can be taken for readings. A detection limit of 8 nM at an exposure of 250 ms has been established. By demonstrating that functionalized amine ligand QDs can be detected using a smartphone it provides a promising basis for the platform to be used as a compact biosensor for POC.

Chapter 4

4 Multiplexing and other fluorescent tags

In this chapter improvements on the proof-of-concept biosensor platform established in chapter 3 are explored. We look to assess if is it possible for a smartphone to effectively distinguish between different colours of fluorescent tags in situ at the same time. This could be used to determine if spectral multiplexing with different analytes is possible with this platform. The use of a novel fluorescent tag is also investigated; a so-called supraparticle, which is a spherical micro-assembly of quantum dots, functionalised with biotin.

4.1 Introduction

4.1.1 Multiplexing

When considering diagnostics for detection of pathogens and analytes, there has been an increasing focus on the detection of multiple markers in one device. This helps to minimise inconvenience to an individual undergoing testing and helps to maximise the resources needed for investigation. One way this can be done is by employing multiplexing. Multiplexing allows for investigation of several analytes or

biomarkers in one test rather than requiring several individual tests. Individual tests per analyte or marker would require consumption of more resources such as blood samples and time. Often more than one biomarker is required for accurate diagnosis for complex diseases such as cancer, diabetes, rheumatoid arthritis and osteoarthritis [91], where one standalone marker would not prove useful in making an accurate or early diagnosis. It is important for clinicians to be able to distinguish between diseases and this is often done through signs and symptoms of diseases. This process is known as differential diagnosis. Differential diagnosis of disease markers is important and provides useful information to clinicians when looking for treatments' options. Multiplexing would provide an efficient way to aid this differential diagnosis process. Another driver for developing multiplexed diagnostics is that there is a cost benefit to not needing several tests to detect multiple biomarkers. Many laboratory tests require a specialised technician to perform them, so multiplexing can help to reduce time costs. As more data could be gathered from one sample, testing could become more efficient and quicker, leading to better diagnosis and treatment options if required.

Although multiplexing could become the preferred method for testing in time, it still presents some challenges such as cross-reactivity between analytes, that can muddy results. Additionally testing for multiple biomarkers could result in an increase in overdiagnosis of certain conditions. Detection of biomarkers where there is an absence of symptoms could result in unnecessary treatment or cause unwarranted anxiety of a condition that would otherwise have not caused harm to the patient. Ensuring that the correct antigen or analytes are targeted and detected is critical for accurate diagnoses and treatment. Perhaps due to this difficulty there are many different strategies that researchers have employed to investigate the best methods for multiplexing. Section 4.2 outlines some of the different techniques that could be employed to create a multiplexed immunosensor, each with their own advantages and drawbacks.

4.2 Strategies for multiplexing

4.2.1 Spatial multiplexing

Spatial multiplexing is a way to measure multiple analytes in one device by using repeated arrays of sensors that are individually configured to detect a specific biomarker. Spatial multiplexing is often used with electrical or optical signals to categorise the different antibodies being detected. As each sensor is programmed to a specific biomarker in an array, elimination of crosstalk is possible without the need for elaborate and complex sensor designs. Adding new biomarkers of interest to an array is also simple since each sensor is programmed for a specific biomarker signal allowing for continual device upgrades with minimal reconfiguration required. However, one drawback to this method is that larger numbers of sensors can lead to increased time acquiring and processing data, with the additional challenge of integrating several sensors into one system. The smartphone platform used in this chapter would be suited to spatial multiplexing as it is used as multiple biomarkers could be added to one slide and based on the position of the detected signal from the images, the target analyte could be determined.

4.2.2 Barcoded multiplexing

Barcode multiplexing is a sister technique to spatial multiplexing. It makes use of combining several labelling molecules on a single sensor to create a signature, or “barcode” to enable multiplexing. This labelling can be done using ligands that have different electroactive properties [92], i.e. different properties in response to an electrical signal or ligands containing a photoactive component, which will respond to an optical signal. Unique label combinations can be designed and attached to targets of interest so that there is no overlap or cross reactivity that could be misunderstood. When the targets bind to the probes, they emit a signal that is easily distinguishable from other targets in the same scan or sample.

4.2.3 Particle based multiplexing.

Using small scale particles such as micro or nano sized particles such as CQDs, that have been functionalised with an antibody that corresponds to the analyte of interest are being used increasingly for immunosensors. These particles will aggregate at the target biomarker, that allows for detection even at low concentrations. Using multiple different antibodies attached to the microparticles allows for multiplexing [93], [94]. This technique could be used alongside wavelength multiplexing with CQDs to allow for more distinction between different analytes.

In the following sections we describe how the biosensing platform has been used to explore multiplexing on our simple glass waveguide with multiple wavelengths of QDs used as the fluorescent tag to demonstrate multiplexing.

4.3 Quantum Dots as a fluorescent tag in multiplexed immunosensors

Quantum dots (QDs) are excellent fluorescent labels for use in multiplexing due to their excellent optical properties, such as high brightness, broad absorption spectrum, high quantum yield, resistance to photobleaching and a narrow photoluminescent spectrum [95], [96]. Having a broad absorption spectrum means that one excitation source can be used to excite several different wavelengths of QD tag at the one time, which is ideal for multiplexing. Their narrow band emission also means that when several different wavelengths of tags are used that there is little overlap in their emission spectrum, reducing the incidence of crosstalk between detection wavelengths.

4.4 Experimental methods to enable multiplexing

4.4.1 Microscope slide functionalisation

The process used to functionalise the glass microscope slides to act as sensor chips follows the same procedure and to demonstrate multiplexing using multiple

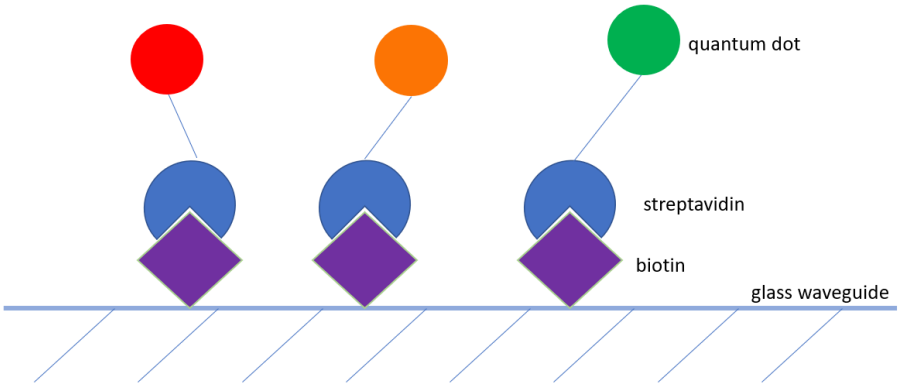

Fig. 4-1 basic schematic of how the 3 different wavelengths of SA-QD tags would bind to biotin on the waveguide surface.

wavelengths of Invitrogen SA-QDs the protocol for rinsing following drop casting was kept consistent outlined in the previous chapter, section 3.2.6.1.

Fig. 4-1 shows a basic schematic of how the multiple wavelengths of SA-QDs were placed on the glass surface to be used for multiplexing.

4.4.2 Multi-Wavelength streptavidin quantum dot tags

SA-QDs were purchased from Invitrogen, the 655 nm wavelength were the same that were used in Chapter 3. Two other wavelengths of the Invitrogen SA-QDs were purchased so multiplexing could be demonstrated, these were 585 nm and 525 nm. These three wavelengths were chosen as they would be spectrally separated from each other to give the smartphone camera the best opportunity for discrimination without cross talk. The quantum dot material in these tags is CdSe core with a ZnS shell that is then coated in polymer to allow conjugation of the streptavidin molecules to the tag. The SA-QDs are approximately 15-20 nm in size. The absorbance and PL spectra for each wavelength is shown in Fig. 4-2. The PL spectra and absorbance were measured in solution. Each wavelength of SA-QDs were diluted from their stock solution using PBS to a concentration of 1nM. For the 525 nm SA-QDs a 450 nm LED was used to excite the QDs, whereas a 532 nm laser diode was used for the 585 nm and 655 nm SA-QDs. 450 nm was used to excite the lower emission wavelength SA-QDs as there would be spectral overlap between the 532 nm laser diode and the 525 nm SA-QDs. The solutions were placed in a cuvette holder and the PL spectra was

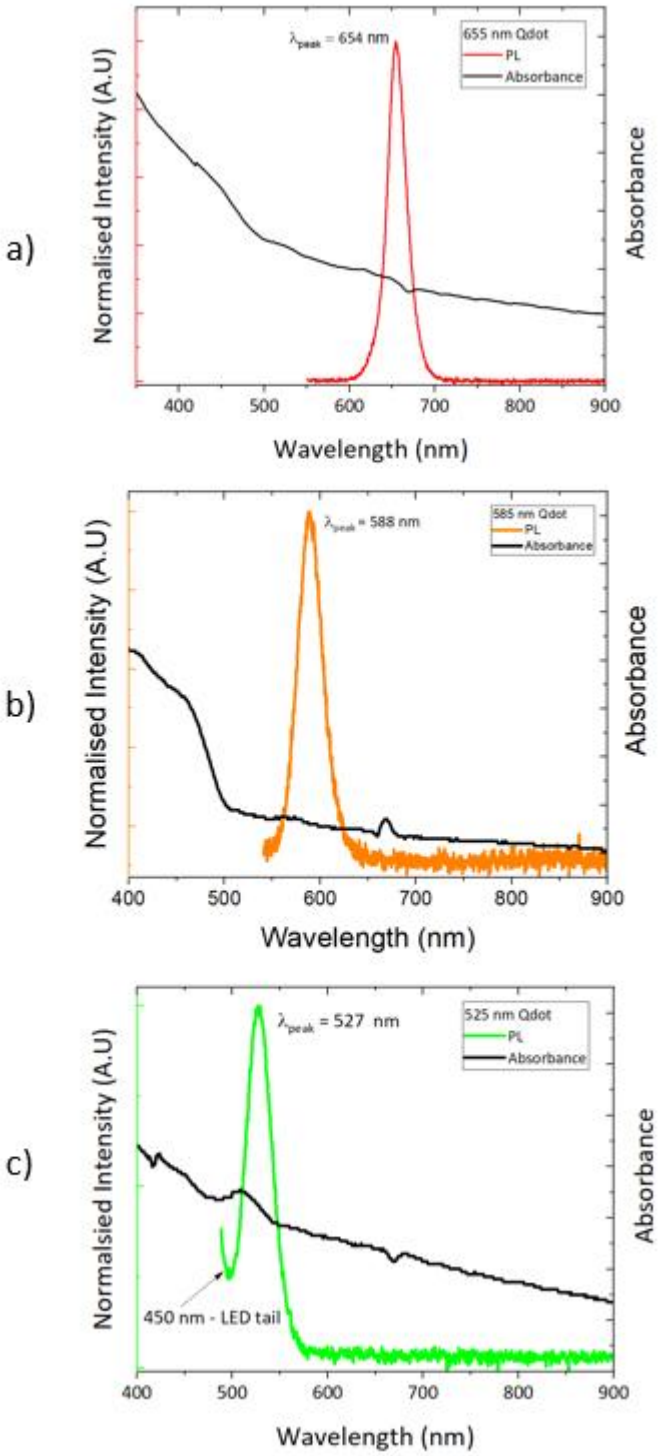

Fig. 4-2 Absorbance and photoluminescent spectrum of each wavelength of Invitrogen Qdot, from a): 525 nm, b) 585 nm, c) 655 nm.

collected using an Ocean Optics spectrometer. The absorbance was collected using a UV-vis spectrophotometer.

Fig. 4-3 Image taken using the Samsung Galaxy S9, showing placement the different wavelengths of SA-QDs that were drop cast onto the glass slide

0.5µL of the three different wavelengths of SA-QDs, were drop cast onto the functionalised glass surface. 100 nM of each wavelength of the SA-QDs were mixed with 4% BSA to inhibit non-specific binding. The placement of the SA-QDs is shown in Fig. 4-3. In the image, the 655 and 585 Qdots are seen more easily than the 525 Qdots, this is discussed later in the results.

4.4.3 Characterisation and Image Processing of the Sensor

The experimental set-up used to image the waveguides in chapter 3, section 3.2.12 is used again here to characterise the multiplexed glass slides. The glass slides and end coupled to the 450 nm µLED, while being imaged with a smartphone. The same procedure for analysing the JPEG images to obtain the mean pixel intensities was followed as outlined in section 3.2.12.1.

4.5 Multiplexing Results

Images of the glass slides were taken, and the resulting JPEGs were analysed. Fig. 4-4 plots the results of the individual R, G and B channels of the smartphone sensor. Each CQD wavelength was dropcast 3 times, giving 3 areas of pixel regions to be analysed per wavelength. Each wavelength is highlighted in the plot. The x-axis simply plots the location of the SA-QD pixel regions numerically, while the y-axis is the mean pixel

intensity of the SA-QD regions. This results in a spectral colour profile for each wavelength, where the R, G, B channels will give a different intensity ratio for each wavelength of SA-QD.

The profile for the first 3 regions is for the 655 Qdot, this profile is already seen in section 3.3.1 for the limit of detection results for the biosensor. It shows there is a higher ratio of red and blue light intensities, with lower levels of green. Although this profile is seen previously in Fig. 3-15, there are higher intensity values for the SA-QDs likely due to some saturation of the camera sensor from using SA-QD concentrations on the upper end of the camera capability (100 nM). The 585 Qdots show a higher ratio of red and green intensities with lower blue intensity level. The 525 Qdots show low intensity levels at each of the smartphone sensor channels (matching what is already seen visually with the naked eye and in the image in Fig. 4-3), this will be due to lower emission intensities from the 525 Qdots overall. Lower excitation emission of the 525 nm SA-QDS could be due to a lower absorption of the pump light. If an excitation source that was better suited to the absorption of the 525 Qdots was used, the expected intensity profile mix would be higher intensities of the green and blue channels with low red intensities. This suggests that for better emission of multiple wavelengths on one slide, a UV excitation source would be better suited for multiplexing in this experimental setup as the 525 Qdots would be able to absorb

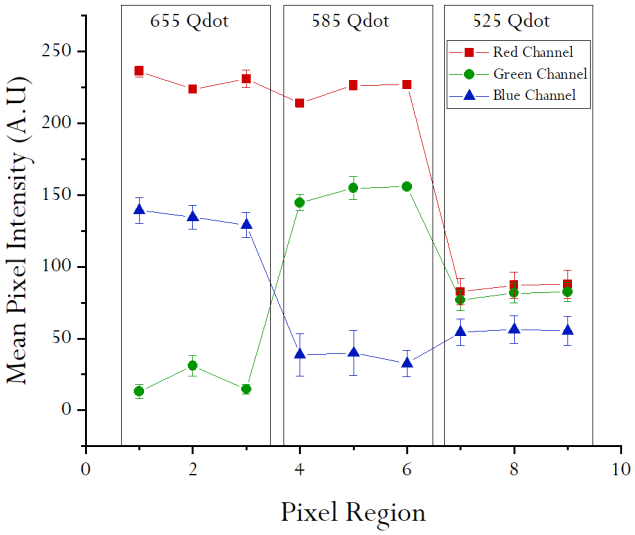

Fig. 4-4 Plot of spectrally separated R, G B channels from the smartphone showing a "colour profile" for the 3 different wavelengths of quantum dots imaged from the one glass slide

more of the emission from the pump and fluoresce more. Although it was not possible to obtain an intensity profile for the 525 Qdots in this instance, there is promise for this experimental setup to be used as a multiplexed POC device. An intensity profile for the 585 nm and 655 nm could be demonstrated, however the higher pixel intensities for these wavelengths for the red channel indicate that some saturation and crosstalk is seen by the smartphone sensor for these two wavelengths. Although it is possible to distinguish between two wavelengths when seen in situ, on one glass microscope slide, more adequately chosen QDs would give a better spectral response from the smartphone camera couple with a UV excitation source this biosensor could yield even better results to demonstrate more effective multiplexing.

The remaining sections of this chapter explore how the use of a novel fluorescent tag -supraparticles - could be used with the biosensor platform.

4.6 Self-Assembled Supraparticles (SPs)

Within the research group, applications of self-assembled SPs are being investigated. Here the SPs are composed of smaller individual nanoparticles in this instance, quantum dots. Larger structures of self-assembled QDs are formed through Van der Waals forces. A basic representation of this is shown in Fig. 4-5. The shape, order and density of the nanocrystals will determine the final structure of the SPs [97].

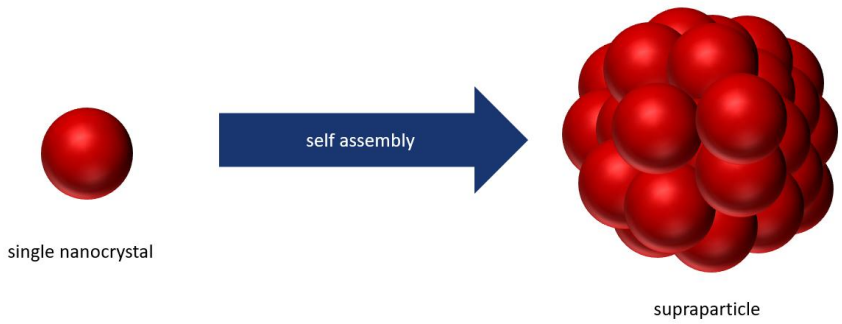

Fig. 4-5 representation of a single nanocrystal (QD) and the SP structure formed following self-assembly.

4.6.1 Self-Assembly Techniques of SPs

CQDs are a versatile material that can be used to assemble different structures from solutions. Self-assembly refers to the ability for a material to closely pack together and form a structural shape through an external driving force such as electrostatic interactions, charge compensation effect, hydrogen bonding interactions, hydrophobic/hydrophilic effect or capillary action [97], [98]. This method is generally less expensive and simpler for fabricating different structures of materials than top-down nanofabrication methods such as epitaxy.

One technique is to use emulsions for wet self-assembly. An emulsion is a mixture of two liquids, that do not readily mix resulting in one of the liquids forming droplets within the other following mechanical agitation. Surfactants are usually used in this method to stabilise these droplets and to reduce the surface tension between the two mixed liquids. There are generally four types of emulsion: oil in water, water in oil, water in oil in water and oil in water in oil [99]. Using an emulsion provides a simple way to self-assemble CQDs with good stability, size tunability and excellent optical properties. For a typical oil in water emulsion synthesis the oil phase would contain the CQD solution that is then added to the water phase containing the surfactants used to stabilise the particles. Aggregation of the CQDs into a structure happens as the solvent evaporates or through demulsification. The process of emulsion based self-assembly has been schematized in Fig. 4-6.

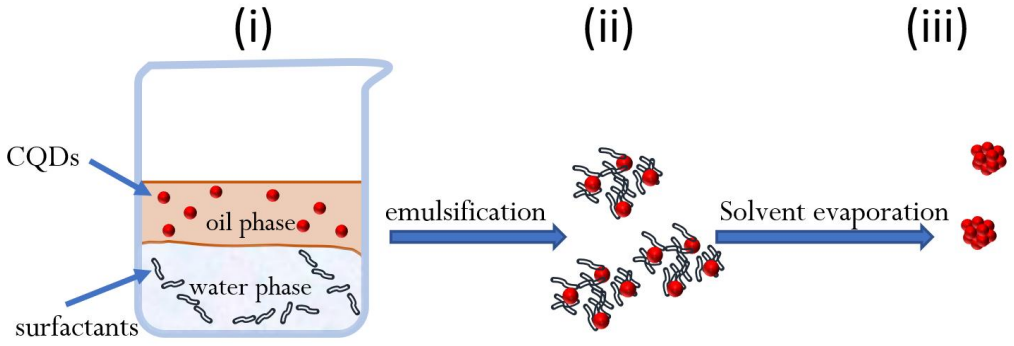

Fig. 4-6 schematic of oil-in-water emulsification process for SP synthesis. CQD solution and surfactants are mixed to enable emulsification. Once emulsified the excess solvent is evaporated leading to the self-assembly of SP structures.

Within emulsion based self-assembly, there are three different stabilizing methods that are commonly used, surfactant stabilized emulsions, Pickering emulsions and surfactant free transient emulsions. The surfactant stabilized emulsion mechanism has already been described above. A Pickering emulsion doesn't use surfactants to help the formation of SPs but relies on solid particles such as CQDs, silica nanoparticles or titanium oxide to stabilize the SPs at a liquid-to-liquid interface [100].

Surfactant free transient emulsions are essentially an emulsion without the stabilizing materials added to help reduce the cost of adding more materials and steps to the fabrication process. Simply put, this method involves a two liquid interface and where the nanoparticles meet at the interface and partial diffusion between the two liquids cause the SPs structures to form at the boundary. The key from this method, first used by Liu et al [101] is to have the correct solubility between the two liquids used, as this partial diffusion would not occur with all liquids employed for emulsion self-assembly. It is important to note other factors which would affect the emulsion solution such as temperature, pH and mixing speed would have an influence on the stability of the SPs using this method.

4.6.2 Why SPs?

SPs have the advantage of sharing the material properties of their smaller building blocks, whilst also having additional properties of their combined suprastructure. For example, the SPs used in this chapter have inherited the optical properties of the CQDs to give the SPs bright emission, colour tunability and high quantum yield. When CQDs agglomerate into a cluster, coupling, emergence and colocalization [97] are some of the properties that the SPs gain from forming into a SP Coupling refers to the interaction between individual CQD particles that are closely situated, leading to strong electron interactions within the nanoparticles where new properties of the SP to occur. Emergence describes the phenomenon where the larger SP possesses unique characteristics not present in the individual CQD particles. Colocalization signifies that the nanoparticles are interconnected, creating an object with novel

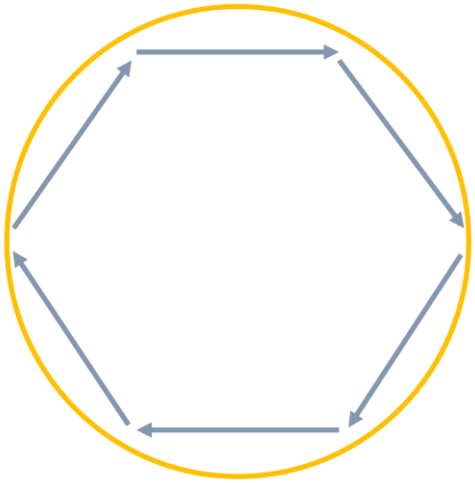

Fig. 4-7 representation of a whispering gallery mode, the yellow circle represents the diameter of the SP, while the arrows demonstrate the path of the light that resonates within the SP creating a feedback loop through TIR conditions enabling WGMs to oscillate.

properties based on the building blocks of the nanoparticles. Nanoparticles can enhance their optical properties through coupling the electronic wave functions, but for simplicity we don't consider coupling or interaction between our CQDs.

In larger SPs, the material can function as an optical cavity and sustain resonances by exploiting whispering gallery modes (WGM). This phenomenon manifests when the particles are stimulated, causing light to constructively interfere within the cavity, amplifying the emitted light. As a result, larger particles that serve as WGM cavities can produce narrower emission spectra [102]. A SP can serve as a resonator by confining oscillatory light rays inside its material cavity through total internal reflection (TIR). When the size of the SP is on the same scale as the wavelength of light, specifically when the SPs circumference is at least equal to one wavelength, it can act as a whispering gallery mode (WGM). Constructive interference of light within the cavity creates a feedback loop, generating distinct and sharp resonances. These WGM materials are responsive to the size and shape of the resonator, as well as the difference in refractive index between the SP material and its surroundings. The wavelength of light is inversely related to the refractive index, which means that a denser material with a higher refractive index can serve as a resonator at smaller sizes

compared to a medium sized particle with a lower refractive index. Furthermore, the refractive index contrast can enhance the strength of these resonances.

Even without considering the cavity effects, the ability of SPs to absorb more of the excitation light and generate greater fluorescent emissions, presents a significant advantage when these structures are employed as fluorescent labels. This advantage has the potential to lower the detection limits for analytes, facilitating more sensitive detection methods with these brighter tags. The SPs used in the following sections of this chapter were synthesis using an emulsion technique and formed spherical microspheres.

4.6.3 Applications of SPs

Since SPs can be fabricated through a variety of different methods, from a variety of starting materials one of their main advantages is that they can form many different shapes of SPs. Tuning of the material, through its composition, size and shape allows these SPs to be designed for a variety of different applications although the starting materials may be similar. Applications where SP have been used previously include: optical pigments, lasers, sensors, drug delivery, as an anti-counterfeiting agent and as photocatalyst [103].

4.7 Experimental Methods

4.7.1 SP Synthesis

The following sections outline how the SPs were fabricated and the sensing experimental work was carried out. The SPs used in this chapter were synthesised and characterised by Dr Charlotte Eling (University of Strathclyde, Glasgow). I gained familiarity with the synthesis technique as I led the experimental sensing work.

The procedure that is outlined is based on the oil-in-water emulsion approach described in section 4.6.1. The SPs were synthesised from a CQD solution. The CQDs had an alloyed core of CdS_xSe_{1-x} and a ZnS core with oleic acid ligands and an emission wavelength of 575 nm. The PL spectrum is shown in Fig. 4-8. The average particle size was 6 nm. The CQD solution was added to 100 µL of chloroform to a concentration of 20 mg/ml. Next, a 1.25% v/v solution of polyvinyl alcohol (PVA) in milliQ water was mixed with the QD solution and vortexed for 5 minutes. This solution was then left at room temperature for 2 hours to allow the chloroform to evaporate. The mixture was then centrifuged at 10,000 rpm for 10 minutes, the supernatant was then removed and re-suspended in milliQ water.

Following successful SP formation, the next step was to perform a ligand exchange as the SP's are hydrophobic due to the oleic acid ligands, followed by coating the SPs in a silica shell to enable functionalization with biotin and render the SPs water soluble and thus better suited for biological applications. The steps for ligand exchange are as follows: the SPs were re-dispersed in ethanol, and a solution of polyvinyl pyrrolidone (PVP) in water was made, at concentration of 50 mg/ml. 80 µL of SP solution and 66 µL of PVP were then added to a microcentrifuge tube and sonicated for 20 minutes. This process was then repeated twice to ensure there was a large enough volume of the solution. The mixture was then centrifuged again at 10,000 rpm for 10 minutes to obtain a pellet of SP material that was then re-dispersed in

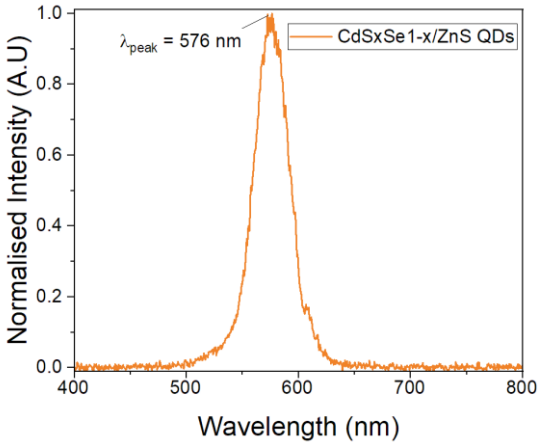

Fig. 4-8 PL spectra of the CdS_xSe_{1-x}/ZnS QDs with a peak emission wavelength of 576 nm.

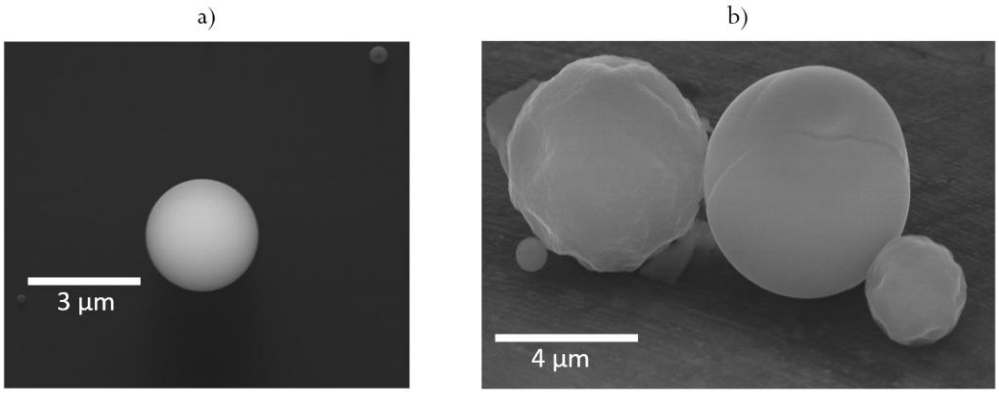

Fig. 4-9 a) SEM image of an uncoated Cd/Se SP b) SEM image of a silica coated SP.

ethanol. Centrifuging was performed another two times to ensure the excess PVP was removed.

To form the silica shell, a solution of tetraethyl orthosilicate (TEOS) in ethanol was made to a concentration of 635 mM. 20 µL of TEOS was added to the SPs and sonicated for 5 minutes. Next, 800 µL of milliQ water and 800 µL of ammonia were added to the SP mixtures and sonicated for an hour. The silica coated SP solution was then centrifuged at 10,000 rpm for 10 minutes and the pellet was re-dispersed in water. The centrifugation step was performed 3 times in total to allow for purification. Fig. 4-9 shows scanning electron microscope (SEM) images of the SP's. Image a) and b) are a comparison of the structures between the uncoated CdSSe/ZnS SPs and the result of silica coating.

Once the silica shell has coated the SPs, the process of functionalising with biotin can begin. The silica coated SPs are centrifuged at 10,000 rpm for 10 minutes to form a pellet that can be re-dispersed in 2 ml of ethanol and 50 µL of (3-Aminopropyl) triethoxysilane (APTES). This is then left to stir overnight at room temperature. Once well mixed, the solution is centrifuged at 10,000 rpm for 10 minutes and the pellet is re-suspended in water. This process is repeated a further two times for purification purposes.

Now the silica bonds have been silanised using the APTES, the SPs can be functionalized using a NHS-Ester polyethylene glycol(PEG) biotin. The latter here

contains an additional unit to the NHS-Ester, a photocleavable ligand - ortho-nitrobenzyl (ONB) linker – for an additional functionality; however, the functionalisation procedure can be generalised to many types of molecules. The NHS-biotin is dissolved in water to give a 4.16 mM solution, this is then pH adjusted to a more alkaline level of 8.5, using sodium hydroxide (NaOH) and hydrogen chloride (HCl) as the reaction between NHS esters and amines is pH dependent, at lower pH's no reaction between these molecules will occur. The SPs are centrifuged to remove the water, and then re-dispersed in the NHS biotin solution and was stirred at room temperature for 4 hours. To remove the ligands that remain unbound from the solution, it was centrifuged a final 3 times at 10,000 rpm for 10 mins each. The SPs are now ready to be used as functionalised fluorescent tags.

4.7.2 Functionalisation the glass slides for the SP tags

The same protocol for functionalising the glass microscope slides was followed as outlined in section 3.2.6. The glass slides were plasma treated, followed by silanisation using APTES and functionalising with NHS-biotin. The slides were also coated with BSA to reduce the incidence of non-specific binding of the tags to area of the glass that had not been functionalised. One difference that was required for the glass slides fabricated for use with the SPs, was an additional step of adding neutravidin to the surface following prior functionalisation with the NHS-biotin ester, which would allow capture of the biotin conjugated SPs. The neutravidin was washed over the glass for 1 minute and the excess was rinsed off in subsequent solutions of 4% v/v polysorbate 20, PBS and DI water and dried. Control slides were also made following the same protocol but the steps for adding biotin and neutravidin were omitted.

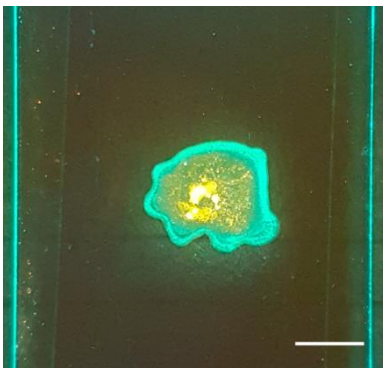

Fig. 4-10 Image taken using the Samsung Galaxy S9 showing the area of 575 nm SPs deposited on the glass surface, before rinsing procedure is carried out. Scale bar, 5mm The edges of the glass slide appear green due to a 500 nm cut off filter being used in conjunction with the µLED, cause the image to appear green due to the green tail of the µLED.

4.7.3 SP Microscope Slides

A volume of 2 µL of the biotin conjugated SPs was dropcast onto the glass slide. Fig. 4-10 show an image of the area where SPs were deposited onto the glass surface. A larger volume of SPs was deposited compared to the SA-QDs used to demonstrate multiplexing. This was due to the SPs' tendency to stick to the sidewall of the pipette tips, as we wanted to ensure that enough functionalised material would come into contact with the functionalised glass surface, allowing binding to occur.

4.7.4 Characterisation and Image Processing of the Sensor

The experimental set-up used to image the waveguides in chapter 3, section 3.2.12 and again briefly in section 4.4.3. Using a Samsung Galaxy S9 smartphone, images are taken of the surface of the functionalised glass slides to determine if binding of the biotin conjugated SPs has occurred, while being excited by a 450 nm µLED.

4.7.5 Testing the photocleavable ligands

The NHS-Ester contained an ONB photocleavable ligand which could be cleaved with 365 nm UV irradiation. These were chosen to determine if it was possible to remove the SPs and re-use them in the future for other experimental work. To test this, the SPs were dropcast onto the glass slides and allowed to dry. The glass slides were subsequently exposed to UV illumination for 5 minutes then were rinsed and dried

following established procedures. The regions containing SPs in the images were analysed as per the previous protocols.

4.7.6 SP results

For the analysis of the SPs' images, one larger area of drop cast material was evaluated rather than comparing multiple smaller regions as with the slide containing the commercial QDs. A larger area was dropcast to ensure adequate SP material could be deposited on the surface due to the propensity of the SPs to stick to the pipette side wall while dispensing. The intensities between a control glass slide and one that had been functionalised with neutravidin following drop casting with conjugated SPs were compared. The questions we aimed to answer with these experimental results were twofold: 1. Were the SPs able to be excited using the TIRF platform and detected by the smartphone camera; and 2. Did binding occur between the neutravidin and the biotin conjugated SPs. The results are as follows.

Fig. 4-11 a) shows the plots of the mean intensity values of the drop cast area for the combined RGB and separate R, G and B smartphone channels for the control slides and b) the neutravidin coated slides. The highest pixel intensity of the SP emission is measured before any washing steps have been carried out as would be expected since all the SP material would still be present regardless of if they had bound to any analytes. As the intensities for the RGB and individual channels are above a background noise level established in chapter 3, we have established that the SP

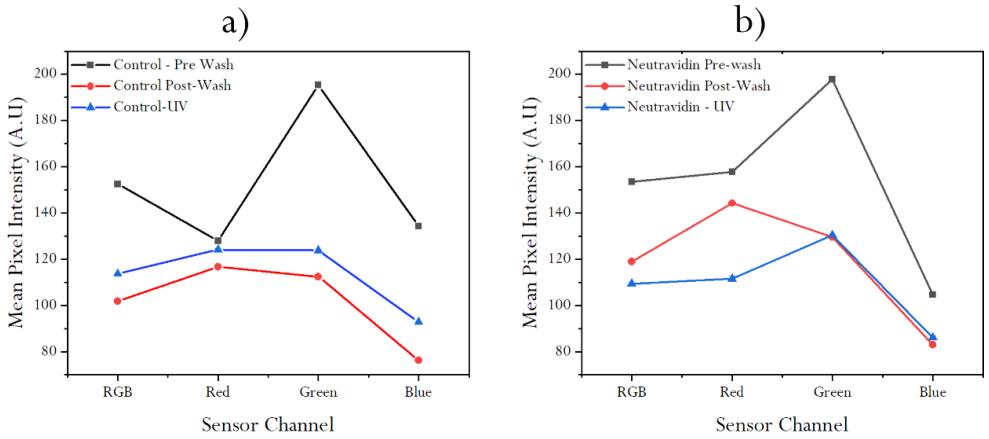

Fig. 4-11 a) results of the control slide without neutravidin conjugated to the SP b) results when neutravidin is used as binding tag to SP to demonstrate.

emission can be detected using the smartphone camera, meaning that this could be a suitable fluorescent tag for this proof of concept (POC) device. The SPs can also be clearly seen in the images taken as seen in Fig. 4-10 from the orange/yellow luminescence seen. For determining positive binding between the neutravidin on the glass slide and biotin conjugated spheres, the control and functionalised images were compared. Comparing Fig. 4-11 a) and b) intensity values show there is a 25% reduction in the overall pixel intensity values between the pre and post-wash steps, for the control and functionalised slides. This is to be expected as excess unbound SPs were washed away from the surface, reducing the detected intensity. After washing, you would expect a greater reduction in the intensity for the control slide as the SPs wouldn't have any analyte to bind to. A reduction in the intensity can be seen from the trends in a) and b), however it is not to a zero-value intensity for the control slides. This is thought to be due to non-specific binding (NSB) from excess ligands on the SP surface during fabrication. Although the intensity value for the control is not zero due to NSB, there is a significant intensity difference between the control and the neutravidin slides post wash of approx. 20 counts which is higher than the standard deviations. This suggests that there is a higher proportion of SPs that have bound to the slide containing neutravidin, indicating an initial positive result on binding. While there are some SPs still left on the control after binding, this could still be acceptable method used when looking to determine limits of detection, as a minimum intensity threshold would be established, and any intensity above that would be used to indicate analyte presence.

4.7.6.1 Photocleavable ligands

After successful binding of the SP tags, the next step was to test the efficacy of the photocleavable ligands. Fig. 4-12 plots the differences in the mean pixel intensities for a control slide and a biotin functionalised slide before and after UV irradiation at 365 nm for 5 minutes. When comparing the mean pixel intensity for the control slide before and after UV irradiation, there was a 36 % reduction in intensity values seen.

Similarly, for the biotin functionalised there was a 52% decrease in intensity levels seen when comparing pre and post UV values. Although the biotin functionalized slides displayed overall higher intensity levels due to a greater number of SPs remaining in place thanks to their strong binding to the surface, both the control and functionalized slides exhibited reduced intensities after UV irradiation. This reduction in intensity would be anticipated if the photocleaving process took place effectively indicating that the number of SPs bound to the surface has decreased. Therefore it has been taken as a positive indication that the photocleaving process occurred..

This successful photocleaving process opens up the potential for reusing and recycling the SP tags after prior use, which can lead to cost-saving and environmentally friendly applications.

4.8 Discussion

In this chapter we have explored ways to improve the features of the proof-of-concept device outlined in chapter 3. We have demonstrated the platform is capable of distinguishing multiple wavelengths on one glass slides using a smartphone, which

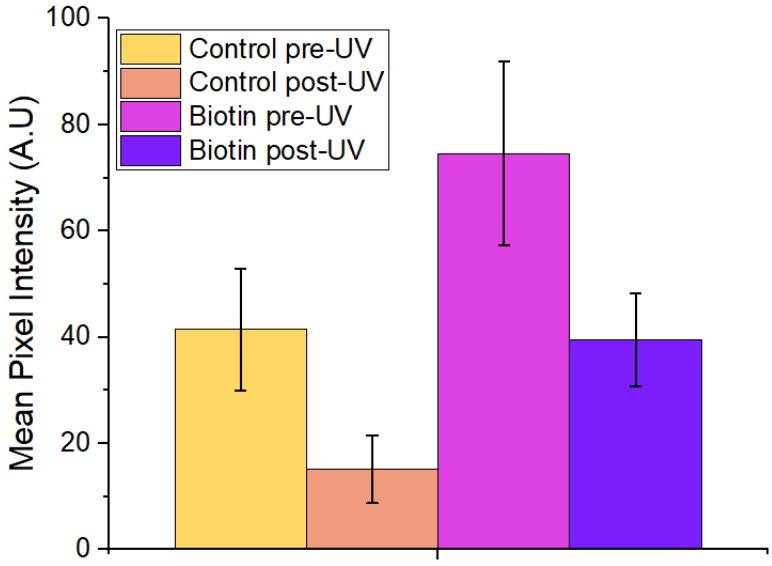

Fig. 4-12 Photocleavable ligand results. A comparison of mean pixel intensities of a glass microscope slide that has been functionalised with biotin and its control. For each slide there is a reduction in the mean pixel intensities after the QDs have been exposed to UV light that would indicate the photocleavable ligands have cleaved, resulting in the reduction of QDs following rinsing of the glass slides.

allows for real time multiplexing with this simple proposed low-cost device. Primary care users would benefit from this due to greater accuracy and the give them the ability to establish better care and treatment by differentially diagnosing analytes for better treatment to be realised. Although we have not managed to demonstrate true multiplexing with different analytes or biomarkers of interest to date with this device, it is the next logical step towards making this device a realised and demonstrable POC device. Crosstalk between the SA-QDs is still a concern between the 585 nm and 655 nm, as the R channel detects a high level of red intensity at for the 585 nm dots, but with more carefully chosen spectrally separated wavelengths this effect could be minimised further. Although we have a positive result in terms of distinguishing multiple wavelengths with the smartphone, further improvements can be made by acquiring and using a UV excitation source, so that a wider range of visible wavelengths QDs can be used for multiplexing purposes without crosstalk.

We have also demonstrated that it is possible to use conjugated SPs as an alternative fluorescent tag. These materials have in principle the potential to establish the presence of lower amounts of analytes due to their brighter emission properties, giving them the ability to be detected even when they have bound to a smaller number of analytes. This could help to improve the limit of detection of this POC device and make it suitable for use for a larger ranger of biomarkers that may only be present at small amounts. A limit of detection has still to be established with this material, as well as improvements in the protocol for use and removal of the photocleavable ligands. Decreasing the NSB due to the ligands would also help to improve the limit of detection when using these exciting new sensing materials to reduce the likelihood of false positive results. Future work using this platform should include establishing a limit of detection with the conjugated SP material, as well as a comparison between LoDs between the SA-QDs and SPs to determine if the SPs can in fact improve the amount of analyte required for accurate detection.

4.1 Summary

Two different methods have been presented in this chapter that could form the basis to extend the functionality of the biosensor that has been outlined in chapter 3. Both methods are in their infancy but provide a clear basis for improvement and have their own individual advantages – multiwavelength tags would provide a basis to detect multiple analytes on one slide, whereas using SPs as a new novel tag could provide improved limits of detection for analytes at lower concentrations due to their brighter emission properties.

Chapter 5

5 Thermal Stability of Colloidal Quantum Dots Encapsulated in Elastomeric Polymer

As mentioned in Chapter 2, CQDs are also utilized as colour-converters of LEDs and laser diodes in a multitude of applications, including solid-state lighting and visible light communications, wearable, and health technologies, or even, as discussed later in Chapter 6, quantum technologies. For applications such as integrating with LEDs, the stability of CQDs under relatively high temperature conditions is important. This chapter presents research focussing on the effect of temperature on the optical properties of colloidal quantum dots when incorporated in an elastomer. The effect of temperature is isolated, by heating composite samples in a vacuum oven to remove other factors that can also contribute to QD degradation and lead to poorer photoluminescent properties such as photo-oxidation. Here, we introduce the principles behind characterising colour converting composites using a µLED and look at the irradiance outcomes to determine if a maximum operating temperature can be established, to aid adoption of CQDs as fluorescent emitters into new devices.

Results from this chapter were published in 2019 IEEE 2nd British and Irish Conference on Optics and Photonics (BICOP)[104].

5.1 Introduction

When developing novel integrated devices such as wearable displays, lighting, and health technologies, it is important that the materials and photoluminescent (PL) properties are robust under different operating conditions. Flexible colour converting composites like the ones introduced in this chapter, play an important role in light emitting devices, which often have more difficult operating requirements. In this chapter, we explore the luminescent properties of light-emitting elastomeric materials made from polydimethylsiloxane (PDMS) and colloidal quantum dots (CQDs) under high temperature conditions, to simulate operating conditions of light emitting diodes (LEDs). CQDs are solution processable and can be manufactured on a larger scale which makes them an ideal candidate for device integration. As their surface is coated with ligands due to their wet chemistry synthesis, they are ideal materials to be incorporated within polymer matrices to create flexible composites. Materials such as PDMS and polyurethane can enable flexibility and even conformability to other structures and shapes, which in turn broadens the scope for colour converting composites, e.g. allowing their use in biomedical applications [105]–[107].

CQDs have become a popular material for use in colour converters for optoelectronic applications due to their highly tuneable emission wavelength, colour purity and high luminescent efficiency [18]. These characteristics make CQDs ideal for customization to meet the specific requirements of various applications. When combined with a polymer to create a colour converting composite they can used with efficient blue or UV emitting GaN-based light emitting diodes (LEDs) to obtain, narrow emission wavelengths in the visible. For example, combining red and green CQD colour converters can be used in conjunction with a blue LED to produce a white LED with a warmer colour rendering index (i.e. a better light quality) than would be obtained using only a yellow phosphor [18], [108] with the blue LED. Applications such as

displays [18], solid state lighting [20] and visible light communications [109] are where CQDs are commonly used due to their ease of integration.

Despite their many desirable characteristics CQDs are susceptible to degradation when exposed to heat, water and oxygen [110]. Combining the CQD nanocrystals with a polymer material to make a matrix offers a mechanism to provide a barrier to oxygen and/or water molecules. Although a polymer may provide a barrier to water and oxygen, thermal degradation to the luminescent material is still possible through direct effects on the CQDs or via thermal contact from the matrix material. In many applications CQD colour converting composites are placed in direct contact with a light source to produce the desired wavelength. Due to this contact, there is a need for their properties to stay stable under relatively high operating temperatures for the lifetime of the device. Understanding limitations and finding ways to circumvent them is therefore critical for integration of CQDs into devices.

5.1.1 Processes behind thermal degradation in QDs

One of the main barriers of CQD integration into devices has been the stability of CQDs properties. It is well known that CQDs degrade with prolonged combined exposure to light and oxygen, known as photo-oxidation. Photo-corrosion is another form of degradation that can affect CQDs through exposure to light of chemically unstable semiconductors. The mechanism of photo-oxidation works via surface oxidation of the CQD particles and causes trap states to form on the QD surface. Adsorption of oxygen through the surface of the CQDs results in the formation of oxide bonds that results in these oxide molecules are released from the surface of the CQD into a surrounding medium[111]. This loss of atoms and molecules leads to fluorescent quenching. (Fluorescent quenching refers to the process of decreasing intensity from fluorescent particles through outside attributing factors such a thermal degradation). Photolysis can also affect the PL properties of CQDs through a mechanism where ions are produced on the surface of the QD causing dissociation of particles from the core. This dissociation of material from the core can cause a blue-shift in the emission wavelength, and PL spectrum broadening [110]. When

considering CQDs for integration into devices such as displays or lighting where colour purity is important, this is not an ideal outcome.

Research has been carried out on different methods of stabilising CQDs in different environmental conditions. One such way of doing this is through a well-designed shell materials and ligands that bind onto the QD surface [112]. The ligands on the surface of the QD give a physical barrier to prevent against trap sites, however this method of stabilisation does not provide much protection against heat. Relying on ligands to protect optical properties of CQDs against heat is not a sufficient protective method for device integration due to the permanent trap states created during expansion of the core, shell, and ligand material when they are heated. This expansion of the core material due to temperature can also cause lattice mismatches in the crystals, inducing strain, and resulting in dislocation of atoms from the QD surface. As a consequence, the structural changes induced cause permanent trap states which result in fluorescent quenching [113]. Stability of the ligands under heating is another reason that relying on this method alone is insufficient for protection. If the ligands are organic in nature, they themselves will be susceptible to degradation and decompose under higher temperature conditions which could result in them being damaged or removed from the QD surface reducing their ability to passivate dangling bonds.

A simple schematic representation of a QD 2-level transition is shown Fig. 5-1 in a) and in b) the same energy levels where a permanent trap state has been created to demonstrate how fluorescent quenching can occur through non-radiative decay. In Fig. 5-1 a) the process of photon generation is shown. The green arrow represents an electron being excited from its ground state in the valence band to the conduction band. The orange arrow represents the electron relaxing from its excited state to recombine as an electron- hole pair. It is this relaxation process where the energy created from recombination is emitted as a photon. Fig. 5-1 b) shows how a trap state creates non-radiative decay. After an electron-hole pair is created some of the energy created is lost through phonons and the electron relaxes to a lower energy state which is not the ground state. The energy becomes “trapped” and is no longer able

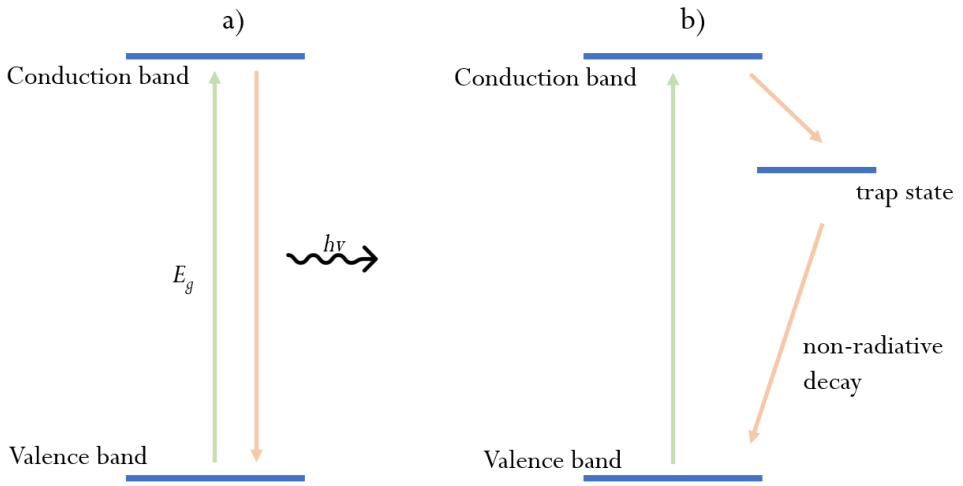

Fig. 5-1 a) schematic showing a QD bandgap b) schematic representation of QD bandgap with permanent trap states generated by heat.

to emit a photon. This results in the electron decaying non-radiatively to the ground state. This process shortens the fluorescence lifetime of a quantum dot and leads to quenching.

An alternative route to improving stability of optical properties under environmental conditions is to incorporate the CQDs into a polymer matrix to form a colour converting composite. Since CQDs are synthesized via wet chemistry methods and the nanocrystals are coated in an outer layer of ligands they are readily combined into polymer matrices depending on the type of ligands. Another advantage of mixing CQDs with polymer materials is that many polymers such as polydimethylsiloxane (PDMS) and polymethyl methacrylate (PMMA) do not require heat to cross link the polymer chains which could contribute to accelerating the degradation process of the CQD properties.

5.1.2 Polymer Properties

Polymers are materials that are made of repeating chains of molecules. Their properties such as molecular weight, molar volume, density, degree of polymerisation and crystallinity of material can vary greatly according to how these repeating chains are made up [114].

One of the most common and versatile polymers used for device integration is PDMS. It is a silicone elastomer that can be cross-linked with different ratios to change the elasticity of the polymer. PDMS has many desirable properties such as high optical transparency in the visible, chemical stability, high gas permeability, biocompatibility, thermal stability and ease of fabrication [115]. It is used in many applications such as device integration, protective coating in electronics, biomedical sciences, cell engineering and microfluidics [116], because of its versatility. Although PDMS is relatively permeable to oxygen which could affect the stability of the CQDs, it can withstand a temperature range of -50 to 200 ^{o}C [117], [118], making it a suitable choice for a colour converting material. This temperature range would allow the material to withstand µLED junction operating temperatures of up to 85 ^{o}C [119].

Another polymer which is often used as a protective coating for QDs is polymethyl methacrylate (PMMA). PMMA shares many of the same properties as PDMS such as high optical transparency, biocompatibility, and chemical stability as well as less water permeability [120]. Although PMMA has good thermal stability from -70 to 100 ^{o}C, this was not a high enough upper limit for the purposes of our research carried out in this chapter.

In this chapter, we study the effect of heat, independently of the photooxidation process, on the luminescent properties of PDMS/CQD colour converting composites. To achieve this, composite samples are annealed under vacuum at different temperatures and durations. The photoluminescence characteristics of thermally treated composites are compared to untreated samples. Samples of neat CQDs are also measured to assess the effect of the PDMS matrix on the overall CQD optical property stability.

5.2 Fabrication and Characterisation of Colour Converting Composites

5.2.1 Composite Sample Fabrication

The colour converters were fabricated using commercial CQD solution from Cytodiagnostics (CdS_xSe_{1-x}/ZnS 575 nm intrinsic wavelength, 50 mg/ml concentration in toluene with alkyl ligands). The stock CQD solution was diluted by adding toluene to lower concentrations of 22.5 mg/ml, 17.5 mg/ml, 12.5 mg/ml, and 6mg/ml. 400 µL of this solution was then added to 1.8 grams of PDMS (Sylgard 184) which was mixed at a ratio of 10:1 elastomer to cross-linking agent. The PDMS was mixed for approximately 3 minutes to ensure the CQD solution was well incorporated into the silicone mixture with a uniform dispersion. Once stirred the CQD/polymer mixture is poured into a petri dish left to de-gas for 1 hour under vacuum before being heated at 80 °C for 6 hours on a hot plate to reduce the time taken to set. Individual samples are cut from the same composite sheet, and have a thickness of 0.8 mm.

5.2.2 Neat Sample Fabrication

Samples consisting of a neat film of dense CQD solution were fabricated and used as a control to determine the protective effect of encapsulation with PDMS on CQD optical properties. Using a spin coater (Spincoater, Model P6700 series), CQD solution at a concentration of 22.5 mg/ml and 12.5 mg/ml respectively were drop cast onto an 18 x18 mm glass cover slip and spin coated at 500 rpm for 40 s to produce a neat film.

5.2.3 Thermal Annealing

The individual composite samples were heated in a vacuum oven (Memmert VO200) under a 50-mbar vacuum and a range of temperatures: 125°C, 150°C and 200°C. Each concentration of CQD/PDMS composite and neat film were heated in the vacuum chamber for either 4 or 8 hours to determine the effect of prolonged high temperature exposure on PL output of the quantum dots and the effectiveness of

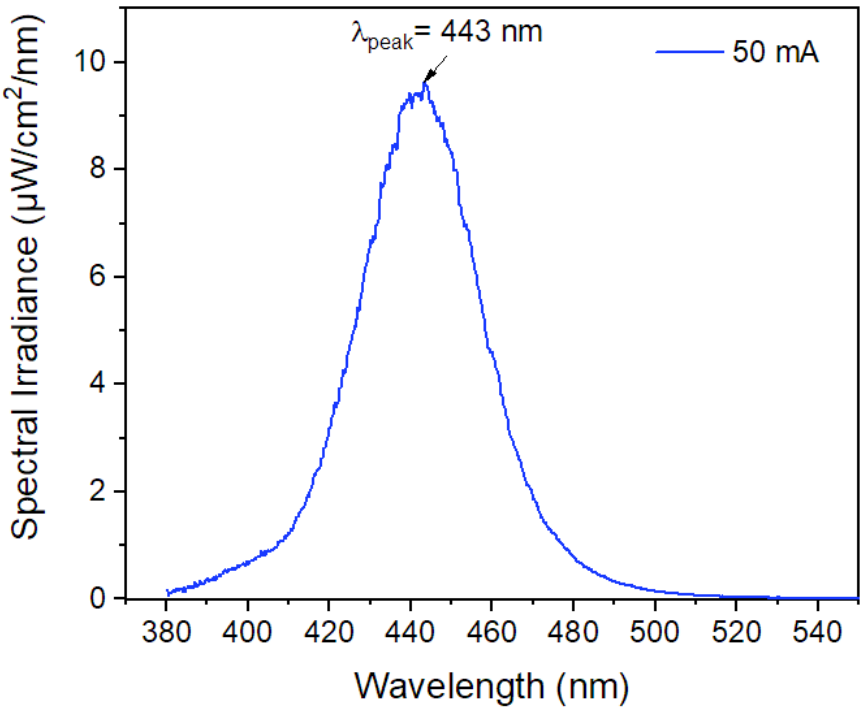

Fig. 5-2 PL spectrum of µLED driven at current of 50 mA, with a peak wavelength emission of 443 nm

PDMS as a protective barrier on these properties. The neat samples were also subjected to heating as described above.

5.2.4 Control Samples

For each concentration of colour converting samples fabricated a piece was left untreated at room temperature 25 °C as a comparison of the PL properties.

5.2.5 Characterising Composite Photoluminescent Properties

The excitation source used to characterize all the samples in this chapter was a 45x45 µm^2 flip-chip gallium nitride (GaN) µLED. For spectral irradiance measurements the µLED was driven at 50 mA producing an output power of 1 mW for an emission peak at 443 nm, which is shown in Fig. 5-2.

To determine the spectral irradiance, the spectrometer must first be calibrated using a tungsten halogen lamp (Ocean Optics, HL-2000), this procedure is outlined in more

a)

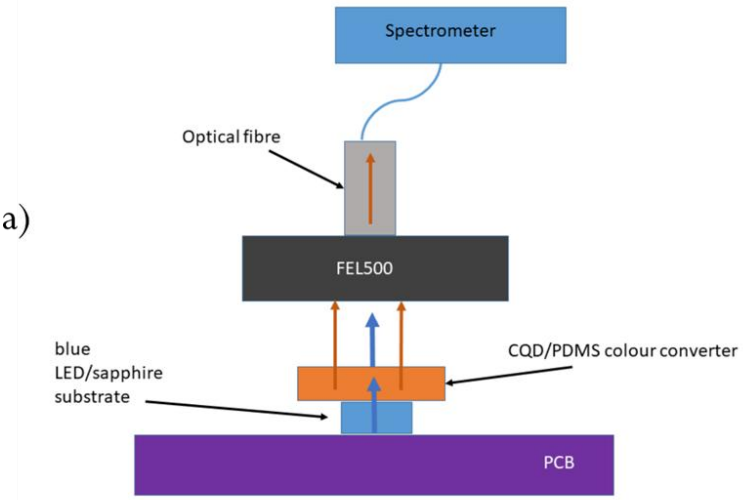

b)

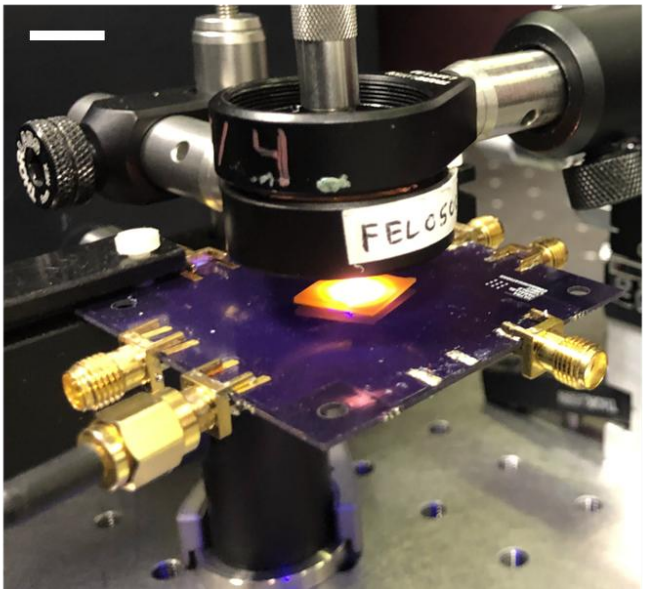

Fig. 5-3 a) Schematic of CQD/PDMS composite in "converter on top" configuration placed on sapphire substate of µLED b) image showing the set-up with SMA connecters and LED mounted on PCB with 1 cm scale bar

detail in section 3.2.8 The samples were placed directly on the sapphire window of the µLED in a "converter on top" configuration, as shown by the schematic and image in Fig. 5-3 a) and b). The excess excitation light was filtered using a long pass filter (Thorlabs, FEL500) to determine the spectra emitted from the composite and neat samples only. The spectral irradiance data was collected using a fibre coupled CCD spectrometer (Ocean Optics, USB 4000).

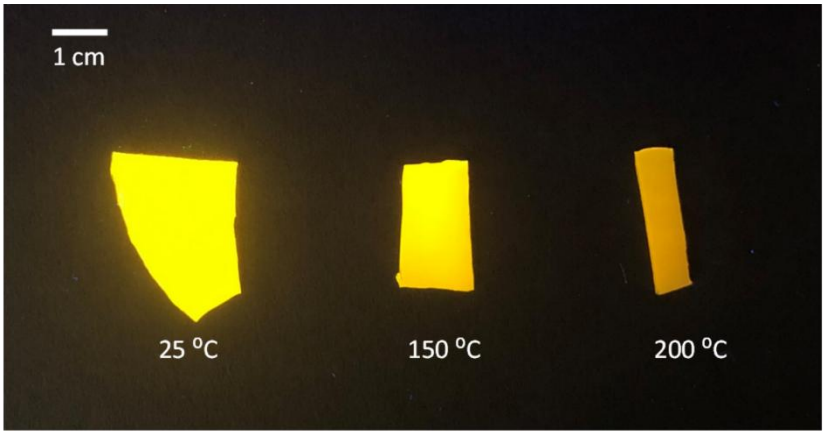

Fig. 5-4 Image of 3 different CQD/PDMS composites under UV excitation. The first sample shows the untreated room temperature (25 °C) colour converting sample compared with 2 other samples that were thermally treated for 8 hours, one at 150°C and the other at 200°C. As temperature increases, a colour change is seen between the three samples. Darkening indicates QD quenching.

5.3 Experimental Results and Discussion

5.3.1 Visual Inspection of Composites

An image comparing the composites is shown in Fig. 5-4. It can be seen in the image that there is a darkening in the colour of the composites from left to right as the temperature increases. This could suggest the QDs within the composite matrix were degrading and the intensity output of the QDs has reduced as temperature has increased.

5.3.2 Evaluation the Effect of Different Concentrations on Spectral Irradiance

Fig. 5-5 a) and b) shows a comparison between spectral irradiance results for untreated neat samples and CQD/PDMS composites. The peak emission wavelength of the neat samples is 581 nm for both concentrations shown, with maximum spectral irradiance values of 0.03 µW/cm^2/nm for the 12.5 mg/ml sample and 0.04 µW/cm^2/nm for the 22.5 mg/ml sample. For the CQD/PDMS composite samples the peak emission wavelengths for the 12.5 mg/ml is 584 nm with a maximum spectral irradiance value of 0.34 µW/cm^2/nm and at a concentration of 22.5 mg/ml the peak emission wavelength is 585 nm with a maximum spectral irradiance value of 0.63 µW/cm^2/nm. As expected, for the samples with higher CQD concentration the spectral irradiance values are higher. This is due to the higher number of QD emitters present in the samples at higher concentrations, leading to a higher optical density of QDs and conversion of µLED pump light. The higher optical density of the CQDs will also contribute to the red shift of the PL spectrum between the neat and composite samples. The spectral bandwidth of the neat samples shown in Fig 5-5 a) is 30 nm for both samples shown, however in b) there is a difference between the spectral bandwidth for the two concentrations. The 22.5 mg/ml sample spectral bandwidth has broadened to 40 nm and the 12.5 mg/ml sample is lower at 25 mg/ml. This difference in spectral bandwidth is likely due to irregularities in the uniformity and thickness of the composite samples.

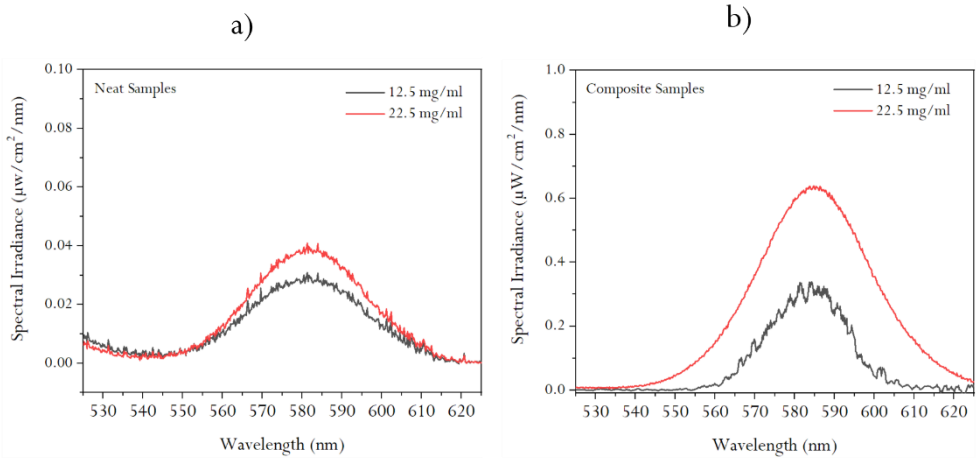

Fig. 5-5 Plot showing spectral irradiance vs. wavelength for non-annealed neat film samples b) spectral irradiance vs wavelength for non-annealed composite samples.

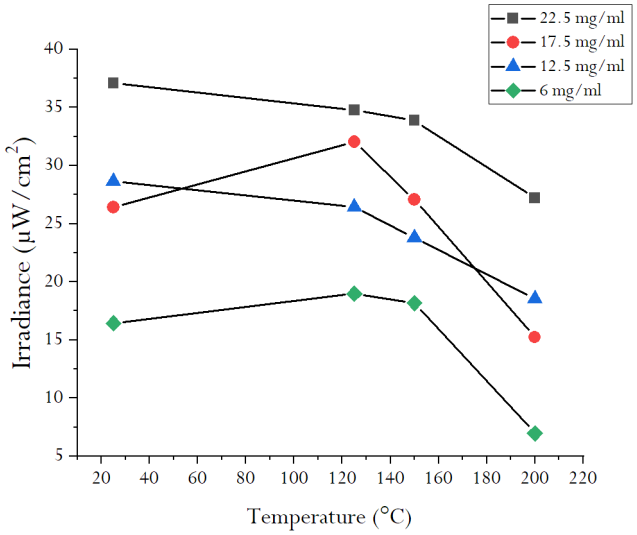

Fig. 5-6 Decreasing peak irradiance with increasing temperate for 4 different concentrations of composite samples that have been thermally treated for 4 hours

5.3.3 Increasing the Temperature on Composite Samples

The overall effect from increasing temperature on 4 different concentrations of composite samples can be seen in Fig. 5-6. After 4 hours prolonged exposure to temperature the irradiance output of the samples remains stable until 200°C where a large reduction is seen. The decrease in irradiance is likely due to the increased thermal vibration effect of the QDs due to an increase in thermal activation energy which would contribute to creating permanent trap states and increase non radiative Auger recombination [121], therefore causing fluorescent quenching and a decreased irradiance output from the CQDs. It should be noted that the trend line seen for the 17.5 mg/ml sample does not follow the same expected pattern in irradiance values as the other samples, this is likely due to fabrication inconsistencies such as thickness and even QD distribution throughout the samples. While it is seen here that there is a reduction in irradiance output, the peak emission wavelength remains unchanged. Normally during the oxidation process, the output wavelength of the QDs would shift towards the blue end of the electromagnetic spectrum [122]. This could indicate that the irradiance decrease can be attributed solely to thermal degradation and photo-corrosion / photo-oxidation was not a contributing factor.

However, this study was limited to 4 hours so it should be noted that this effect on wavelength requires further investigation at longer treatment durations to determine if photo-corrosion occurs. From Fig. 5-6 the decline in irradiance is greatest at 200°C, this trend is seen for all composite samples and could be accelerated by the host the matrix itself. At such temperatures it is possible the PDMS material itself could contribute to further degradation by maintaining a higher temperature within the material via an insulator effect. Another possibility is the PDMS material beginning to breakdown as the upper limit of its temperature stability range is being reached as mentioned previously in section 5.1.1.

5.3.4 Outcome of photoluminescent properties after increasing heating duration

To evaluate the effect of increasing the duration of time that CQDs were exposed to heat on PL properties, peak irradiance values at one temperature were assessed. The samples were exposed to elevated temperatures for durations of 0, 4 and 8 hours. The results for composites that have been heated to a temperature of 200 ° C are shown in Fig. 5-7. The trend indicates that at longer durations of exposure to higher temperatures, the decrease in the peak irradiance output of the CQDs is larger. When comparing the 22.5 mg/ml composite sample at 4 hours and 8 hours, the percentage decrease in irradiance from the room temperature values was 29 % and 32 % respectively for this concentration. For the composite with a lower concentration (12.5 mg/ml), at 8 hours of heat exposure, there is a decrease in irradiance of 56% compared to its room temperature counterpart. When evaluating irradiance values of the neat film samples, the decrease in irradiance output is even larger at an 85% reduction from the room temperature value at a concentration of 22.5 mg/ml. This shows the the effect of temperature on the neat film samples was greater than the equivalent concentration of CQDs that had been encapsulated in PDMS. Here we have shown that when comparing samples that have been exposed to heat for longer periods of time compared to room temperature samples, that there is an increasing degradation of irradiance output with exposure time. This effect is seen for both neat samples and composite samples, although to a lesser degree for the composites. This

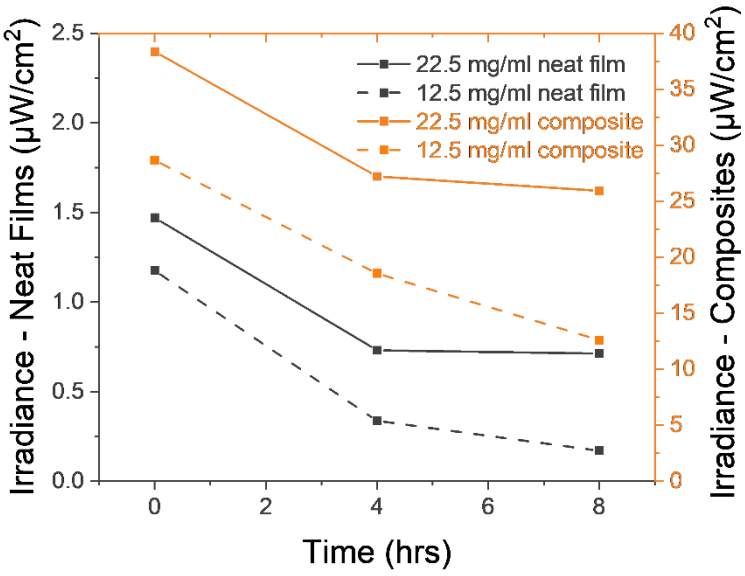

Fig. 5-7 Comparison on the effect of temperature duration on 2 different concentrations of neat film samples and composite samples for 0, 4 and 8 hours.

indicates that the polymer matrix is providing a beneficial effect and providing some protective against heat due to the smaller percentage decrease in irradiance for the CQD/PDMS composite samples.

5.3.5 Effect of temperature on wavelength

It has been reported that as the temperature increases and thermal quenching of QDs occurs a blue shift in the emission spectrum can occur [121]. Fig. 5-8 shows results for change in emission wavelength for one concentration of CQD/PDMS composite (12.5 mg/ml), as the duration of time three composite samples were exposed to three different temperatures. A small negative shift in the output wavelength of CQDs can be seen. This negative shift correlates to a wavelength shift towards the blue end of the spectrum. However, this apparent shift is not statistically significant as the measured values are not out with the standard deviations for any of the temperatures measured as shown in Fig. 5-8. When there is a blue shift in wavelength from semiconductor materials, this occurs when permanent trap states cause thermal quenching due to photo corrosion of the QD core. Due to the relatively short duration of thermal exposure, and the lack of evidence found for these samples studied, it is not possible at this stage to gauge the significance of this effect for these

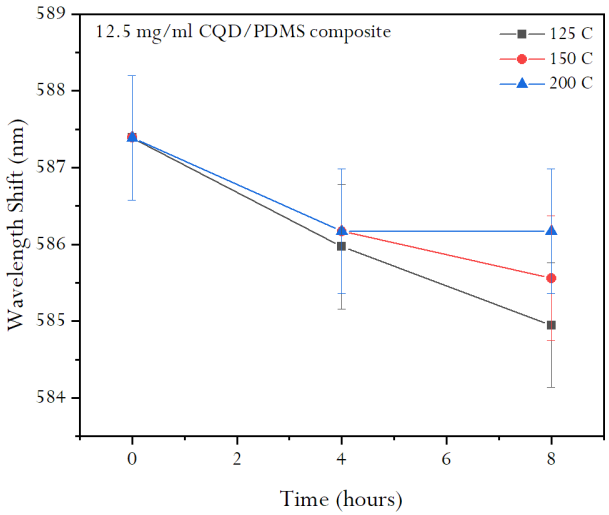

Fig. 5-8 trend of wavelength shift versus heat exposure time for one concentration of CQD/PDMS composite at three different temperatures

samples. Further investigation is required for longer time durations at different concentrations of composites to determine if the small shift in wavelength seen in Fig. 5-8 occurs at when exposed to temperature only.

5.4 Summary

In this chapter we have explored the isolated effect of heat on the stability of the photoluminescence properties of a CQD encapsulated in an elastomeric polymer without the presence of oxygen. Results showed that embedding CQDs in a composite material provides a protective effect from heat to the optical properties of the CQDs such as irradiance, when they are compared to an unprotected neat film. An operating temperature of 150°C has been determined, where exposure to temperatures below this limit will not yield significant detrimental effects on PL output of CQDs. These results are found to be independent of other photo-induced or oxygen-related phenomena such as photooxidation. The damage to CQD PL output was compounded with the duration of time the CQDs were exposed to heat. Overall, the results presented in this chapter offer useful information for tolerancing operating conditions for mechanically flexible colour converters into practical device and systems, such as solid-state lighting or displays

Chapter 6

6 On demand single photon emission from quantum dot source

6.1 Introduction

In this chapter research is presented towards an on demand (deterministic) source of single photons, which could be used for example in a quantum key distribution setting. The novel device structure that is proposed is based on a colloidal quantum dot (CQD) optically excited by a GaN LED. The CQD is the material used to generate single photon emission. CQDs are a solution processible, alternative to epitaxially grown quantum dots that could potentially be easier or cheaper way to produce fabricate single photon devices. Although epitaxially grown QDs have been established as excellent materials for a single photon source due to their high single photon purity, there are challenges for their integration into devices for use out with laboratory settings. For example, the requirement for operation within an engineered cavity optical cavity or waveguide structure [123] and to be cryogenically

cooled to maintain single photon operation due to small separations between quantised states [33], [124].

The work reported here was part of a collaboration of efforts between three institutes that were responsible for different aspects of the device build. Fraunhofer Centre for Applied Photonics (FhCAP) was responsible for the quantum integrated optics, Fraunhofer Institute for Microengineering and Microsystems (IMM) main role was the synthesis of the quantum dots, and the Institute of Photonics (IoP) were to support with polymer embedding and nanoscale accuracy transfer printing. Transfer printing (TP) is a pick and place technique that enables objects from a donor substrate to be retrieved/picked-up and transferred to a receiver substrate of different material [125], [126]. This technique can provide a method to integrate pre-fabricated structures such as µLEDs, and flexible integrated circuits [126] and polymer films [127].

In the following, after a basic introduction to the concept of quantum key distribution and the main characteristics of single photon sources, we present the structure of the proposed device, and outline the experimental methods and results. We give an overview of the project but focus our report and discussions on our own experiments and results. In particular, we report on the fabrication of solid-state CQD/polymer samples, optical characterisation of CQDs in solution and of PL characterisation of the solid-state samples (including PL mapping and attempts at single photon generation). While single photon generation has not been achieved in our CQD samples yet, efforts have enabled the establishments of an approach for sample preparation and of a confocal micro-PL set-up for single photon experiments. In the results section we report on the confocal PL map capability, as well as the HBT measurements on thin film nanodiamond samples and CQD thin film samples using solutions provided by IMM.

It is to be noted that this part of our work was the most severely impacted through the COVID-19 pandemic and through various factors such as restricted lab access and my access to the lab being limited, did not move past the proof-of-concept design towards iterative improvements. Still, we progress towards such a device technology.

6.2 Applications

The main applications for single photon sources are related to quantum information technologies, such as quantum key distribution as mentioned in more detail in the following section. Other applications include quantum computing and quantum metrology [128], [129]. Epitaxially grown QDs which emit in the visible spectrum have shown promise in quantum cryptography with was intended for secure communications such as QKD via free space connections or optical fibres [130], [131].

6.3 Quantum Key Distribution

Quantum key distribution (QKD) is an area of research related to quantum cryptography that is being investigated to help improve security of communications by using photons as an encryption source. Using photons to encrypt information provides a secure source that is protected by the laws of physics making it harder to be intercepted by illicit sources. QKD takes advantage of the quantum nature of photons, where their state will change depending on whether they have been observed or not.

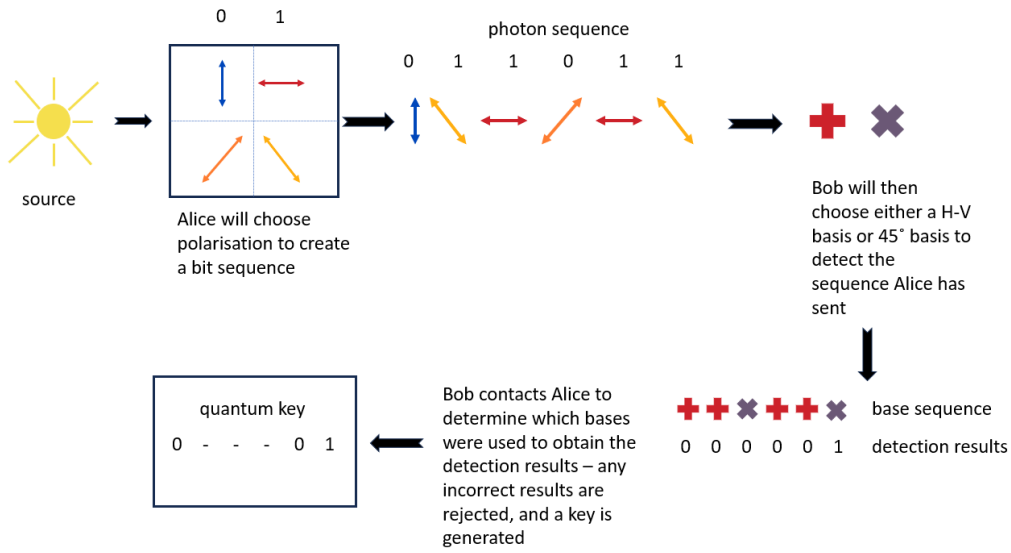

Fig. 6-1 representation of the flow of work and concept of how a quantum key is created using a laser source and polarisation filter as per the BB84 protocol.

To describe the concept of QKD in simple terms, the usual example of “Alice” as the transmitter of information and “Bob” the receiver of information is used. A schematic representation of this process is shown in Fig. 6-1.

The concept relies on quantum states of single photons, which can be for example the polarisation. Alice can send photons with a particular polarisation direction to Bob at a different location using an attenuated laser source by using different polarisation filters. The photons can be polarized in orthogonal direction pairs, this can be as horizontal and vertical (H-V), or 45° and 135°. Bob will then use either a H-V or 45° basis with two detectors to determine the orientation of the photons he receives. The detectors will then convert the polarization directions into a series of zero's and one's depending on the whether the correct direction of basis filter was applied to determine the results. Bob will then compare which filter bases were used with what Alice used to create the sequence and he will reject the photons that were detected with an incorrect polarization. The sequence that they are left with of zeros, and one's is known as the quantum key. With this quantum key, Alice can encode a message and transmit this on a classical communication channel to Bob, who will decrypt the code using the quantum key. The element of QKD that makes using single photons more secure is their quantum mechanical nature. An attenuated laser source will create the single photons through weak coherent pulses, which is a probabilistic source of single photons relying on photon statistics to produce single photons which can be a lengthy process overall for producing secure keys. If a key is created using weak coherent pulses, there is still the probability of multiple photons or no photons being generated rather than only single photons. This will introduce a higher error rate in the instance of multiple photons or reduce the rate of key production if there are zero photons produced. One method Alice may use to avoid eavesdropping on key generation by an unknown third party is to generate additional states known as decoy states. The decoy states have different intensities giving different photon number statistics compared to the single photons used for key generation and following transmission the bit error rate is evaluated between Alice and Bob to determine the genuine QKD. However, if a deterministic single photon source were to be utilised instead the probability of multiphoton events is negligible, allowing for a more secure quantum key generation.

A deterministic single photon source is an on demand source for single photons that means a single photon could be produced when it is chosen to be triggered rather than relying on photon statistics [132].

One current drawback with QKD systems is finding a reliable source to provide single photons on demand so that keys can be generated when needed. Sources of single photon emitters are outlined in the following section.

6.4 Single photon purity

The main characteristics of an ideal single photon source (SPS) would be the ability to produce single indistinguishable photons on demand which allows for photon-photon interference such as the Hong Ou Mandel Effect [128], [133]. Such photons are required for quantum information processing, where photon-photon interference is a building block for these processes. These characteristics would allow the beginning of integration of SPSs into practical devices for applications such as distribution of encryption keys in QKD and quantum imaging. The requirements for practical device integration on the characteristics of SPSs would include: room temperature operation, low manufacturing costs, sub nanosecond fluorescence emission (which will give a higher repetition rate, i.e. higher frequency of emission) and be electrically driven [124]. Another desirable characteristic of the SPS would be to have a tuneable emission wavelength so that it could be easily matched to an application.

The term purity is used to quantify how well an excited source will emit a single photon. The purity of SPSs can be determined using the second order intensity correlation function [$g^{(2)}(\tau)$], a SPS is thought to be ideal when this function gives a value of zero. The second order correlation [$g^{(2)}(\tau)$], can be given by Eq. 11, where $I(t)$ is the measured photon intensity counts at time t at one detector, and $I(t+\tau)$ is the measured photon intensity counts at the second detector with a time delay of τ.

$$g^{(2)}(\tau) = \frac{\langle I(t)I(t+\tau)\rangle}{\langle I(t)\rangle\langle I(t+\tau)\rangle} \tag{11}$$

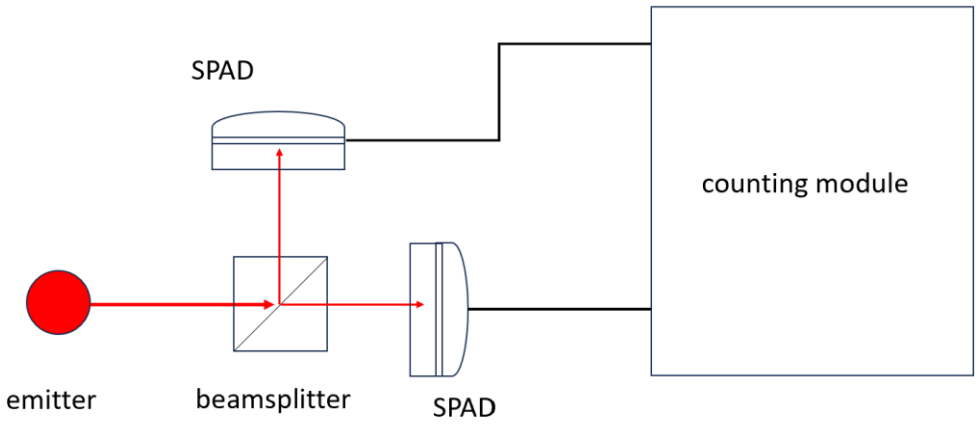

Fig. 6-2 schematic of a simple Hanbury-Brown and Twiss set up. Emission from an excited emitter is sent to two single photon detectors (SPADs) using a beam splitter. The two detectors are connected to a counting module which counts the photons received from the detectors and determines the second order correlation function calculated from a time delay.

Eq. 11 describes how the intensity correlation is a function of the time delay between two photon events arriving at detectors when measured using a Hanbury Brown and Twiss (HBT) experimental set up – shown in Fig. 6-2.

There is a characteristic dip at zero time delay (shown in Fig. 6-3 a), known as photon antibunching where $g^{(2)}(0) = 0$. This value of zero would represent an ideal photon source, however in practical applications an emitter is deemed an SPS when $g^{(2)}(0) < 0.5$, with a value of < 0.1 being a very high purity SPS [124].

Fig. 6-3 b) represents the photon statistics for a single emitter under pulsed excitation where the characteristic $g^{(2)}(0)$ dip appears different. Here a dip at zero is seen amongst the recorded pulse trains in the repetition of the laser pulse emission.

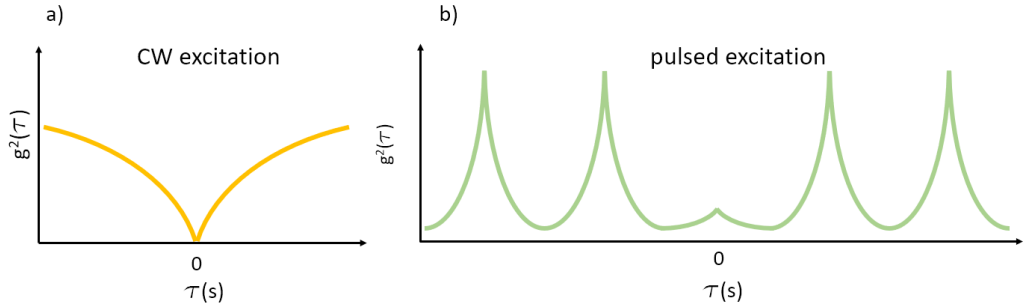

Fig. 6-3 a) schematic representing antibunching at zero time delay under continuous wave excitation for a quantum emitter b) the second order correlation under pulsed excitation still exhibits a dip at zero delay surrounded by the pulse train emitted by the laser.

6.5 Sources of single photon emitters

One of the main challenges of QKD is generating single photons when they are required and in a controllable manner. The photons must be ideally generated by a quantum source, with a high enough chance that only one photon will be produced when required i.e. with sufficient purity [128].

Trapped atoms are being investigated and used as single photon sources since they operate as a two-level system. They provide a source where the emission properties are reproducible and identical sources can be made and used. This characteristic of trapped atoms gives the possibility of multiplexing applications [134].

Colour Centres are defects within a crystalline structure of a material that can introduce additional properties such as increased absorption or emission of light. Usually, the host material is transparent, and the defect can be used to colour the material (much like how chromium colours aluminium oxide to form a red crystal, i.e., ruby). The defects can be created by different methods such as a vacancy, addition of an impurity or substitution. An atom that has been removed or is absent naturally from the crystalline structure is known as a vacancy. An atom which is within the crystal matrix that would otherwise not be present is known as an impurity. Substitution of one atom for another in the crystal lattice is another way that a defect can be created. It is these defects that provide additional levels in the energy bandgap of the host material that lie between the conduction and valence band of the material allowing lower energy photons to play a role in the absorption and emission dynamics and giving the material their photoluminescence characteristics. Nitrogen vacancy (NV) diamond is one of the most well used and studied colour centre materials [49], [135] for single photon emission. Nitrogen atoms can be inserted into the crystalline structure of diamond via forced substitution but can also occur naturally. Other atoms such as germanium and silicon can be added to diamond to enhance the materials optical properties. Another similar material that has shown promise for single photon emission which makes use of colour centres is silicon carbide (SiC). The colour centres often used in SiC are divanacy (DV) or substitution with a transition metal such as titanium or chromium [136]. One of the main advantages of using

colour centres is that they can be considered as isolated atoms [135] as they don't interact with the host material. The defects are excluded from the energy transitions from the valence to conduction band and when electrons are excited into the defect level, they are more likely to emit a single photon from this transition. The colour centres are also more readily incorporated into devices as they are a solid-state medium, unlike trapped atoms which require cooling and an optical cavity for trapping.

6.5.1 Colloidal Quantum Dots as a single photon source

Semiconductor quantum dots often nicknamed "artificial atoms", are another candidate for an ideal single photon source that have been shown to emit single photons [137]. The type of QDs that have been most successful as single photon sources are made from III-V semiconductor material [137]. For single photon emission epitaxially grown QDs have some advantages such as site control during growth and fabricating the QDs within a photonic cavity [138]. Although antibunching has been demonstrated with epitaxially grown QDs, due to the small separation between quantized states, they have required operation at cryogenically operated to demonstrate single photon emission [33] which would prove more challenging for integration into a compact device.

CQDs are beginning to show promise as single photon emitters due to their ability to operate at room temperature [139]. This reduces the need for cryogenic cooling, and their flexibility in design parameters such as size, emission wavelength and shape also provide desirable properties for a single photon source. CQDs have a higher degree of quantum confinement in comparison to epitaxially grown QDs which is one of the reasons their single photon emission is demonstratable at room temperature as their quantum characteristics are preserved at higher temperatures [33]. Antibunching recorded from single CQDs has been attributed to the high efficiency of Auger recombination of multiexcitons [139]. Auger recombination is a non-radiative process where excess energy from electron-hole recombination is transferred to other electrons or holes in the material, causing subsequent cascading excitation of

carriers to an excited state within the same band without emitting any photons. Fast Auger recombination can help to suppress multiphoton emission making CQDs robust single emitters which would be independent of temperature [33]. Although fast Auger recombination can be of benefit to SPSs, if the radiative recombination of carriers doesn't occur on a fast enough scale intermittent 'blinking' of the emitter could reduce the purity of SPS by being in an off state and ways to control this should be considered. In the case of quantum emitters this could result in an unstable signal when using the SPS for creating an encryption key for QKD. 'Blinking' is a characteristic determined by intermittent luminescence of an emitter where brightness states are switched between i.e. on/off, under continual optical excitation [140]. To eliminate blinking entirely, a thick shell can be grown on the QD core which comes with its own difficulties. Embedding a single QD in a polymer is one method that has shown to reduce the incidence of photobleaching [141].

Although CdSe QDs are a more mature and popular material to use as single quantum emitter, perovskite quantum dots (PQDs) have recently shown promise as single quantum emitters. Large improvements in their photovoltaic properties due to perovskite solar cells mean they would be a good candidate to suit the electrically driven characteristic that is desirable for a SPS as well as being solution processible, with the ability to operate at room temperatures. However, they are still in their infancy due to stability issues such photo induced degradation.

6.6 Single Photon Avalanche Detectors (SPADs)

Single photon detection requires sensitive detectors such as silicon SPADs. These detectors are commonly used in experimental laboratory settings and for free-space QKD. They offer the advantages of having low dark count rates which are needed to distinguish single photons above the baseline background noise, while giving high count rates in the visible to near infra-red spectrum and maintaining high detection efficiencies of approximately 80%. The SPAD is based on an avalanche photodiode structure of p-n or p-in junction. They are operated Geiger mode which is in reverse-bias above the breakdown voltage. Carriers are generated when photons are absorbed by the junction and can create an avalanche gain that triggers breakdown

in the diode junction. Typically SPADs will have photon sensitivity from 400 – 1000 nm and reaching peak sensitivity at approximately 650 nm [142].

In the following sections the proposed device for the QuDos project is outlined and the experimental methods used to make progress towards achieving this final device.

6.7 Device Design

The design proposed for this project would provide a novel device for deterministic single photon generation. Most devices that are currently used for single photon generation are impractical due to their requirement for cryogenic operating temperature or complex operating systems. The proposed design incorporates a 450 nm µLED pump source, which would be used to excite an isolated single quantum dot that has been embedded in a polymer to help protect the emitter emission characteristics. To collect the emission that is generated from the single quantum dot, a single mode optical fibre would be aligned with the emitter using nanoscale accuracy transfer printing. Transfer printing is a technique which uses a pick and place strategy of to fabricate micron or nanoscale devices. A polymer stamp - usually made from PDMS is used to release a device from donor substrate and is subsequently released onto a different host substrate or onto an integrated circuit. Samples are then mounted onto a high resolution translation stage which incorporates the use of an optical microscope as the imaging system to aid the positioning of the donor and substrate relative to one another, viewed through the transparent stamp and placed accordingly with micro to nanoscale precision.

A schematic of the proposed final device is shown in Fig. 6-4.

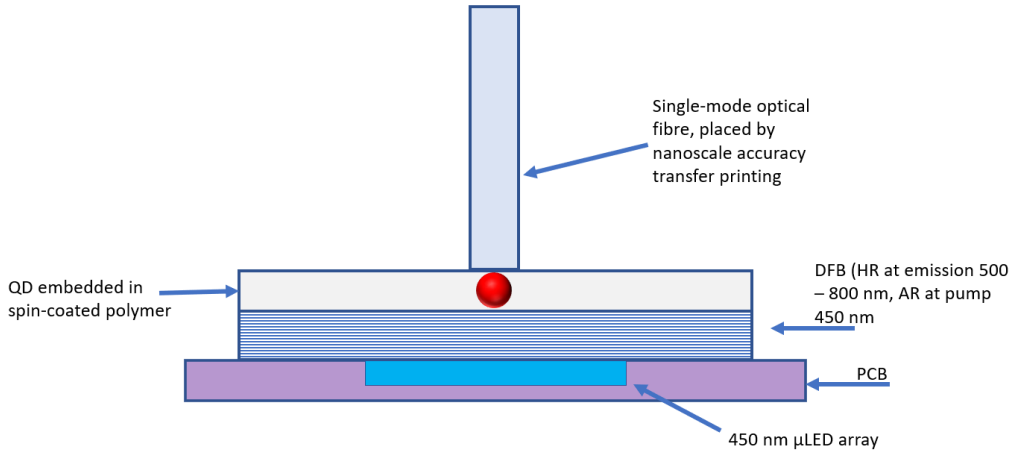

Fig. 6-4 Concept of final for a novel deterministic single photon source (not to scale). A single mode fibre is coupled to the single photon source – in this instance a QD. The excitation source is a µLED so allowing for miniaturisation and portability, and the possibility to create arrays of sources.

The design proposes the use of colloidal quantum dots as the single photon source for their ease of use, high photon efficiency at room temperature in comparison to epitaxially grown active nanostructures which can suffer from low yield in the manufacturing process. The emission wavelength of the QDs will be tailored to match the peak absorption efficiency of the silicon single photon avalanche detectors (SPAD), which is in the range of 630 – 680 nm. Due to the broad absorption of QDs the emission of the pump source can be tailored to visible wavelengths such as 630 – 680 nm, such that excitation with GaN based LEDs are ideal. Other characteristics for the QDs which would be important to optimise for device design would include, high quantum yield (PLQY), high photostability and low blinking.

Incorporating the use of transfer printing with nanoscale precision will also aid with increasing the yield of the devices during the manufacturing process. The device geometry allows for a compact integrated pump and fibre output which will make it attractive for commercial exploitation.

So far, we have outlined the final device design, however the project looks to develop and demonstrate single photon emission through several stages with the main aim to be a demonstrator system with commercial applications due to device geometry, with reduced size, weight, and power.

6.7.1 Quantum Dot Synthesis

The quantum dots (QDs) used in this chapter are custom made quantum dots from a project partner Fraunhofer Institute for Microengineering and Microsystems (IMM) using a continuous solution processing, the details are outlined in section 6.7.1.2. The intention was to use QDs for the final device, however synthesizing QDs at the desired wavelength of 630 nm proved challenging and further refinement using the continuous flow synthesis was required for dots with a sufficient quantum yield to be realised. This led IMM to provide quantum rods that have a more established synthesis and quantum yield with this method.

6.7.1.1 Custom QDs

The specification given to IMM for emission properties of the QDs were in the range of 630 – 680 nm to match the peak absorption of the SPADs used in the micro-PL set up. From initial discussion the first batch (Batch 1) of solutions sent had an emission wavelength of 650 nm. A second larger batch (Batch 2) of solutions were then sent as the continuous solution processing set up was improved with wavelengths ranging from 580 to 600 nm. Finally, a third batch (Batch 3) of quantum rods were sent as the synthesis proved more reliable at the specified wavelength range of 630 to 680 nm. These had an emission wavelength of 630 nm. The variations in emission wavelengths sent from IMM are attributed to the synthesis process and refinements their facility made to along the course of the project. The details of the QD solutions are provided by Fraunhofer IMM following synthesis and given in Table 4.The photoluminescent quantum yield (PLQY) gives an indication of the amount of excitation light which is absorbed by the CQDs and converted into emission by exciting the electrons from ground state to the excited state and subsequently releasing that energy in the form of photons.

Table 4 Summary of QD properties received from Fraunhofer IMM

Batch	Material	Emission Wavelength (nm)	Shape	Photoluminescent Quantum Yield (%)
1	CdSe/CdS	650	dots	45 - 25
2	CdSe/CdS CdSe/ZnS	580 – 600 580	rods dots	7 - 86 38
3	CdSe/CdS	635	rods	60

6.7.1.2 Continuous Flow Solution Synthesis

Fraunhofer IMM were investigating a method to realise automated purification of colloidal quantum dot during the synthesis process. An image of this setup can be seen in Fig. 2-10, chapter 2. This was achieved through a combination of solvent-induced adhesion and solid phase extraction [43].

Previous works at the institute had set up a modular flow reactor [143], that helped with control of nanoparticle synthesis through separated seed generation and crystal growth. To help with reproducibility and accuracy - which is the main challenge when looking to scale the synthesis process for nanoparticles - this method encompassed continuous analysis of the solution. As the solution moves through the microfluidic flow reactor the optical properties are measured as it passes through the reactor set-up. The temperature could be controlled while the solution flowed to change the size of the nanoparticles being produced and therefore tune the optical properties of the QDs. Using a continuous flow process with a microfluidic system as opposed to a stirred batch synthesis process has the advantage of the ability to produce large quantities of monodisperse QDs through better heat control, residence time and mass transfer throughout the process [144]. An image of the solutions received from IMM is shown in Fig. 6-5.

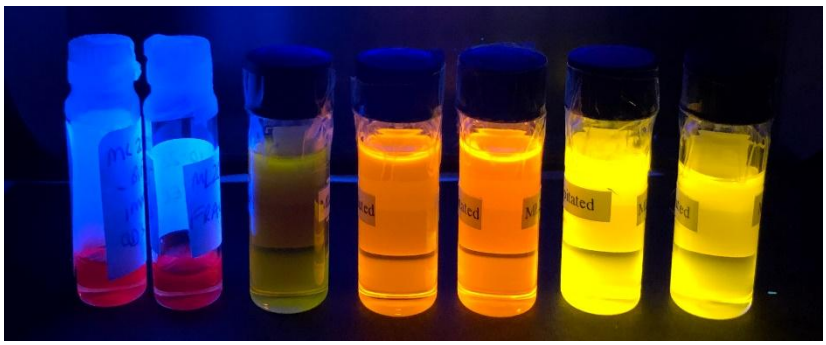

Fig. 6-5 Batch 2 of solutions synthesised by Fraunhofer IMM under ultraviolet excitation, showing the variation in emission wavelengths.

6.8 Experimental Methods

6.8.1 Characterising Samples

6.8.1.1 Photoluminescence and absorbance

To characterize the optical properties of the quantum dots solutions received from Fraunhofer IMM, the photoluminescent spectrum and absorbance spectrum were measured. Each solution was placed in a 1 cm x 1 cm microcuvette and then placed in a 4 – port cuvette holder (Thorlabs, CVH100). Depending on the solution a 396 nm µLED or a 532 nm laser diode (LD), (Thorlabs, 532 nm DPSS, DJ532-10) was used to

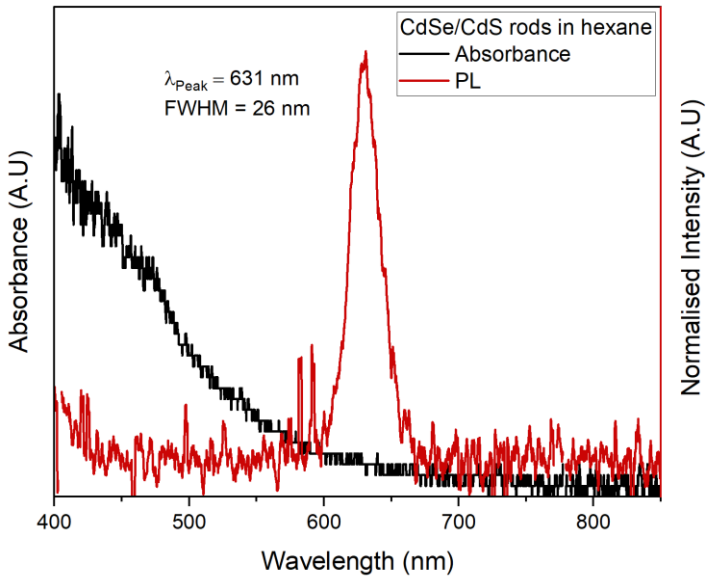

Fig. 6-6 PL and absorbance spectra for the CdSe/CdS quantum rods sent from IMM in batch 3 which was used to thin film samples shown in Fig. 6-9.

excite the solutions. The 396 nm µLED was driven at a current of 60 mA, or the LD was driven at 10 mW.

A spectrometer (OceanOptics USB 4000) was set up at 90 degrees to the excitation source in an edge detection configuration to collect the photoluminescent light emitted light from the CQDs. Using an edge detection configuration helps to avoid the spectra of the laser diode being collected at the same time as the CQD emission spectra. The absorbance spectrum was measured using a spectrophotometer (Thermo Scientific, GENESYS 30 Visible Spectrometer). a 1 cm x 1 cm microcuvette is placed within the machine while a single xenon flash lamp is used to scan the sample. A spectrophotometer measures how much light has been absorbed once it has passed through the CQD solution. This is used to give an indication of the wavelengths that could be used to excite the CQDs. The PL and absorbance spectra of the IMM solution that was used to fabricate thin film samples are shown in Fig. 6-6 showing a peak emission wavelength of 631 nm.

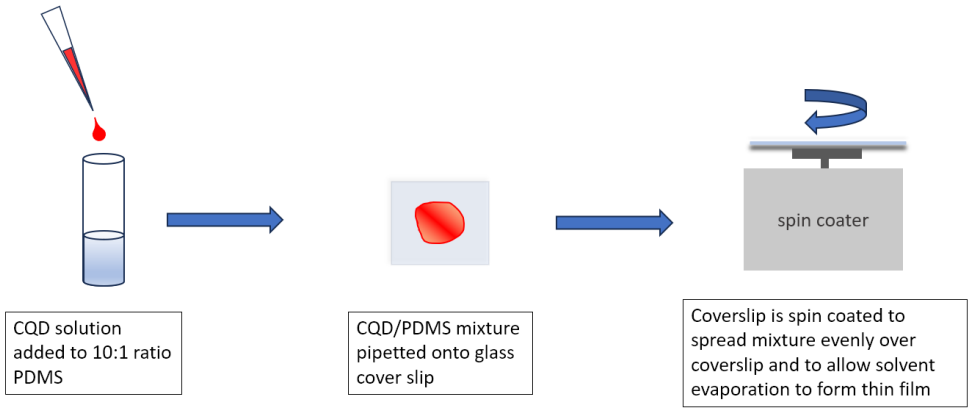

Fig. 6-7 representation of the flow process for thin film fabrication using CQDs or nanodiamonds.

6.8.1.1 Thin film composite method

To fabricate the thin film samples the same basic process was used for all the nanomaterials, as depicted in Fig. 6-7. A mixture of PDMS with a ratio of 10:1 was prepared, and CQD solution was added to this mixture. Thorough stirring was performed to ensure the CQDs would be well incorporated into the polymer matrix. Subsequently the CQD/PDMS mixture was then pipetted onto a clean glass coverslip. The coverslip was then positioned on the spincoater and the relevant speed settings were applied to evenly distribute the CQD/PDMS mixture across the coverslip, creating a thin film. Sectionss6.8.1.2, 6.8.1.3,6.8.1.4 give more specific steps of the process for each type of nanomaterial utilised in sample preparation.

6.8.1.2 PDMS/CQD polymer samples using commercial CQD solution at high concentrations.

To test the spin coating procedure, 10 µL of commercial CQDs were incorporated into PDMS. 25 mg/ml of 630 nm CdSe/ZnS QDs with oleic acid ligands were mixed into 1 gram of 10:1 PDMS. 200 mg of the CQD/PDMS mixture was drop cast onto a microscope slide and spin coated at 6000 rpm for 30s, the results of this test can be seen in Fig. 6-8. The diameter of the CQDs were 11 nm. Due to high concentration, clustering of CQDs into sphere-like formations following solvent evaporation occurred. The CQDs formed into a supraparticle structure within the PDMS. The high concentration of CQDs and high spin speed make this sample and method unsuitable

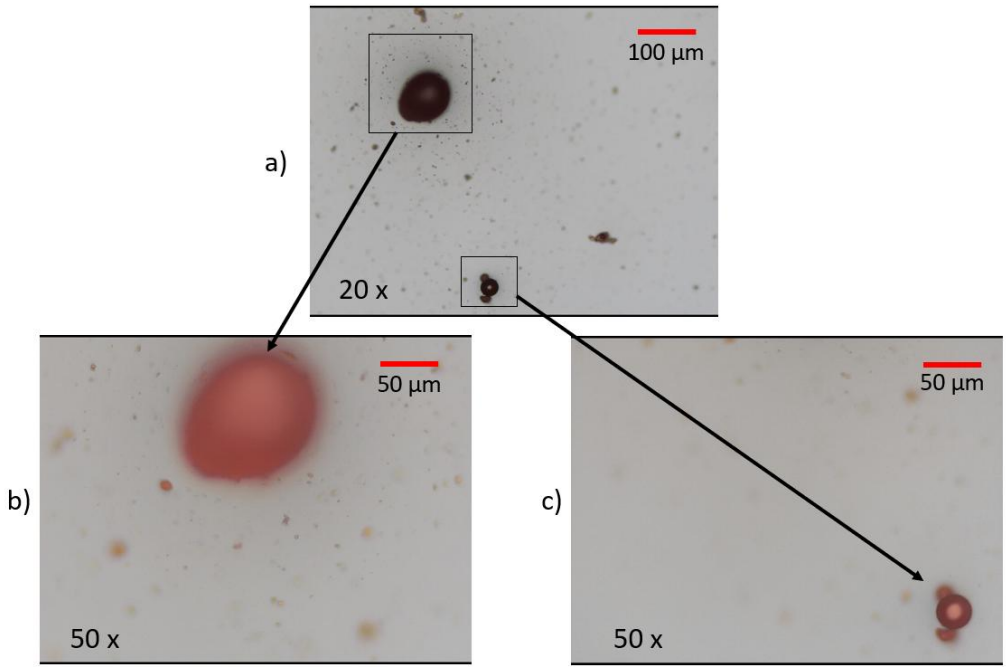

Fig. 6-8 microscope images of CQD/PDMS spin coated films. The quantum dots used were 630 nm CQD solution from Cytodiagnostics. Image a) is the film at 20 x magnification, b) and c) are enlarged images of the microspheres seen in image a) with arrows indicating which sphere.

for single photon emission as there is a higher probability of clustering the quantum dot material together and less chance of isolation of a single CQD.

6.8.1.3 Nanodiamond Composite Samples

Nitrogen Vacancy centre nanodiamonds with an average size of 40 nm,(sourced from Adamas Nanotechnologies) were used to determine if detection of single photon emission was possible using the micro-PL set up described in section 6.8.2. Diluting the stock nanodiamond solution to a concentration of 0.01 mg/ml, then adding 15 µL of this to 15 µL of 0.3% (w/v) PVA solution and sonicated for 30 minutes. Following this the solution was spin coated at 3000 rpm for 30 s onto a standard coverslip and left to dry before characterising.

6.8.1.4 Composite Samples fabricated Fraunhofer IMM solution.

Using the CQD solution from batch 3 prepared by IMM a test sample was spin coated. The solution was incorporated into PDMS polymer and then spin coated onto a coverslip to create a thin film. A microscope image of the films is shown in Fig. 6-9.

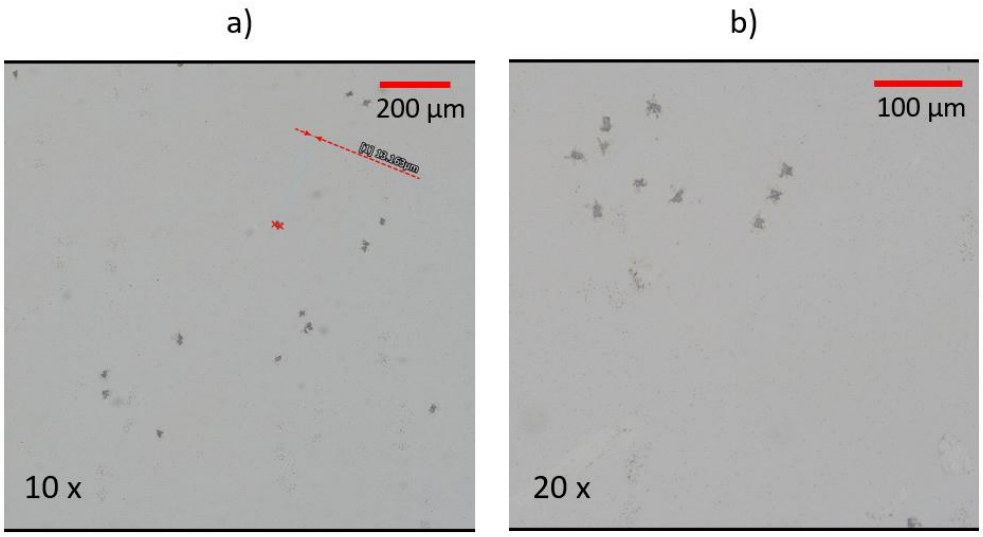

Fig. 6-9 Microscope Images of CQD/PDMS films containing Fraunhofer IMM solution (ML2020-09-F6_diluted). Image a) shows debris within film at 10 x mag, if individual quantum dots were incorporated into the film, they would be hard to image due to their size. b) shows the same film at higher magnification.

10 µL of CQD solution was mixed into 1000 mg of 10:1 ratio PDMS. 200 µL of the mixture was then drop cast onto the cover slip and spin coated at 2000 rpm for 30 seconds. From the images taken using the microscope it is difficult to determine the presence of the CQDs within the sample as the resolution of the microscope is not able to resolve particles that small. The black dots seen are most likely large clusters of debris. As there is no clustering present within these samples PL mapping and HBT measurements using the confocal micro-PL were performed on these samples as the have a higher probability of containing an isolated CQD which could be suitable for single photon emission. The results of PL mapping and HBT measurements shown in section 6.9.

6.8.2 Micro-PL Experimental Set-up

To measure and determine if the samples contain single emitters, modifications to an established micro – PL system outlined in [145], were made. These modifications made the micro-PL into a confocal system. In a confocal set up, light is collected from a sample and spatially filtered using a confocal aperture, in this case a pinhole. Using a pinhole means that only photons from a single spot in a sample will reach the detector. This can allow for better image contrast and depth resolution since the pinhole eliminates out of focus photons and stray light, making the detection of single

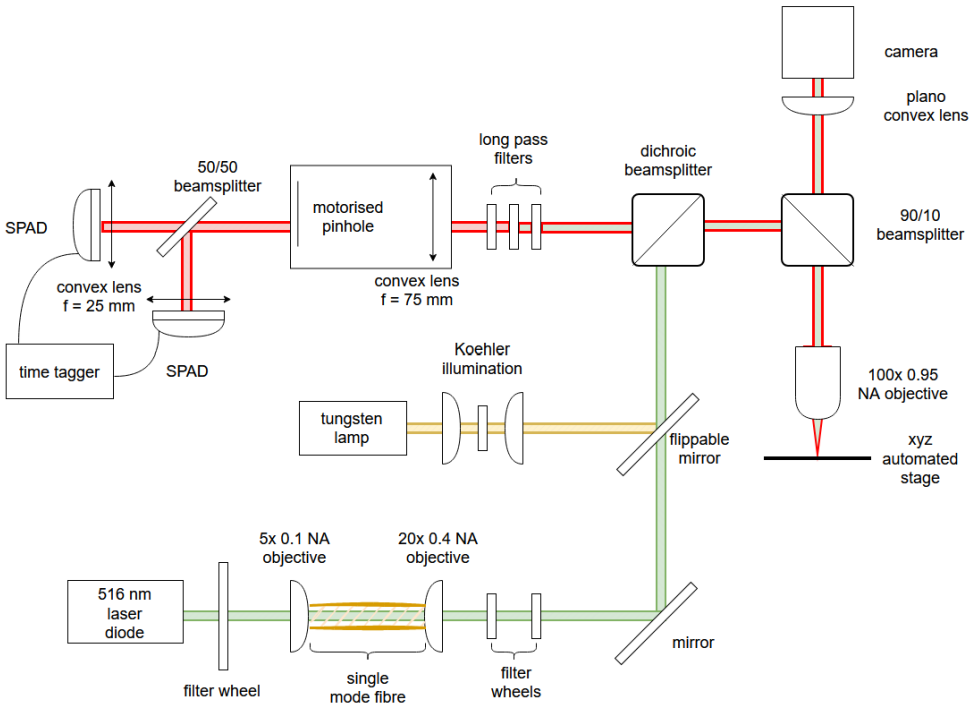

Fig. 6-10 Schematic of micro-PL experimental set up.

photons easier. The system also required the integration of additional optics and single photon detectors to perform HBT measurements necessary to determine if single photon emission has occurred. The system allows the ability to optically pump micro and nano sized objects while collecting the emissions through fibre-coupled single photo avalanche diode (SPAD) photodetectors and intensity maps through a high-resolution (CMOS) camera. Interchangeable optical objective lenses allow for larger area and more localised scans, which range from x5 to x100 magnification. Additionally, high- accuracy computer-controlled translation stages were used for accurate x-y-z location of emitters areas.

This set-up, as seen in Fig. 6-10 makes use of a continuous wave (CW), 516 nm laser which is initially attenuated using a filter wheel and then focussed using a 5x objective lens into a single mode fibre. The output from the fibre is then collimated using a 20x microscope objective and the intensity is attenuated further by 2 sets of attenuator wheels with a wide range of neutral density filters. A beam splitter is used to split the incoming pump light into two directions, one directed towards the sample and camera pathway, and the other towards the SPADs. Following the pathway, which is split towards the camera and sample stage, a second beam splitter is used to send

90% of the light towards the sample, while the remaining 10% is directed towards the camera. An objective lens (100×/0.95 NA) is used to focus the pump light onto the sample. At the focus of the sample plane, the beam spot size 0.41 microns. The beam spot was measured using the 100x objective. An image of the focussed beam was taken using the camera. An x-y scan through the origin of the beam spot was taken to give the relative pixels size across the beam. The pixel size was calculated using the magnification of the 125 mm lens and then compared to the given pixel size of the camera from the data sheet. Samples are placed on a motorised x-y-z stage (SmarAct) that gives micron precision control of their positioning. The light emitted by the sample is collected by the same objective and is focused onto the camera using a plano convex lens with a focal length of 125 mm. Following the arm of the setup up towards the two SPAD detectors, the light emitted from the sample is passed back through the beam splitters and is filtered using three long pass filters to cut as much of the excitation light as possible. These are used to block 516 nm pump light, letting through only the luminescence emitted from the sample. Each time the setup is initialized the 40 µm pinhole is aligned. The pinhole ensures that as much excess background light as possible is rejected before reaching the SPAD detectors to improve the signal to noise ratio. A tungsten lamp has also been integrated into the system so that features on the samples can be visualised using the camera by inserting a flip up mirror. The laser output power can be checked and calibrated using a flip in mirror before light enters the confocal microscopy set up before each measurement is carried out.

6.8.3 Confocal Intensity Maps and HBT scanning

For the confocal PL intensity maps and HBT measurements to be carried out the pinhole alignment needed to be carried out first. At a low laser power, a time trace is used to maximise the counts/s of one SPAD. The pinhole position is adjusted horizontally and vertically to optimise the counts on time trace. Following this an x-z laser confocal scan is carried out to determine if the focus of the laser on the sample correlates to the maximum counts registered by the SPAD. If the values agree, the 3 filters after the beam splitter are inserted to engage “PL mode” so that the confocal

intensity maps and HBT measurements can be performed. The sample is scanned in the x-y direction to map the position of the nanoparticle emitters. The stage moves the sample beneath the laser beam in micron steps while images are captured using the camera that are later stitched together using a python code to give an x-y PL map. As the images are being captured one of the SPADs measures the counts/s it receives at each point of the scan and the code correlates that with the PL map to give an indication where the possible emitters are located. Using the larger x-y map, a smaller map can be taken at any position of interest, as well as an HBT measurement.

The HBT scan is performed using 2 SPADs and the temporal delay between the detection events is measured using a time tagger (Swabian Instruments, Time Tagger 20), to count the incoming photons from the excited emitters in the sample. The output is then given as the correlated $g^2(0)$ value against the time delay of the signals between the 2 SPADs and synchronised with sample position using a Python-based GUI.

6.9 Results

6.9.1 Film Characterisation

6.9.1.1 IMM solution results

A confocal photoluminescence intensity map is shown in Fig. 6-11 a). The numerous bright spots in the image represent regions with higher pixel intensity, likely indicating the presence of quantum dots (QDs). The map is shown in a false colour profile and bears no relation to the emission wavelength of the quantum dots. The inset image depicts an enlarged view of the selected emitter used for the HBT measurements, showing an approximate count rate of 60 kcounts/s. The results of the HBT measurement are shown in Fig. 6-11 b). The peak at 0 ns indicates that there is likely multiphoton emission and bunching of several photons at the detectors due to the simultaneous emission of several QD emitters due to the high density in the sample. The presence of peaks in the HBT measurements at 25 ns are thought to be after pulsing [146] from the Excelitas detectors that were initially installed into the micro-PL system used to obtain these initial measurements. Following this, the SPADs

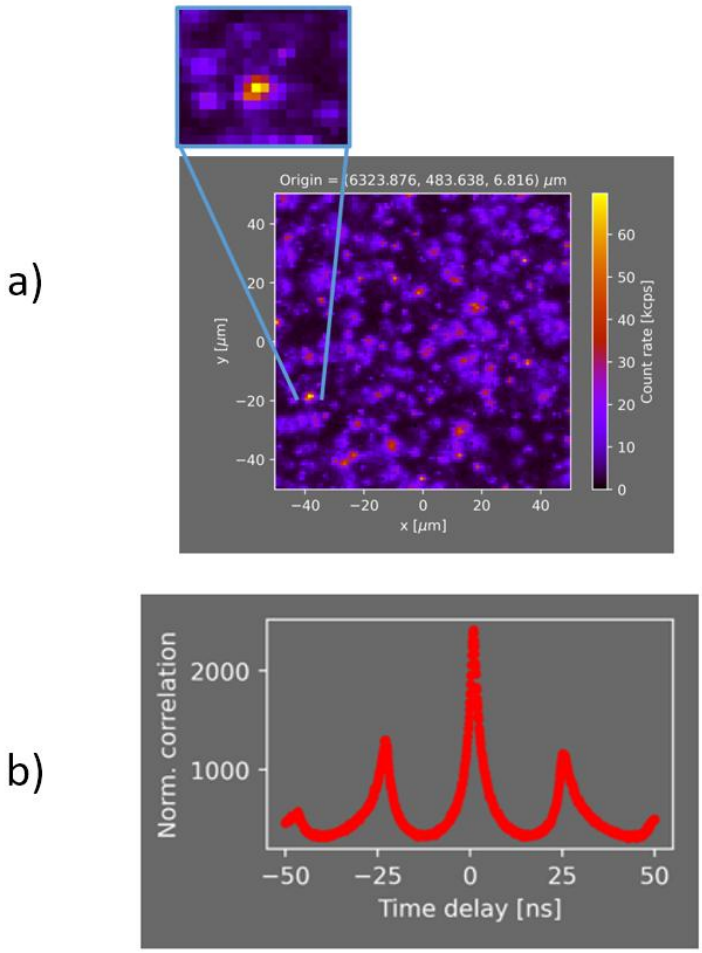

Fig. 6-11 a) Confocal Photoluminescent Map of a broad area scan of a sample contatining IMM quantum rods. Inset is a larger view of a bright spot of detected luminescence b) Corresponding HBT results for the emitter highlighted in a). The results show evidence of photon bunching, indicating the occurrence of multiphoton emission and more that one quantum emitter at that location.

were swapped for different models (IDQ detectors) and this phenomenon was eliminated.

With regards to the emitter density of the sample, it has been reported in [124], [140] that single quantum emitters should be isolated from each other with distances larger than the emission wavelength, which in this case would be greater than 630 nm. For the sample shown in Fig. 6-11 a). the emitter density is higher and are in closer proximity to one another than that. For a higher chance of a successful HBT measurement outcome, the concentration of quantum dots should be reduced, aiming for a lower overall density. A QD density of 0.1 dot/μm^2 in film [33], [140] was reported as being an ideal density of QDs on a spin coated sample.

6.9.1.2 Nanodiamond Results

Fig. 6-12 shows the HBT results for two different emitters from an x-y intensity map scan of the nanodiamond sample. Areas of brighter intensity from the larger PL map were targeted to determine if the higher intensity areas contained single emitters. Each sample had several locations scanned and at different time delays with different excitation power, the best results are shown.Both a) and c) show images of the targeted emitters that were used for HBT measurements shown in b) and d). The displayed data is centred around the 0 point, where antibunching is expected, by focusing on a 100 ns interval, even though each scan covers a total time of 300 ns. This approach provides a clearer view of the phenomenon. Fig. 6-12 c) shows the HBT results for the emitter highlighted by the red circle in a) at an excitation power of 100 µW. The emitter gave a count rate of approximated 40 x10^3 counts/sec on the x-y

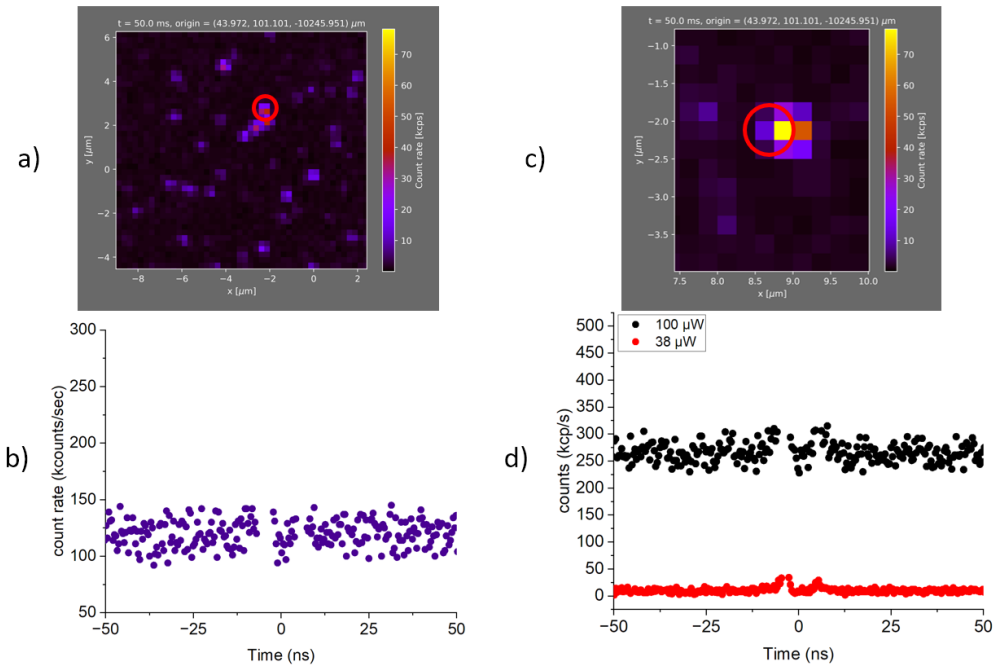

Fig. 6-12 a) image of the confocal PL map taken for an area of the sample. b) is the corresponding HBT results from an emitter with approximately 50 kcps/s with excitation power of 100 µW, indicated by the red circle c) a second confocal PL map from the same sample at a different location, d) the HBT results for the emitter which is indicated by the red circle given in c). the results show a comparison of HBT measurements from an emitter at different excitation powers, the red data shows the kcps/s for excitation at 38 µW while the black data shows the kcps/s for the same emitter excited at 100 µW. Neither result demonstrate antibunching to confirm the presence of a single photon emitter.

confocal scan. The HBT results in b) do not show any evidence of antibunching at this emitter. This emitter may be a cluster of aggregated nanodiamonds reducing the probability of detecting a single NV centre within the nanodiamond cluster. Fig. 6-12 d) shows the data from another emitter taken from the same sample at a different location with a higher approximate count rate of 70 x10^3 counts/sec, where two different excitation powers are compared. The black dots show an excitation power of 100 µW, while the red dots show an excitation power of 38 µW. Neither data set show the presence of single photon emission via the second order corelation function. Comparing the count rates of the 2 different excitation powers, when the excitation power increases the noise floor is also increased. This increase in noise floor could make detection of antibunching more difficult to determine accurately, so care must be taken when exciting the emitters.

Fig. 6-13 a), shows a "broad" area scan of 30 x 30 µm of a region of a nanodiamond sample. The brighter areas of luminescence are indicated by the yellow spots on the

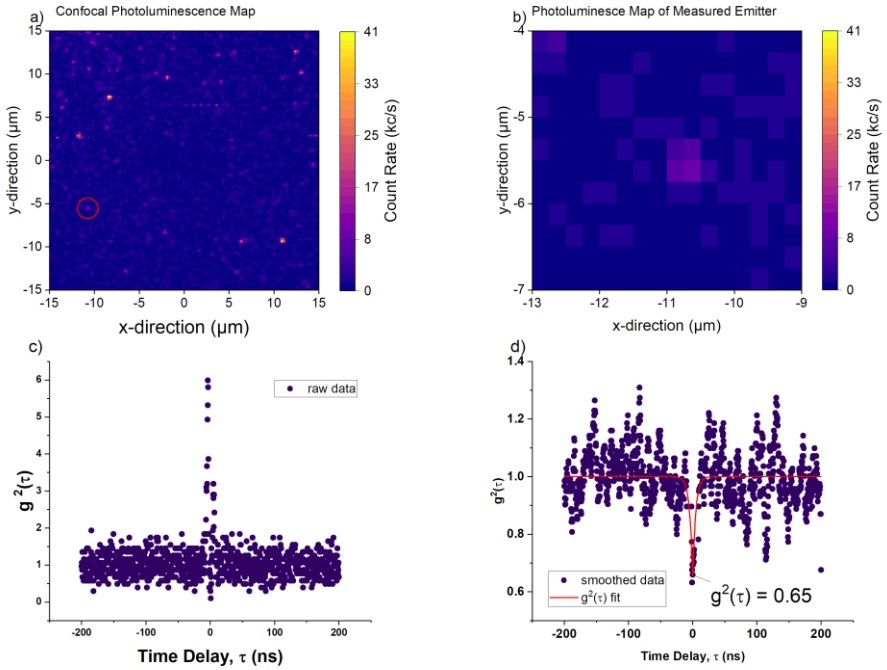

Fig. 6-13 a) Photoluminescent intensity map of large area (30 x 30 µm) confocal microscope scan, b) enlarged image of emitter highlighted in image a). The count rate for this emitter is approximately 15 k counts/s when pumped with an excitation power of 95 µW. c) shows the raw data for the HBT measurement d) corresponding processed HBT results for emitter shown in a). The red line indicates the second order correlation fit giving a $g^2(\tau)$ value of 0.65.

PL map and have a count rate of approximately 41 kc/s. As the brighter areas of luminescence are suspected to be clusters of nanodiamond material that have aggregated that will demonstrate “bunching”, an emitter with a lower count rate is chosen for HBT measurements. The chosen emitter is highlighted in Fig. 6-13 a) by a red circle, with an enlarged image of the same emitter shown in Fig. 6-13 b). This emitter has a count rate of approximately 15 kc/s when pumped at 95 µW. The resultant raw data is shown Fig. 6-13 c) and the processed HBT data is shown in Fig. 6-13 d).The graph shows some lower correlated count rates at a time delay of 0 ns. This could indicate a single NV centre on the nanodiamond was excited and some antibunching occurred since some of the correlated counts have a value below 0.5 at zero delay. The $g^2(\tau)$ fit shows a value of 0.65 while this is not below 0.5 strongly indicating occurrence of single photon emission from the emitter, it does indicate antibunching as the value is between 1 and 0. Current research has demonstrated single photon emission with values of 0.1 [34] indicating it is possible to achieve single photon emission with this nanodiamond material. A challenge lies in the significantly high signal-to-noise ratio for this system and as a result, lower $g^2(\tau)$ values become increasingly challenging as is is possible single photo emission from the source occurred but with multi photon contamination from other sources.

6.10 Discussion

Although single photon emission has not been clearly demonstrated with these thin film samples, a photoluminescence map showing where emitters are in a sample location has been achieved. Within the timing of the Qudos project, the materials used, and set-up could not be improved further to show better HBT results. As seen in Fig. 6-13 the nanodiamond material was the closest to yielding positive results, however the signal to noise ratio and the optical cross talk from the SPADs would need to be greatly reduced for this to be confidently demonstratable. Something as simple as swapping the SPAD detectors for a different model may have a significant impact on the signal to noise ratio. Installation of a pulsed laser source as the excitation source for the emitters over a CW could also be a way to improve the HBT measurements as it would help to improve the signal to noise ratio from the

detectors. Furthermore, it should be noted the density of quantum dots in the sample shown in Fig. 6-11 was higher when compared to the nanodiamond samples shown in Fig. 6-13 and Fig. 6-13, which could be an explanation for the nanodiamond results being closer to yielding single photon emission results. To confirm that the luminescence captured with the camera is from a quantum emitter, photoluminescence measurements using a spectrometer would be beneficial, this could help to give an idea that emitters with a lower count rate are the desired material rather than unwanted dust or debris on the sample. Scanning electron microscope images of the samples would be another way to verify the presence of nanodiamond or quantum dot emitters in the spin coated samples which could be of benefit in determining the location of the emitters so that the precise location could be find using the micron scale capabilities of the xyz translational stage.

6.11 Summary

In this chapter we have prepared a method for generating a film of quantum dots/nanodiamonds with a method to disperse the nanomaterial. Analysis of quantum dots supplied by Fraunhofer IMM, was also performed. Establishing and optimising a micro-PL system to perform HBT measurements that allowed subsequent measurements of a series of samples containing QDs and nanodiamonds to explore thin films as a source for a deterministic single photon source. Although the materials used have been established in previous works as single photon sources, it was not possible to demonstrate within the time frame given for this project, however a fundamental basis for this kind of research has been established at FhCAP and the IoP where future works and projects could continue the refinement of the HBT system which has already been established, as well as the protocols used for sample fabrication.

Chapter 7

7 Conclusions

This thesis has concentrated on the exploration of a combination µLEDs with CQD materials to create hybrid bioinstrumentation with a view to advance POC diagnostics, progression of the development and understanding of elastomeric colour converters and to assess the potential for these materials as a single photon source in the visible spectrum.

A novel compact optical biosensor was developed to qualitatively detect the presence of an analyte using protein conjugated colloidal quantum dots demonstrating their detection with a smartphone. Further work explores adding additional capabilities to the device which could be used to improve detection such as multiplexing and the use of a novel conjugated SP to enhance the limit of detection. Examining the impact of temperature treatment on the photoluminescent properties of quantum dots (QDs) within a PDMS matrix, when combined, to determine their protective effects has also been investigated within this work. A functional operating temperature which includes CQD colour converters has been outlined.

Finally, CQDs and nanodiamonds within polymer thin film samples have been used to explore their potential as a single photon source. Although the achievement of single

photon emission was not demonstrated in these samples, strides toward this goal have been achieved. This thesis includes the demonstration of protocols for a spin coating procedure for the thin film samples as well as the successful implementation of upgrades to the micro-PL system necessary for characterising these samples.

This final chapter outlines the results and the conclusions drawn from all the experimental work within this thesis, and then discuss future work that could be developed from these platforms.

7.1 Summary of results

Chapter 2 introduced materials, devices and principles which were a common thread throughout. Since the subjects examined within this portfolio varied across different categories and research domains, each relevant chapter included an introduction to the current state-of-the-art devices pertaining to the respective topic.

Chapter 3 centred around a proof-of-concept fluorescent biosensor that employed a µLED to inject light into a glass microscope slide, serving as an evanescent waveguide platform. The biosensors concept and design were presented with attention being given to the µLED geometry, quantum dot tags and smartphone detector. This setup demonstrated the potential for smartphone detection, making it a versatile and practical tool for fluorescent biosensing. The purpose of using µLEDs was to enable efficient light coupling without any additional optics, allowing for future iterations of the device to battery operated The unusual µLED design and integration of detection without optics with potential for battery operation gives this form factor a novelty and great potential for further development of a compact point of care diagnostic device.

The main findings in this chapter outline that the RGB response of the camera sensor can discriminate between the fluorescence and excitation light when the µLED emission light and the QD emission wavelengths are chosen with a suitable separation. Demonstration of simple data collection in the form of JPEG images can be used for analysis. Following data collection, it was determined that the device with smartphone detection has a detection limit of 8 nM for streptavidin-conjugated

quantum dots, with an exposure time of 250 ms. The other results of this chapter explore the parameters which could be used to improve this limit of detection such as driving current of the μLED and exposure time when capturing images. By demonstrating that functionalized amine ligand QDs can be detected using a smartphone it provides a promising basis for the platform to be used as a compact biosensor for POC.

Building on the work in chapter 3, the platforms capability to distinguish multiple wavelengths of quantum dot tags in situ on a single chip is explored in chapter 4. Additionally, the utilization of SPs as an alternative fluorescent tag is investigated. The most effective approach to distinguish between multiple wavelengths of SA-QDs in situ on the chip was by utilizing an intensity ratio profile, where each wavelength would give intensity readings in a particular ratio in the R, G, B channels. Moreover, the smartphone-based detection system also allowed for imaging of the SPs. By comparing intensity levels before and after UV irradiation following functionalisation, a successful photocleaving process was demonstrated through variations in light intensity levels. This demonstrates that SPs would be an alternative to CQDs with the added possibility of reusing the SPs following photocleaving.

Chapter 5 focused on isolating the impact of heat on the stability of the PL properties of a CQD encapsulated in an elastomeric polymer. Different concentrations of CQDs were incorporated into a polymer mixture, and the results were compared to examine the effects of various temperatures and durations of heat exposure on the photoluminescent output.

The findings revealed that embedding CQDs in a composite material provided a protective effect, preserving the optical properties of the CQDs, particularly irradiance, compared to an unprotected neat film. An upper operating temperature limit of 150°C was identified, above this temperature detrimental effects on the PL output of CQDs would occur. Importantly, these results remained unaffected by other oxygen-related phenomena like photooxidation.

It was also observed that the damage to CQD PL output intensified with the duration of heat exposure. Overall, the insights presented in this chapter are valuable for determining the operational conditions and tolerance levels necessary for integrating mechanically flexible colour converters into practical devices and systems, such as solid-state lighting or displays.

The final results chapter introduces the concept behind a device designed for a deterministic single photon source. The novelconcept and design of this compact device is outlined in this chapter, describing how a device using a µLED could be used to excite a single quantum dot after it has been transfer printed onto a collection fibre while at room temperature The micro-PL experimental set up is described in detail, and an early demonstration of a protocol for spin coating QDs and NV-NDs is described. The results show that intensity mapping and HBT measurements with the micro-PL system using thin film samples has been demonstrated. Using the accurate x-y-z translation stage locations of potential emitters can be recorded and HBT measurements performed at these precise locations. Current research indicates a purity value of 0.1 for room temperature single photon emission of nanodiamond, we have demonstrated a $g^2(\tau)$ value of 0.65 from the ND samples indicating antibunching, however as time ran out for further investigation of these samples single photon emission could not be definitively shown with the CQDs or NDs.

7.2 Summary of Key achievements

- Established smartphone can used in conjunction with µLED excitation source to create a compact biosensor.
- Establish a detection limit of 8nM using SA-QD tags for the presence of the analyte biotin.
- Exploration of alternative tags for use on the evanescent platform showed that microspheres could be a potential alternative.

- Multiple wavelengths of SA-QDs can be distinguished on one sensor chip allowing for further investigations of multiplexing the biosensor chips to detect more than one analyte at a time.
- PDMS polymer can have a protective effect on damage to optical properties of QDs against heat.
- An upper limit of 150 ˚C on the operating temperature of elastomeric devices containing QDs was established before irreversible damage on optical properties on the QDs occurred. This provides a tolerance for heat range when incorporating elastomeric QDs into devices.
- Protocols for thin film single photon sources for further investigation into room temperature deterministic sources
- Demonstration of antibunching with ND samples with a $g^2(\tau)$ value of 0.65

7.3 Future Work

Overall, the research conducted in this thesis has resulted in important progress towards the integration of hybrid elastomeric quantum dot films into devices, there are still many more avenues for improvement that could be explored. The remaining section of this thesis will highlight areas of research which could be used for device improvement in each case.

7.3.1 Compact biosensor platform

Improving performance of the biosensor device outlined in chapters 3 and 4 could come from several different areas. Enhancing the detection sensitivity in line with other available POC diagnostics could be one main area of focus. One approach that could be focussed on is the spectral calibration for the RGB sensor in the smartphone that would enable more accurate and reliable results.

Since the device serves as a proof-of-concept, it is essential to demonstrate the detection of various analytes to showcase true multiplexing capabilities. Exploring different analytes for this purpose would be beneficial.

To progress from a bench-top lab set up to a functional device and user-friendly device, the development of an app or software programme which can be added to the smartphone software should be considered. This will allow for automatic image processing within the device and reduce the need for specialised operation and to meet the criteria for a POC diagnostic.

As only one model of smartphone is used for measurements, performing the data acquisition across multiple different smartphone devices would allow for direct comparison of the difference between smartphone sensors available and the effect of this on the detection limit. This would also provide insightful information for the spectral calibration required.

A significant step towards achieving a functional point-of-care device is to minimize the device footprint and make it portable by incorporating battery operation. Investigating the best method for implementing this feature is crucial.

Considering an alternative wavelength for the excitation source of the biosensor is another promising avenue. Using a UV µLED will enable excitation of more wavelengths of QDs at once, allowing for better multiplexing capabilities. Using a UV µLED would require the design and testing of a novel µLED device with a similar geometric design to the previously outlined setup. This would ensure a similar filling of the glass microscope slide and maintain similar coupling efficiencies.

Improvements can also be explored by customizing the glass used in the biosensor device. Flexibility should be taken into consideration to enhance the device's performance and adaptability.

7.3.1 Supraparticle materials.

Enhancing SP fabrication could lead to significant improvements in the quality of emission when used as fluorescent tags, as nanoparticles and SPs may be affected by self-absorption. By improving the synthesis and photoluminescent properties of the SPs, their detection capabilities at lower concentrations can be greatly improved, resulting in better limits of detection.

One objective of this project outlined in chapter 4 is to determine if microspheres can be effectively used as functionalized tags and detected by the smartphone biosensor platform. As this has now been established, further work is required to set a specific limit of detection using this material.

As the SPs are functionalised with photocleavable streptavidin ligands and biotin is a well-established way to attach different analytes through biotinylating, the process could be streamlined by using a photocleavable biotin ligand.

Due to the toxic nature of the CdSe materials used to create the SPs, less toxic materials such as indium phosphide (InP) should be explored as an alternative material. This substitution would render the SP tags more suitable for a broader range of applications, including biological applications such as in vivo testing.

7.3.2 Qudos Project

In many existing systems demonstrating single photon emission, a pulsed laser has been used as the excitation source. However, the current experimental setup described in chapter 6 only utilizes a continuous wave source. Introducing a pulsed laser as an excitation source could lead to easier and more reliable demonstration of single photon emission from quantum dots. This is because the pulsed laser is less likely to cause quenching of the quantum dot material, which can irreversibly lead to a loss of photoluminescence and render the nanoparticle unsuitable for its intended purpose. By using a pulsed laser, repeatability, and reliability of results with quantum dot materials can be enhanced.

Another area for further research to improve the system is to enhance the signal-to-noise ratio. This can be achieved, for instance, by using better detectors that are less prone to optical crosstalk, which has been observed in SPAD (single-photon avalanche diode) array systems in the past.

Once improvements are made to the overall system, the next step would be to work on reducing the benchtop footprint. This would involve developing a more compact device for the project, making it more practical and convenient for various applications.

7.4 Overall Conclusion

All works established in this thesis focussed on the overarching theme of combining quantum emitters like CQDs with GaN LED photopumping for applications in fields like medicine and biophotonics, solid-state lighting and related, and quantum technologies. Different aspects, presented as a portfolio of projects, were reported. This has proven beneficial in several ways, as it facilitated the seamless integration of quantum dots into different devices for diverse applications. Moreover, this approach demonstrated protective effects on the photoluminescent properties of the quantum dots, ensuring their stability and functionality within the elastomeric matrix. These findings open new possibilities for utilizing quantum dots in a wide range of applications, while also ensuring their long-term effectiveness and performance. One significant finding in this thesis established that a smartphone is a capable device for the detection of different types of nanoparticles. These findings provide an opportunity to integrate and miniaturise a detection and data analysis processes more readily for POC diagnostics. Using smartphones as a detection tool for bioparticles could provide an easily accessible tool for researchers and the public to continue to improve health outcomes in primary care and environmental settings.

References

[1] ‘The Nobel Prize in Physics 2014: Blue LEDs - filling the world with new light’. [Online]. Available: https://www.kva.se/en/news/nobelpriset-i-fysik-2014-2/. [Accessed: 11-Dec-2023].

[2] ‘The Nobel Prize in Chemistry 2023: They planted an important seed for nanotechnology’. [Online]. Available: https://www.kva.se/en/news/the-nobel-prize-in-chemistry-2023/. [Accessed: 11-Dec-2023].

[3] E. F. Schubert, *Light Emitting Diodes*, 2nd Editio. Cambrigde University Press, 2006.

[4] S. Nakamura and M. R. Krames, ‘History of gallium-nitride-based light-emitting diodes for illumination’, *Proc. IEEE*, vol. 101, no. 10, pp. 2211–2220, 2013.

[5] G. Li *et al.*, ‘GaN-based light-emitting diodes on various substrates: A critical review’, *Reports Prog. Phys.*, vol. 79, no. 5, 2016.

[6] H. S. Wasisto, J. D. Prades, J. Gülink, and A. Waag, ‘Beyond solid-state lighting: Miniaturization, hybrid integration, and applications of GaN nano-and micro-LEDs’, *Appl. Phys. Rev.*, vol. 6, no. 4, 2019.

[7] K. Behrman and I. Kymissis, ‘Micro light-emitting diodes’, *Nat. Electron.*, vol. 5, no. 9, pp. 564–573, 2022.

[8] P. J. Parbrook, B. Corbett, J. Han, T. Y. Seong, and H. Amano, ‘Micro-Light Emitting Diode: From Chips to Applications’, *Laser Photonics Rev.*, vol. 15, no. 5, pp. 1–18, 2021.

[9] Z. Chen, S. Yan, and C. Danesh, ‘MicroLED technologies and applications: Characteristics, fabrication, progress, and challenges’, *J. Phys. D. Appl. Phys.*, vol. 54, no. 12, 2021.

[10] K. Ding, V. Avrutin, N. Izyumskaya, Ü. Özgür, and H. Morkoç, ‘Micro-LEDs, a manufacturability perspective’, *Appl. Sci.*, vol. 9, no. 6, 2019.

[11] T. Wu *et al.*, ‘Mini-LED and Micro-LED: Promising candidates for the next generation display technology’, *Appl. Sci.*, vol. 8, no. 9, 2018.

[12] F. Rahman, ‘Zinc oxide light-emitting diodes: a review’, *Opt. Eng.*, vol. 58, no. 01, p. 1, 2019.

[13] R. C. Sharma, R. Nandal, N. Tanwar, R. Yadav, J. Bhardwaj, and A. Verma, ‘Gallium Arsenide and Gallium Nitride Semiconductors for Power and Optoelectronics Devices Applications’, *J. Phys. Conf. Ser.*, vol. 2426, no. 1, 2023.

[14] P. Tian *et al.*, ‘AlGaN Ultraviolet Micro-LEDs’, *IEEE J. Quantum Electron.*, vol. 58, no. 4, pp. 1–14, 2022.

[15] S. P. Denbaars, S. Nakamura, and J. S. Speck, ‘Gallium nitride based light emitting diodes (LEDs) for energy efficient lighting and displays’, *2013 Saudi Int. Electron. Commun. Photonics Conf. SIECPC 2013*, 2013.

[16] M. S. Kang, C. H. Lee, J. B. Park, H. Yoo, and G. C. Yi, ‘Gallium nitride nanostructures for light-emitting diode applications’, *Nano Energy*, vol. 1, no. 3, pp. 391–400, 2012.

[17] F. A. Ponce and D. P. Bour, ‘Nitride-based semiconductors for blue and green light-emitting devices’, *Nature*, vol. 386, no. 6623, pp. 351–359, Mar. 1997.

[18] E. Jang, S. Jun, H. Jang, J. Lim, B. Kim, and Y. Kim, ‘White-Light-Emitting Diodes with Quantum Dot Color Converters for Display Backlights’, *Adv. Mater.*, vol. 22, no. 28, pp. 3076–3080, May 2010.

[19] L. Yin, Y. Bai, J. Zhou, J. Cao, X. Sun, and J. Zhang, ‘The thermal stability performances of the color rendering index of white light emitting diodes with the red quantum dots encapsulation’, *Opt. Mater. (Amst).*, vol. 42, pp. 187–192, 2015.

[20] T. Frecker, D. Bailey, X. Arzeta-Ferrer, J. McBride, and S. J. Rosenthal, ‘Review—Quantum Dots and Their Application in Lighting, Displays, and Biology’, *ECS J. Solid State Sci. Technol.*, vol. 5, no. 1, pp. R3019–R3031, 2016.

[21] C. C. An, M. H. Wu, Y. W. Huang, T. H. Chen, C. H. Chao, and W. Y. Yeh, ‘Study on flip chip assembly of high density micro-LED array’, *Proc. Tech. Pap. - Int. Microsystems, Packag. Assem. Circuits Technol. Conf. IMPACT*, pp. 336–338, 2011.

[22] A. Nardelli, E. Deuschle, L. D. de Azevedo, J. L. N. Pessoa, and E. Ghisi, 'Assessment of Light Emitting Diodes technology for general lighting: A critical review', *Renew. Sustain. Energy Rev.*, vol. 75, no. July 2015, pp. 368–379, 2017.

[23] J. Lee *et al.*, 'Dry etching of GaN and related materials: Comparison of techniques', *IEEE J. Sel. Top. Quantum Electron.*, vol. 4, no. 3, pp. 557–562, 1998.

[24] H. Jiang, 'Nitride microLEDs and beyond - a decade progress review', *Opt. InfoBase Conf. Pap.*, vol. 21, no. May, pp. 475–484, 2012.

[25] D. Massoubre *et al.*, 'Micro-structured light emission from planar InGaN light-emitting diodes', *Semicond. Sci. Technol.*, vol. 29, no. 1, pp. 0–6, 2014.

[26] H. X. Zhang *et al.*, 'Individually-addressable flip-chip AlInGaN micropixelated light emitting diode arrays with high continuous and nanosecond output power', *Opt. Express*, vol. 16, no. 13, p. 9918, 2008.

[27] A. D. Griffiths, J. Herrnsdorf, J. J. D. McKendry, M. J. Strain, and M. D. Dawson, 'Gallium nitride micro-light-emitting diode structured light sources for multi-modal optical wireless communications systems', *Philos. Trans. R. Soc. A Math. Phys. Eng. Sci.*, vol. 378, no. 2169, 2020.

[28] G. B. Nair and S. J. Dhoble, 'A perspective perception on the applications of light-emitting diodes', *Luminescence*, vol. 30, no. 8, pp. 1167–1175, 2015.

[29] F. P. García de Arquer, D. V. Talapin, V. I. Klimov, Y. Arakawa, M. Bayer, and E. H. Sargent, 'Semiconductor quantum dots: Technological progress and future challenges', *Science*, vol. 373, no. 6555, 2021.

[30] A. M. Smith and S. Nie, 'Semiconductor Nanocrystals: Structure, Properties, and Band Gap Engineering', *Acc Chem Res.*, vol. 43, pp. 190–200, 2010.

[31] M. Liu, N. Yazdani, M. Yarema, M. Jansen, V. Wood, and E. H. Sargent, 'Colloidal quantum dot electronics', *Nat. Electron.*, vol. 4, no. 8, pp. 548–558, 2021.

[32] Y. Ye, X. Lin, and W. Fang, ‘Room-Temperature Single-Photon Sources Based on Colloidal Quantum Dots : A Review’, pp. 1–20, 2023.

[33] Y. S. Park, S. Guo, N. S. Makarov, and V. I. Klimov, ‘Room Temperature Single-Photon Emission from Individual Perovskite Quantum Dots’, *ACS Nano*, vol. 9, no. 10, pp. 10386–10393, 2015.

[34] B. Rodiek *et al.*, ‘Experimental realization of an absolute single-photon source based on a single nitrogen vacancy center in a nanodiamond’, *Optica*, vol. 4, no. 1, p. 71, 2017.

[35] D. Kushavah, P. K. Mohapatra, and P. Ghosh, ‘Reduced carrier trapping in CdSe/ZnS/CdSe heterostructure quantum dots inferred from temperature dependent spectral studies’, *Phys. E Low-Dimensional Syst. Nanostructures*, vol. 102, no. April, pp. 58–65, 2018.

[36] M. A. Boles, D. Ling, T. Hyeon, and D. V. Talapin, ‘The surface science of nanocrystals’, *Nat. Mater.*, vol. 15, no. 2, pp. 141–153, Feb. 2016.

[37] C. Carrillo-Carrión, S. Cárdenas, B. M. Simonet, and M. Valcárcel, ‘Quantum dots luminescence enhancement due to illumination with UV/Vis light’, *Chem. Commun.*, no. 35, pp. 5214–5226, 2009.

[38] J. Y. Kim, O. Voznyy, D. Zhitomirsky, and E. H. Sargent, ‘25th Anniversary Article: Colloidal Quantum Dot Materials and Devices: A Quarter-Century of Advances’, *Adv. Mater.*, vol. 25, no. 36, pp. 4986–5010, Sep. 2013.

[39] M. A. Cotta, ‘Quantum Dots and Their Applications: What Lies Ahead?’, *ACS Appl. Nano Mater.*, vol. 3, no. 6, pp. 4920–4924, 2020.

[40] J. Zhang *et al.*, ‘Colloidal Quantum Dots: Synthesis, Composition, Structure, and Emerging Optoelectronic Applications’, *Laser Photon. Rev.*, vol. 17, no. 3, p. 2200551, Mar. 2023.

[41] C. B. Murray, D. J. Norris, and M. G. Bawendi, ‘Synthesis and Characterization of Nearly Monodisperse CdE (E = S, Se, Te) Semiconductor Nanocrystallites’, *J. Am. Chem. Soc.*, vol. 115, no. 19, pp. 8706–8715, 1993.

[42] Y. Pu, F. Cai, D. Wang, J. X. Wang, and J. F. Chen, 'Colloidal Synthesis of Semiconductor Quantum Dots toward Large-Scale Production: A Review', *Ind. Eng. Chem. Res.*, vol. 57, no. 6, pp. 1790–1802, 2018.

[43] M. G. Lüdicke, J. Hildebrandt, C. Schindler, R. A. Sperling, and M. Maskos, 'Automated Quantum Dots Purification via Solid Phase Extraction', *Nanomaterials*, vol. 12, no. 12, 2022.

[44] A. V Shvidchenko *et al.*, 'Colloids of detonation nanodiamond particles for advanced applications', *Adv. Colloid Interface Sci.*, vol. 268, pp. 64–81, 2019.

[45] L. Basso, M. Cazzanelli, M. Orlandi, and A. Miotello, 'Nanodiamonds: Synthesis and application in sensing, catalysis, and the possible connection with some processes occurring in space', *Appl. Sci.*, vol. 10, no. 12, pp. 1–28, 2020.

[46] A. Boruah and B. K. Saikia, 'Synthesis, Characterization, Properties, and Novel Applications of Fluorescent Nanodiamonds', *J. Fluoresc.*, vol. 32, no. 3, pp. 863–885, 2022.

[47] V. N. Mochalin, O. Shenderova, D. Ho, and Y. Gogotsi, 'The properties and applications of nanodiamonds', *Nat. Nanotechnol.*, vol. 7, no. 1, pp. 11–23, 2012.

[48] Y. Wu and T. Weil, 'Recent Developments of Nanodiamond Quantum Sensors for Biological Applications', *Adv. Sci.*, vol. 9, no. 19, pp. 1–19, 2022.

[49] I. Aharonovich, S. Castelletto, D. A. Simpson, C. H. Su, A. D. Greentree, and S. Prawer, 'Diamond-based single-photon emitters', *Reports Prog. Phys.*, vol. 74, no. 7, 2011.

[50] M. W. Doherty, N. B. Manson, P. Delaney, F. Jelezko, J. Wrachtrup, and L. C. L. Hollenberg, 'The nitrogen-vacancy colour centre in diamond', *Phys. Rep.*, vol. 528, no. 1, pp. 1–45, 2013.

[51] C. E. Wieman, D. E. Pritchard, and D. J. Wineland, 'Atom cooling, trapping, and quantum manipulation', *Rev. Mod. Phys.*, vol. 71, no. SUPPL. 2, pp. 253–262, 1999.

[52] K. Okamoto, 'Planar Optical Waveguides', in *Fundamentals of Optical Waveguides*, Elsevier, 2022, pp. 13–65.

[53] S. Ramachandran, D. A. Cohen, A. P. Quist, and R. Lal, 'High performance, LED powered, waveguide based total internal reflection microscopy', *Sci. Rep.*, vol. 3, pp. 1–7, 2013.

[54] B. Agnarsson, S. Ingthorsson, T. Gudjonsson, and K. Leosson, 'Evanescent-wave fluorescence microscopy using symmetric planar waveguides', *Opt. Express*, vol. 17, no. 7, p. 5075, 2009.

[55] B. Agnarsson, A. B. Jonsdottir, N. B. Arnfinnsdottir, and K. Leosson, 'On-chip modulation of evanescent illumination and live-cell imaging with polymer waveguides', *Opt. Express*, vol. 19, no. 23, p. 22929, 2011.

[56] R. Diekmann *et al.*, 'Chip-based wide field-of-view nanoscopy', *Nat. Photonics*, vol. 11, no. 5, pp. 322–328, 2017.

[57] V. Dugas, A. Elaissari, and Y. Chevalier, 'Surface Sensitization Techniques and Recognition Receptors Immobilization on Biosensors and Microarrays', in *Recognition Receptors in Biosensors*, New York, NY: Springer New York, 2010, pp. 47–134.

[58] C. MacDonald, R. Morrow, A. S. Weiss, and M. M. M. Bilek, 'Covalent attachment of functional protein to polymer surfaces: A novel one-step dry process', *J. R. Soc. Interface*, vol. 5, no. 23, pp. 663–669, 2008.

[59] J. A. Howarter and J. P. Youngblood, 'Optimization of silica silanization by 3-aminopropyltriethoxysilane', *Langmuir*, vol. 22, no. 26, pp. 11142–11147, 2006.

[60] M. Szkop, B. Kliszcz, and A. A. Kasprzak, 'A simple and reproducible protocol of glass surface silanization for TIRF microscopy imaging', *Anal. Biochem.*, vol. 549, no. February, pp. 119–123, 2018.

[61] N. Bruce *et al.*, 'MicroLED biosensor with colloidal quantum dots and smartphone detection', *Biomed. Opt. Express*, vol. 14, no. 3, p. 1107, 2023.

[62] S. Vashist, 'Point-of-Care Diagnostics: Recent Advances and Trends', *Biosensors*, vol. 7, no. 4, p. 62, Dec. 2017.

[63] S. Kumar, M. Nehra, J. Mehta, N. Dilbaghi, G. Marrazza, and A. Kaushik, 'Point-of-Care Strategies for Detection of Waterborne

Pathogens', *Sensors*, vol. 19, no. 20, p. 4476, Oct. 2019.

[64] X. Weng, G. Gaur, and S. Neethirajan, 'Rapid Detection of Food Allergens by Microfluidics ELISA-Based Optical Sensor', *Biosensors*, vol. 6, no. 2, p. 24, Jun. 2016.

[65] M. Zarei, 'Portable biosensing devices for point-of-care diagnostics: Recent developments and applications', *TrAC - Trends Anal. Chem.*, vol. 91, pp. 26–41, 2017.

[66] V. Gubala, L. F. Harris, A. J. Ricco, M. X. Tan, and D. E. Williams, 'Point of care diagnostics: Status and future', *Anal. Chem.*, vol. 84, no. 2, pp. 487–515, 2012.

[67] S. Aydin, 'A short history, principles, and types of ELISA, and our laboratory experience with peptide/protein analyses using ELISA', *Peptides*, vol. 72, pp. 4–15, 2015.

[68] I. A. Darwish, 'Immunoassay Methods and their Applications in Pharmaceutical Analysis: Basic Methodology and Recent Advances.', *Int. J. Biomed. Sci.*, vol. 2, no. 3, pp. 217–35, 2006.

[69] Q. XIAO and J.-M. LIN, 'Advances and Applications of Chemiluminescence Immunoassay in Clinical Diagnosis and Foods Safety', *Chinese J. Anal. Chem.*, vol. 43, no. 6, pp. 929–938, Jun. 2015.

[70] C. WANG, J. WU, C. ZONG, J. XU, and H.-X. JU, 'Chemiluminescent Immunoassay and its Applications', *Chinese J. Anal. Chem.*, vol. 40, no. 1, pp. 3–10, Jan. 2012.

[71] A. Sharma *et al.*, 'Designed strategies for fluorescence-based biosensors for the detection of mycotoxins', *Toxins (Basel).*, vol. 10, no. 5, pp. 1–19, 2018.

[72] F. Farrell *et al.*, 'A wearable phototherapy device utilizing micro-LEDs', in *Proceedings of the Annual International Conference of the IEEE Engineering in Medicine and Biology Society, EMBS*, 2019, no. c, pp. 67–70.

[73] F. A. Farrell, 'Design of a wearable LED-based phototherapy device', University of Strathclyde, 2021.

[74] F. Farrell, E. Xie, B. Guilhabert, A. M. Haughey, M. D. Dawson, and N. Laurand, 'Micro-LED Waveguide for Fluorescence Applications',

2019 IEEE Photonics Conf. IPC 2019 - Proc., pp. 2–3, 2019.

[75] S. Tominaga, S. Nishi, and R. Ohtera, 'Measurement and estimation of spectral sensitivity functions for mobile phone cameras', *Sensors*, vol. 21, no. 15, 2021.

[76] A. Roda, E. Michelini, M. Zangheri, M. Di Fusco, D. Calabria, and P. Simoni, 'Smartphone-based biosensors: A critical review and perspectives', *TrAC - Trends Anal. Chem.*, vol. 79, pp. 317–325, 2016.

[77] S. K. Vashist, O. Mudanyali, E. M. Schneider, R. Zengerle, and A. Ozcan, 'Cellphone-based devices for bioanalytical sciences Multiplex Platforms in Diagnostics and Bioanalytics', *Anal. Bioanal. Chem.*, vol. 406, no. 14, pp. 3263–3277, 2014.

[78] E. Petryayeva and W. R. Algar, 'A job for quantum dots: Use of a smartphone and 3D-printed accessory for all-in-one excitation and imaging of photoluminescence', *Anal. Bioanal. Chem.*, vol. 408, no. 11, pp. 2913–2925, 2016.

[79] E. Petryayeva and W. R. Algar, 'Multiplexed homogeneous assays of proteolytic activity using a smartphone and quantum dots', *Anal. Chem.*, vol. 86, no. 6, pp. 3195–3202, 2014.

[80] J. Herrnsdorf *et al.*, 'Micro-LED pumped polymer laser: A discussion of future pump sources for organic lasers', *Laser Photonics Rev.*, vol. 7, no. 6, pp. 1065–1078, Nov. 2013.

[81] K. E. Sapsford, 'Total-Internal-Reflection Platforms for Chemical and Biological Sensing Applications', M. Zourob and A. Lakhtakia, Eds. Berlin, Heidelberg: Springer Berlin Heidelberg, 2010, pp. 3–20.

[82] C. R. Taitt, G. P. Anderson, and F. S. Ligler, 'Evanescent wave fluorescence biosensors: Advances of the last decade', *Biosens. Bioelectron.*, vol. 76, pp. 103–112, Feb. 2016.

[83] R. Peltomaa, B. Glahn-Martínez, E. Benito-Peña, and M. Moreno-Bondi, 'Optical Biosensors for Label-Free Detection of Small Molecules', *Sensors*, vol. 18, no. 12, p. 4126, Nov. 2018.

[84] Y. Li and H. Zhang, 'Binding of streptavidin to surface-attached biotin with different spacer thicknesses', *J. Wuhan Univ. Technol.*

Mater. Sci. Ed., vol. 30, no. 6, pp. 1304–1309, 2015.

[85] T. Lakshmipriya, S. C. B. Gopinath, and T. H. Tang, 'Biotin-streptavidin competition mediates sensitive detection of biomolecules in enzyme linked immunosorbent assay', *PLoS One*, vol. 11, no. 3, pp. 16–20, 2016.

[86] I. L. Medintz, H. T. Uyeda, E. R. Goldman, and H. Mattoussi, 'Quantum dot bioconjugates for imaging, labelling and sensing', *Nat. Mater.*, vol. 4, no. 6, pp. 435–446, 2005.

[87] 'Thermo Fisher Scientific', 2023. [Online]. Available: https://www.thermofisher.com/order/catalog/product/Q10123MP. [Accessed: 29-Oct-2023].

[88] X. C. Tong, 'Characterization Methodologies of Optical Waveguides', in *Advanced Materials for Integrated Optical Waveguides*, vol. 46, Cham: Springer International Publishing, 2014, pp. 53–102.

[89] R. Radha, S. K. Shahzadi, and M. H. Al-Sayah, 'Fluorescent immunoassays for detection and quantification of cardiac troponin i: A short review', *Molecules*, vol. 26, no. 16, 2021.

[90] J. Zhou, Y. Liu, J. Tang, and W. Tang, 'Surface ligands engineering of semiconductor quantum dots for chemosensory and biological applications', *Mater. Today*, vol. 20, no. 7, pp. 360–376, 2017.

[91] G. Jarockyte, V. Karabanovas, R. Rotomskis, and A. Mobasheri, 'Multiplexed nanobiosensors: Current trends in early diagnostics', *Sensors (Switzerland)*, vol. 20, no. 23, pp. 1–23, 2020.

[92] U. Zupančič, J. Rainbow, C. Flynn, J. Aidoo-Brown, P. Estrela, and D. Moschou, 'Strategies for Multiplexed Electrochemical Sensor Development', in *Studies in Systems, Decision and Control*, vol. 327, 2021, pp. 63–93.

[93] F. Liu, L. Ni, and J. Zhe, 'Lab-on-a-chip electrical multiplexing techniques for cellular and molecular biomarker detection', *Biomicrofluidics*, vol. 12, no. 2, 2018.

[94] Y. Han, H. Wu, F. Liu, G. Cheng, and J. Zhe, 'A multiplexed immunoaggregation biomarker assay using a two-stage micro resistive pulse sensor', *Biomicrofluidics*, vol. 10, no. 2, 2016.

[95] R. C. Castro, M. L. M. F. S. Saraiva, J. L. M. Santos, and D. S. M. Ribeiro, 'Multiplexed detection using quantum dots as photoluminescent sensing elements or optical labels', *Coord. Chem. Rev.*, vol. 448, p. 214181, 2021.

[96] M. Suzuki, H. Udaka, and T. Fukuda, 'Quantum dot-linked immunosorbent assay (QLISA) using orientation-directed antibodies', *J. Pharm. Biomed. Anal.*, vol. 143, pp. 110–115, 2017.

[97] S. Wintzheimer *et al.*, 'Supraparticles: Functionality from Uniform Structural Motifs', *ACS Nano*, vol. 12, no. 6, pp. 5093–5120, 2018.

[98] Z. Xu, L. Wang, F. Fang, Y. Fu, and Z. Yin, 'A Review on Colloidal Self-Assembly and their Applications', *Curr. Nanosci.*, vol. 12, no. 6, pp. 725–746, 2016.

[99] C. Wu, Q. Fan, and Y. Yin, 'Emulsion-confined self-assembly of colloidal nanoparticles into 3D superstructures', *Cell Reports Phys. Sci.*, vol. 3, no. 12, p. 101162, 2022.

[100] X. Zhai *et al.*, 'Inverse Pickering emulsions stabilized by carbon quantum dots: Influencing factors and their application as templates', *Chem. Eng. J.*, vol. 345, no. March, pp. 209–220, 2018.

[101] D. Liu *et al.*, 'Black Gold: Plasmonic Colloidosomes with Broadband Absorption Self-Assembled from Monodispersed Gold Nanospheres by Using a Reverse Emulsion System', *Angew. Chemie Int. Ed.*, vol. 54, no. 33, pp. 9596–9600, Aug. 2015.

[102] M. Fujii, R. Fujii, M. Takada, and H. Sugimoto, 'Silicon Quantum Dot Supraparticles for Fluorescence Bioimaging', *ACS Appl. Nano Mater.*, vol. 3, no. 6, pp. 6099–6107, 2020.

[103] J. Wang *et al.*, 'Mechanics of colloidal supraparticles under compression', *Sci. Adv.*, vol. 7, no. 42, 2021.

[104] N. Bruce, F. Farrell, and N. Laurand, 'Temperature Stability of Elastomeric Colloidal Quantum Dot Colour Converter', *2019 IEEE 2nd Br. Irish Conf. Opt. Photonics, BICOP 2019*, pp. 1–4, 2019.

[105] L. Kong, L. Zhang, Z. Meng, C. Xu, N. Lin, and X. Y. Liu, 'Ultrastable, highly luminescent quantum dot composites based on advanced surface manipulation strategy for flexible lighting-emitting', *Nanotechnology*, vol. 29, no. 31, 2018.

[106] H. Chen *et al.*, 'Flexible quantum dot light-emitting devices for targeted photomedical applications', *J. Soc. Inf. Disp.*, vol. 26, no. 5, pp. 296–303, May 2018.

[107] F. Farrell *et al.*, 'Hybrid GaN LED/Elastomer Membrane for Uniform Area Illumination', *31st Annu. Conf. IEEE Photonics Soc. IPC 2018*, pp. 18–19, 2018.

[108] K.-J. Chen *et al.*, 'The Influence of the Thermal Effect on CdSe/ZnS Quantum Dots in Light-Emitting Diodes', *J. Light. Technol.*, vol. 30, no. 14, pp. 2256–2261, Jul. 2012.

[109] M. F. Leitao *et al.*, 'Gb/s Visible Light Communications with Colloidal Quantum Dot Color Converters', *IEEE J. Sel. Top. Quantum Electron.*, vol. 23, no. 5, pp. 1–10, 2017.

[110] H. Moon, C. Lee, W. Lee, J. Kim, and H. Chae, 'Stability of Quantum Dots, Quantum Dot Films, and Quantum Dot Light-Emitting Diodes for Display Applications', *Adv. Mater.*, vol. 31, no. 34, p. 1804294, Aug. 2019.

[111] D. A. Hines, M. A. Becker, and P. V. Kamat, 'Photoinduced surface oxidation and its effect on the exciton dynamics of CdSe quantum dots', *J. Phys. Chem. C*, vol. 116, no. 24, pp. 13452–13457, 2012.

[112] J. Ko *et al.*, 'Chemically resistant and thermally stable quantum dots prepared by shell encapsulation with cross-linkable block copolymer ligands', *NPG Asia Mater.*, vol. 12, no. 1, p. 19, Dec. 2020.

[113] B. Xie, R. Hu, and X. Luo, 'Manipulating heat transport of photoluminescent composites in LEDs/LDs', *J. Appl. Phys.*, vol. 130, no. 7, p. 070906, Aug. 2021.

[114] A. P. Properties, 'Physical, Thermal, and Mechanical Properties of Polymers', in *Biosurfaces*, Hoboken, NJ, USA: John Wiley & Sons, Inc, 2015, pp. 329–344.

[115] I. Miranda *et al.*, 'Properties and applications of PDMS for biomedical engineering: A review', *J. Funct. Biomater.*, vol. 13, no. 1, 2022.

[116] S. Deguchi, J. Hotta, S. Yokoyama, and T. S. Matsui, 'Viscoelastic and optical properties of four different PDMS polymers', *J.*

Micromechanics Microengineering, vol. 25, no. 9, p. 097002, Sep. 2015.

[117] I. D. Johnston, D. K. McCluskey, C. K. L. Tan, and M. C. Tracey, 'Mechanical characterization of bulk Sylgard 184 for microfluidics and microengineering', *J. Micromechanics Microengineering*, vol. 24, no. 3, 2014.

[118] F. Schneider, T. Fellner, J. Wilde, and U. Wallrabe, 'Mechanical properties of silicones for MEMS', *J. Micromechanics Microengineering*, vol. 18, no. 6, 2008.

[119] C. Cengiz, M. Azarifar, and M. Arik, 'A Critical Review on the Junction Temperature Measurement of Light Emitting Diodes', *Micromachines*, vol. 13, no. 10, 2022.

[120] U. Ali, K. J. B. A. Karim, and N. A. Buang, 'A Review of the Properties and Applications of Poly (Methyl Methacrylate) (PMMA)', *Polym. Rev.*, vol. 55, no. 4, pp. 678–705, 2015.

[121] T.-T. Ke, Y.-L. Lo, T.-W. Sung, and C.-C. Liao, 'CdSe Quantum Dots Embedded in Matrices: Characterization and Application for Low-Pressure and Temperature Sensors', *IEEE Sens. J.*, vol. 16, no. 8, pp. 2404–2410, Apr. 2016.

[122] Y. Zhang *et al.*, 'Time-dependent photoluminescence blue shift of the quantum dots in living cells: Effect of oxidation by singlet oxygen', *J. Am. Chem. Soc.*, vol. 128, no. 41, pp. 13396–13401, 2006.

[123] X. Zhou, L. Zhai, and J. Liu, 'Epitaxial quantum dots: a semiconductor launchpad for photonic quantum technologies', *Photonics Insights*, vol. 1, no. 2, p. R07, 2022.

[124] C. Zhu *et al.*, 'Room-Temperature, Highly Pure Single-Photon Sources from All-Inorganic Lead Halide Perovskite Quantum Dots', *Nano Lett.*, vol. 22, no. 9, pp. 3751–3760, May 2022.

[125] A. Carlson, A. M. Bowen, Y. Huang, R. G. Nuzzo, and J. A. Rogers, 'Transfer printing techniques for materials assembly and micro/nanodevice fabrication', *Adv. Mater.*, vol. 24, no. 39, pp. 5284–5318, 2012.

[126] J. McPhillimy, B. Guilhabert, C. Klitis, M. D. Dawson, M. Sorel, and

M. J. Strain, ‘High accuracy transfer printing of single-mode membrane silicon photonic devices’, *Opt. Express*, vol. 26, no. 13, p. 16679, 2018.

[127] K. H. Yim, Z. Zheng, Z. Liang, R. H. Friend, W. T. S. Huck, and J. S. Kim, ‘Efficient conjugated-polymer optoelectronic devices fabricated by thin-film transfer-printing technique’, *Adv. Funct. Mater.*, vol. 18, no. 7, pp. 1012–1019, 2008.

[128] S. Scheel, ‘Single-photon sources-an introduction’, *J. Mod. Opt.*, vol. 56, no. 2–3, pp. 141–160, 2009.

[129] S. Höfling *et al.*, ‘Single photon sources for quantum information applications’, *Quantum Dots Nanostructures Synth. Charact. Model. IX*, vol. 8271, no. February 2012, p. 82710D, 2012.

[130] I. C. Robin, ‘Single-photon sources of visible light Single-photon sources of visible light’.

[131] Y. Wei *et al.*, ‘Bright and highly-polarized single-photon sources in visible based on droplet-epitaxial GaAs quantum dots in photonic crystal cavities’, *Opt. Mater. Express*, vol. 10, no. 1, p. 170, 2020.

[132] P. Lodahl, A. Ludwig, and R. J. Warburton, ‘A deterministic source of single photons’, *Physics Today*, vol. 75, no. 3. American Institute of Physics, pp. 44–50, 2022.

[133] F. Bouchard *et al.*, ‘Two-photon interference : the Hong – Ou – Mandel effect’, 2021.

[134] D. B. Higginbottom *et al.*, ‘Pure single photons from a trapped atom source’, *New J. Phys.*, vol. 18, no. 9, 2016.

[135] D. Y. Fedyanin, ‘Optoelectronics of Color Centers in Diamond and Silicon Carbide: From Single-Photon Luminescence to Electrically Controlled Spin Qubits’, *Adv. Quantum Technol.*, vol. 4, no. 10, pp. 1–19, 2021.

[136] S. Castelletto and A. Boretti, ‘Silicon carbide color centers for quantum applications’, *JPhys Photonics*, vol. 2, no. 2, 2020.

[137] P. Senellart, G. Solomon, and A. White, ‘High-performance semiconductor quantum-dot single-photon sources’, *Nat. Nanotechnol.*, vol. 12, no. 11, pp. 1026–1039, 2017.

[138] Y. Arakawa and M. J. Holmes, 'Progress in quantum-dot single photon sources for quantum information technologies: A broad spectrum overview', *Appl. Phys. Rev.*, vol. 7, no. 2, 2020.

[139] V. Chandrasekaran, M. D. Tessier, D. Dupont, P. Geiregat, Z. Hens, and E. Brainis, 'Nearly Blinking-Free, High-Purity Single-Photon Emission by Colloidal InP/ZnSe Quantum Dots', *Nano Lett.*, vol. 17, no. 10, pp. 6104–6109, 2017.

[140] X. Lin *et al.*, 'Electrically-driven single-photon sources based on colloidal quantum dots with near-optimal antibunching at room temperature', *Nat. Commun.*, vol. 8, no. 1, pp. 1–7, 2017.

[141] H. Qin, R. Meng, N. Wang, and X. Peng, 'Photoluminescence Intermittency and Photo-Bleaching of Single Colloidal Quantum Dot', *Adv. Mater.*, vol. 29, no. 14, 2017.

[142] R. H. Hadfield, 'Single-photon detectors for optical quantum information applications', *Nat. Photonics*, vol. 3, no. 12, pp. 696–705, 2009.

[143] K. Jährling, S. Wolinski, M. Ulbricht, and H. J. Schultz, 'Vergleich von Tubebaffles und Rohrschlangen in Bezug auf thermische und mechanische Energieeintragung in Rührreaktoren', *Chemie-Ingenieur-Technik*, vol. 88, no. 9, p. 1224, 2016.

[144] V. Misuk, M. Schmidt, S. Braukmann, K. Giannopoulos, D. Karl, and H. Loewe, 'Segmented Flow-Based Multistep Synthesis of Cadmium Selenide Quantum Dots with Narrow Particle Size Distribution', *Chem. Eng. Technol.*, vol. 38, no. 7, pp. 1150–1153, 2015.

[145] D. Jevtics *et al.*, 'Integration of Semiconductor Nanowire Lasers with Polymeric Waveguide Devices on a Mechanically Flexible Substrate', *Nano Lett.*, vol. 17, no. 10, pp. 5990–5994, 2017.

[146] A. W. Ziarkash, S. K. Joshi, M. Stipčević, and R. Ursin, 'Comparative study of afterpulsing behavior and models in single photon counting avalanche photo diode detectors', *Sci. Rep.*, vol. 8, no. 1, pp. 1–8, 2018.